MAGNETICALLY ACTUATED MEMS SCANNERS FOR LASER SCANNING CONFOCAL MICROSCOPY

by

Hilmi Artun Oyman

B.S., Electrical Engineering, Yıldız Technical University, 2008

M.S., Systems and Control Engineering, Boğaziçi University, 2012

Submitted to the Institute for Graduate Studies in
Science and Engineering in partial fulfillment of
the requirements for the degree of
Doctor of Philosophy

Graduate Program in Electrical and Electronics Engineering

Boğaziçi University

2019

ACKNOWLEDGEMENTS

I would like to express my sincere gratitude to my thesis advisor, Prof. Arda Deniz Yalçınkaya, for his guidance and sharing his experiences on almost everything. His motivation and his eager for accomplishment were driving forces during my study.

I'am also thankful to my thesis coadvisor, Prof. Yiğit Dağhan Gökdel, for helping me on how to develop my skills, be organized and deal with time management. His advices before the qualifier exam were precise.

I feel very lucky to work with, Prof. Onur Ferhanoğlu, from Istanbul Technical University. He was always positive and kind. His guidance in Optics part of my study was a key to my success.

I also want to thank you to my jury member, Prof. Hamdi Torun, for his constructive comments in my progress meetings. I always felt him as one of my project directors, his insights and contributions were crucial during my thesis study.

I can not forget to thank Prof. Faik Başkaya and Prof. Sema Dumanlı Oktar for accepting to be a jury member for my thesis defence.

Moreover, I want to express my appreciation to the alumni of the Beta Laboratory. I would like to thank Okan Zafer Batur for being kind all the time and ready for help, Baykal Sarıoğlu for sharing his invaluable experiences and for being supportive especially in tough times. Engin Afacan and Bedri Gürkan Sönmez for their nice conversations at lunch or during the breaks at exact 3:00 pm. Also, İskender Haydaroğlu for being a "Rippetoe style" mentor in powerlifting. I also had a chance to gain a great friend, Berk Çamlı, who is such a perfectionist and role model with his serious work ethic. The times we spend at the conferences are all memorable.

I also like to thank my friends from social science; Abdullah Sarıduman for being a tough riding partner, Öykü Tuncel and Erdem Eren for making any conversation enjoyable. Can Altay for being an easy-going, solid friend starting from at the very beginning of my MS studies. Alican Gök who is like a brother to me, I am especially thankful to him that I learnt so many things from him about any given subject.

I can not forget to thank Gökhan Gümüş for his contributions of the developed software for the image processing part of my thesis study.

I felt privileged for being coworker with Mustafa Akın İçel, who is a master of making boring things fun, and Barış Can Efe, a keen mind, a great problem solver. They were more than a working partner and their help in my studies is priceless.

Ve son olarak bu kritik süreç boyunca hep destek olan aileme sonsuz teşekkürlerimi iletiyorum.

ABSTRACT

MAGNETICALLY ACTUATED MEMS SCANNERS FOR LASER SCANNING CONFOCAL MICROSCOPY

Magnetically actutated micro-scanners are fabricated via three-dimensional (3D) printing and laser machining technologies to use in a laser scanning confocal microscopy application. First, a 3D printed polymer based scanning mirror with magnetic actuation is designed to meet a confocal microscopy application providing 100 μm $\times$ 100 μm field of view and less than 3-μm lateral resolution. Stress distribution along the circular-profiled flexure is compared with a rectangular counterpart in finite-element environment. The resonance frequencies of the device were analytically modeled. Finally, imaging experiments were conducted on a resolution target, showcasing the desired scan area and resolution. In the second part of thesis, laser machining technology is used to produce stainless steel the micro-scanners. First device is developed for a 2D confocal imaging application. This device tested with the United States Air Force target accomplishing a 200 μm $\times$ 200 μm field of view and sub 10 μm resolution. In the following study, a micro-scanner with multi-gimbaled structure is designed and produced for 3D Lissajous confocal imaging application. This device can work in three different out-of-plane modes in order to control the focus of the confocal system. Final study contains a micro-scanner for 3D beam steering with better performance specifications, such as higher TOSA for less current consumption, increased resonance frequencies and smaller total size of the device as opposed to the previously designed micro-scanners. Also, fabricated micro-scanner is integrated in a confocal system and 2D image of a biological sample; convallaria rhizome, is obtained. Furthermore, a novel 3D confocal microscopy configuration is proposed and it's validty is tested for 3D beam steering on a custom confocal setup.

ÖZET

LAZER TARAYICILI KONFOKAL MİKROSKOPLAR İÇİN MANYETİK OLARAK HAREKETLENDİRİLMİŞ TARAYICILAR

Üç boyutlu baskılama ve lazer işleme teknolojileri ile üretilip manyetik olarak hareketlendirilen mikro tarayıcılar, eşodaklı mikroskop uygulamasında kullanıldılar. Öncelikle, üç boyutlu yazıcıyla polimer malzemeden üretilen tarayıcı, manyetik olarak harekete geçecek, eşodaklı bir mikroskop sistemi içerisinde 100 μm $\times$ 100 μm görüş alanı ve 3-μm'den düşük bir yanal çözünürlük sağlayacak şekilde tasarlandı. Dairesel ve dikdörtgen kesitli dirseklerin uzunlukları boyunca stres dağılımı sonlu eleman yöntemi yazılımı içerisinde karşılaştırıldı. Dizayn edilen cihazın rezonans frekansları analitik olarak modellendi. Son olarak, hedeflenen görüş alanını ve çözünürlüğü ortaya çıkartacak bir hedef üzerinde görüntüleme deneyleri yapıldı. Tezin ikinci kısmında, lazerle işleme yöntemi kullanılarak paslanmaz çelikten mikro tarayıcılar üretildi. İlk tarayıcı iki boyutlu eşodaklı mikroskop uygulaması için geliştirildi. Bu cihaz Birleşmiş Devletler Hava Kuvveti isimli hedef üzerinde test edilerek 200 μm $\times$ 200 μm görüş alanı ve 10 μm'nin altında çözünürlük sağladığı gözlemlendi. Takip eden çalışmada, çoklu çerçeve geometrisine sahip bir mikro tarayıcı üç boyutlu Lissajous eşodaklı görüntüleme uygulaması için tasarlanıp üretildi. Bu cihaz, üç farklı düzlem dışı modda çalışarak eşodaklı mikroskop sisteminin odağını değiştirebiliyor. Son çalışmada üretilen mikro tarayıcı, daha önce üretilen diğer cihazlara kıyasla, daha düşük akımla daha yüksek toplam optik tarama açısına, daha yüksek rezonans frekanslarına ve daha küçük toplam boyuta sahip olacak şekilde üç boyutlu ışın idaresi için üretildi. Üretilen mikro tarayıcı eşodaklı mikroskop sistemi içerisine entegre edilip müge köksapının görüntüleri elde edildi. Ayrıca, özgün bir üç boyutlu eşodaklı mikroskop sistemi ileri sürülerek üç boyutlu ışın idaresi için özel bir eşodaklı düzenek üzerinde geçerliliği test edildi.

TABLE OF CONTENTS

LIST OF FIGURES

LIST OF TABLES

LIST OF SYMBOLS

D	Diameter of the flexure
E	Young's Modulus of the material
E_n	Young's Modulus of Neodmium
E_v	Young's Modulus of Veroclear
f_{o}	Resonance frequency of out-of-plane mode
f_{t}	Torsional resonance frequency
J_{eff}	Effective moment of inertia
G	Shear modulus of the material
I_{xx}	Polar moment of inertia around x axis
k_c	Torsional spring constant for circular profile
k_{o}	Spring constant for out-of-plane movement
k_r	Torsional spring constant for rectangular profile
k_{t}	Torsional spring constant
L	Length of the flexure
M	Magnification constant of the relay lens pair
M_m	Mass of the mirror
M_f	Mass of the flexure
t	Thickness of the flexure
W	Diameter of the flexure
λ	Input laser wavelength
ν_n	Poisson's ratio of Neodmium
ν_v	Poisson's ratio of Veroclear
ρ	Density of the material
θ_o	Zero-to-peak optical scan angle

LIST OF ACRONYMS/ABBREVIATIONS

1D	One-Dimensional
2D	Two-Dimensional
2P	Two-Photon Microscopy
3D	Three-Dimensional
CAD	Computer Aided Drawing
CM	Confocal Microscopy
FEM	Finite Element Method
FOV	Field-of-View
FPS	Frame per Second
FR4	Fire Retardant 4
FWHM	Full-Width Half-Maximum
LDV	Laser Doppler Vibrometer
LSCM	Laser Scaning Confocal Microscopy
MEMS	Micro Electro Mechanical Systems
MOI	Moment of Inertia
OCT	Optical Coherence Tomography
NA	Numerical Aperture
PDMS	Polydimethylsiloxane
TOSA	Total Optical Scan Angle
USAF	United States Air Force

1. INTRODUCTION

Advances in optical fiber, Micro Electro Mechanical Systems (MEMS) and computing technologies have paved the way for minimally invasive, low cost optical imaging approaches. Some of the currently available imaging techniques are, optical coherence tomography (OCT) [24–26], two photon microscopy (2P) [27–29] and confocal microscopy (CM) [30–32].

1.1. Historical Background of Confocal Microscope

The word microscope comes from ancient greek which consists of two words; μικρός (mikrós) meaning "small" and σκοπεῖν (skopeîn) meaning "to look" or "see". Giovanni Faber, fellow of the Accademia dei Lincei, was the one who coined the word "microscope" (microscopio) to Galileo's "small eyeglass" (occhialino) in 1625 [1].

Figure 1.1. Designed by Galileo Galilei in the second half 17th century [1]

One of the earliest examples of a compund microscope which includes concave and convex lenses is shown in Figure 1.1 and it is said to have been construted by Galileo;

however, is now more plausibly attributed to Giuseppe Campani. This microscope is an exhibit at Museo Galileo in Florance.

A microscope is basically helps us to see or examine very small things with naked eye. Some famous examples of these "small things" are living tissue, surface of a material, cell of a plant etc.

In 1954, Marvin Minsky, an expert in artificial intelligence, is considered as the founder of this huge branch. He was trying to map a neuron and the available system in those years was not good enough to see a proper image [33]. In order to solve that problem, he invented the confocal microscope.

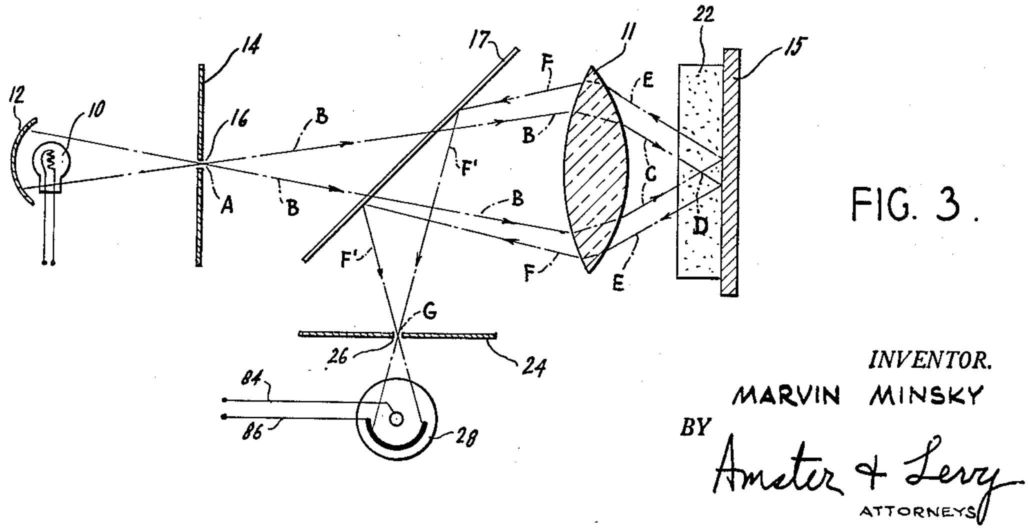

Figure 1.2. Microscopy apparatus US3013467A [2].

Minsky's idea was point by point scanning a laser source over the sample to be imaged and collecting the reflected light through eliminating out-of-focus light using a pinhole (Figure 1.2). In his setup, the rays emitted from a bulb (10) travels through a pinole aperture (16) to provide a point light source. The divergent beam passes through a beam splitter (17), is focused via an objective lens (11) upon a target (22) to expose a very small field included in the specimen. The illuminated point reflects back from the surface of a mirror (15) is directed by the beam splitter onto another pinhole aperture (26). A photoelectric cell (28) is located behind the pinhole to collect the intensity data of the light.

The cost of a single point illumination was being able to measure only one point at a time and the whole process of imaging can take a long time because it is the summation of time intervals it takes to collect sufficient light to measure each image point. That amount of time could be decreased by using a brighter light and he used a carbon arc which was the available brightest source in those years.

The most critical design problem was choosing between moving the specimen or moving the beam. At first he thought it would look more elegant to deflect a weightless beam of light than to move a huge specimen. However, the three-dimensional alignment of two tiny moving apertures forces Minsky to keep the optics fixed and move the stage. The intensity values were measured with a low noise photomultiplier. At the end of the day, the image was reconstructed on the screen of a military surplus long persistence radar scope.

In 1960s, Mojmír Petráň developed the first commercialized confocal microscope which is called tandem scanning microscope (Figure 1.3). In this microscope setup, the rays radiated from a planar light source (7) (i.e. tungsten ribbon lamp, a zirconium oxide arc lamp, etc.) are focused by a photographic type objective lens (8) by way of a reflecting mirror (9) into the plane of the Nipkow disc (1). An inverting system (2), includes an odd number of reflections, inverts the rays to the mirror (10). The beams of rays hits a beam splitter (3), where a part of the light is reflected to the objective lens (4); whereas, the another part of the light passes the beam splitter and is absorbed on the walls of the microscope system. In the end, the images of the holes in the Nipkow disc are focused by the microscope objective (4) into the object plane (6). The light reflected from the illuminated part of the observed object enters again the objective lens of the microscope (4), passes partly through the light splitter (3), is reflected by the mirror or prism (11) perpendicularly to the axis of the microscope objective (4), is again reflected by the mirror (12) into a direction parallel with same axis reaches an inverting system (5) similar to the system (2) in the illuminating part. After the inverting system, the image of the sample is ready to be viewed by the eye piece (13).

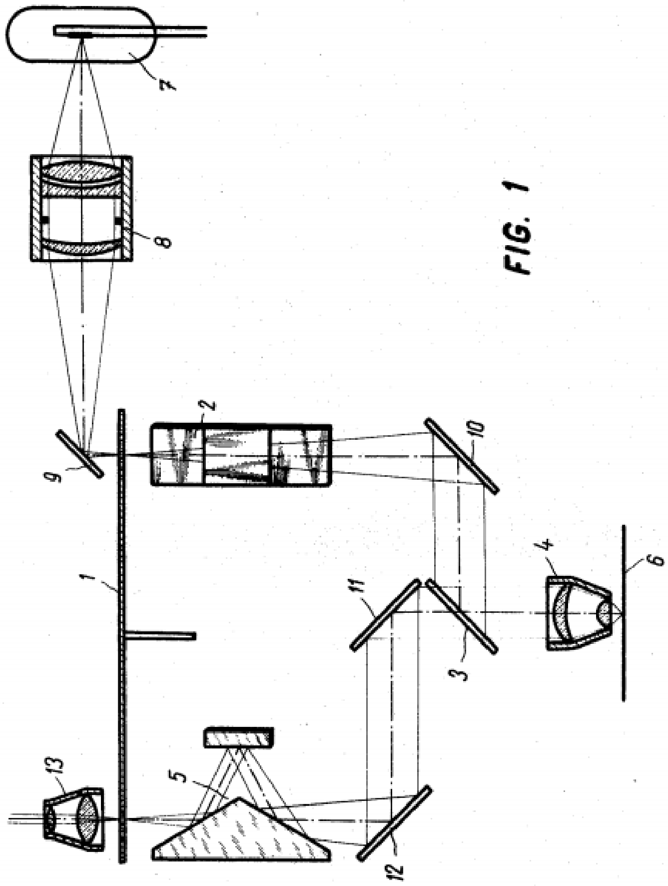

Figure 1.3. Method and arrangement for improving the resolving power and contrast US3517980 [3].

The Nipkow disc is rotated with the help of a small electric motor at a speed about 100 revolutions per minute and its holes are simultaneously scanning both the object and the image field of view. Moreover, the scanning frequency of the disc must be high enough to provide a stable picture.

The first journal was published in 1967 where M. David Egger and Mojmír Petráň examined unstained cells and cell processes in brains of living salamanders and in excised dorsal root ganglia of frogs which are challenging samples to be seen [34]. One year later, another journal was published explaining the theory and technical details of this imaging device. The working principle of tandem scanning microscope is similar to the confocal microscope where the tandem scanning system improves the contrast of semitransparent material by eliminating the light coming above and below the object plane of interest. A special rotating disc which has holes on its both sides, called Nipkow wheel, one side of which is used to provide light to the object and the other side of this mechanism is used for the reflected light.

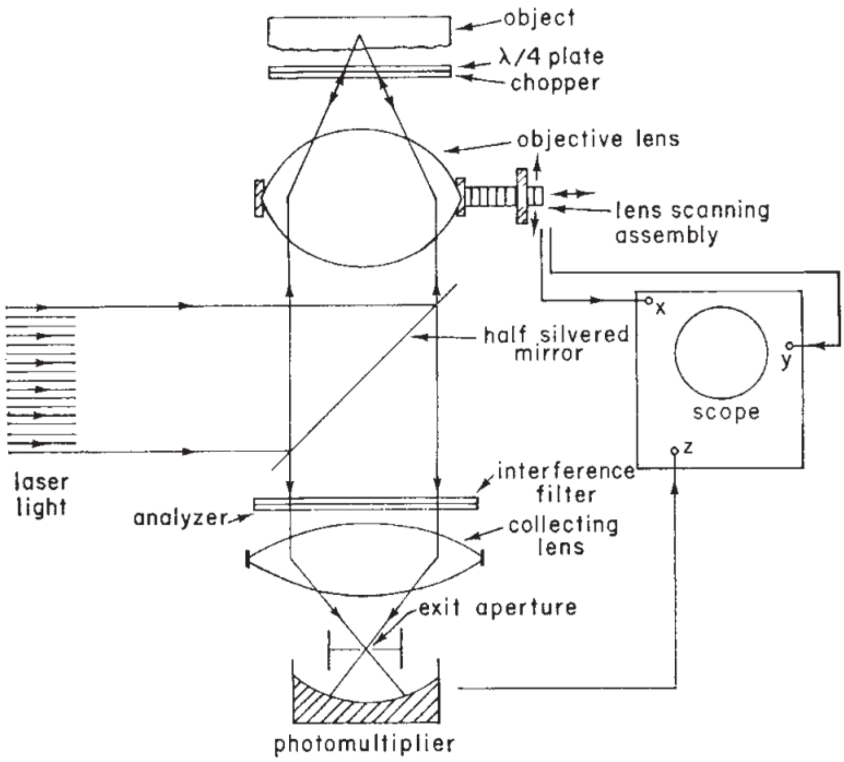

Figure 1.4. Schematic of laser scanning microscope [4].

In 1969, M. David Egger and Paul Davidovits published a paper briefly explains the working principle of the first prototype of a laser scanning confocal microscope [4]. In this setup, a 5 mW He-Ne continous wave laser used as a light source. Also scanning pattern is generated by the motion of the objective lens which was a novel idea for the movement of the focal point (Figure 1.4). After the collection of the reflected light via a photomultiplier, an image is built up on an oscilloscope screen. Two years later, a second paper was published which explains the theory and design of the laser scanning microscope in detail. A ruled glass surface is used for the characterization of the microscopy system. Moreoever, the images of a fresh smear of unfixed, unstained blood of a frog and nerve fibers in a spinal rootlet from a cat are demonstrated.

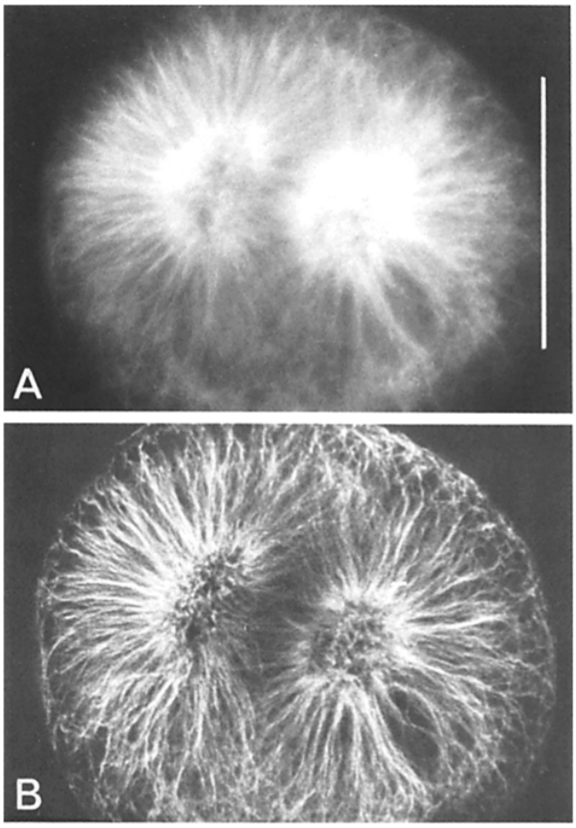

Figure 1.5. Fertilized egg of sea urchin stained with antitubulin. (A) Conventional image for comparison with (B) confocal. Bar, 50 μm [5].

The benchmarking of confocal microscope is published in a work by Fred Brakenhoff and coworkers in 1987 [5]. This was the first paper which has satisfactory images taken on a confocal microscope that were able to answer biological questions (Figure 1.5). For further information about how the confocal microscopy becomes a need for every biological labrotary, the reader may consult the paper published by W. B. Amos and J.G. White [35].

Today, confocal microscopy is a well-established laser-scanning based optical imaging technique, which provides increased contrast and high optical resolution [2]. Images of human and mouse skin [36], colon tissue [37], oral mucosa [38], GI-tract [39] and colon tissue of a rat [40] have already been acquired with CM, for tissue assessment.

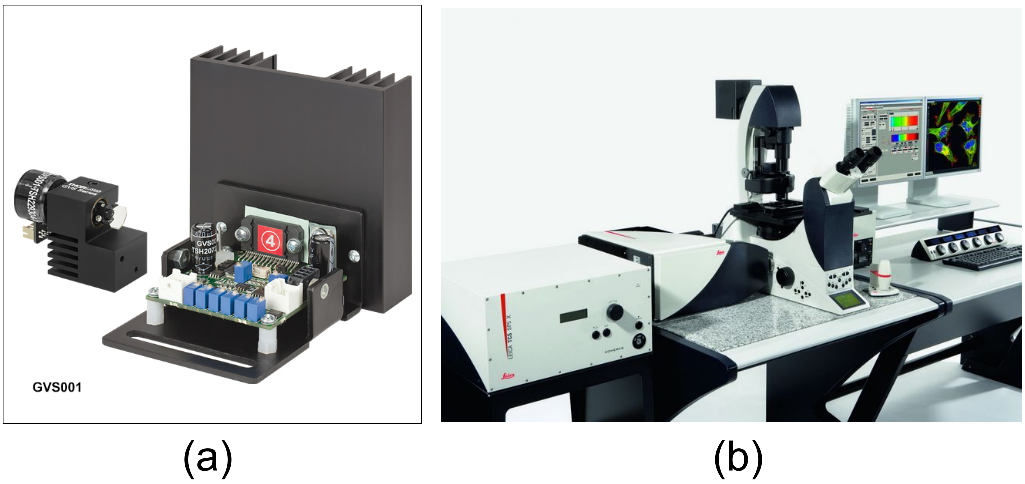

Figure 1.6. (a) Small beam diameter scanning galvo mirror system (Thorlabs GVS001) [6]. (b) Commercial confocal microscope (Leica TCS SP5 X) [7].

Although, galvanometers (Figure 1.6a) are favored as the scanning units in traditional laser scanning confocal microscopes [41] (Figure 1.6b), nowadays, the scanning units are getting replaced by micro-scanners in order to make the LSCM more compact and portable [42–44].

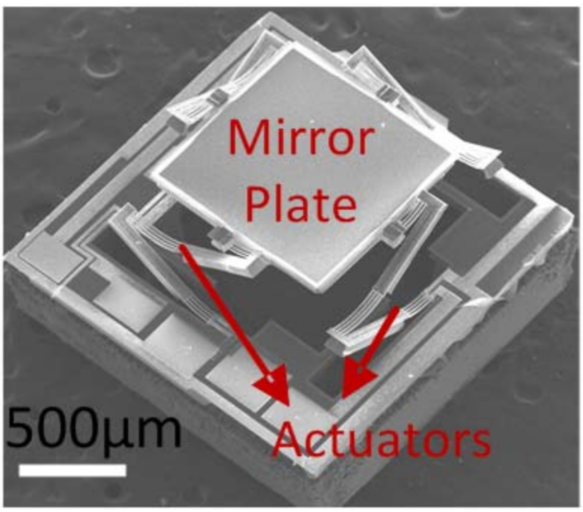

Figure 1.7. Scanning electron microscope image of a MEMS mirror used in a confocal microscope [8].

One example of such a micro-scanner is shown in Figure 1.7 which is used to get two dimensional (2D) and three-dimensional (3D) confocal reflectance images of microparticles embedded in Polydimethylsiloxane (PDMS) and acute rat brain tissue [8]. The micro-scanner in a LCSM system has a critical role in defining the field-of-view (FOV), the full-width half-maximum (FWHM) resolution and the frame rate. The topology, the structural material, together with the actuation technique determines the overall performance of the micro-scanner. These MEMS devices can be actuated using various techniques such as electrothermal [45], electrostatic [46], piezoelectric [47], and magnetic [48] ones.

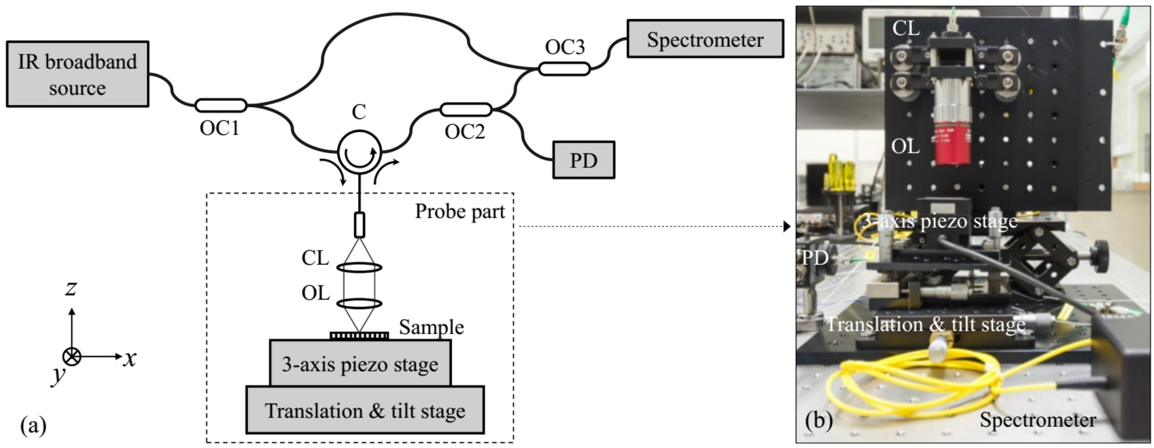

Figure 1.8. (a) Optical layout of fiber-based confocal and interferometric system for measuring the depth and diameter of through silicon vias. (OC1, OC2, OC3: optical coupler; C: circulator; CL: collimation lens; OL: objective lens; PD: photo-detector.) [9].

3D imaging of biological samples is of utmost importance in medicine and biology. Though typically piezoelectric stages (Figure 1.8) are placed under the samples for axial displacement [9], a low-cost and potentially hand-held system would benefit from having an internal 3D laser scanning capability.

Another study have focused on using separate MEMS scanners for lateral and axial scans [10]. These MEMS devices are also integrated in an endoscopic probe (Figure 1.9). The confocal reflectance 2D and 3D images of micro-patterns, microparticles, onion skins and acute rat brain tissue are obtained with the fabricated microendoscope.

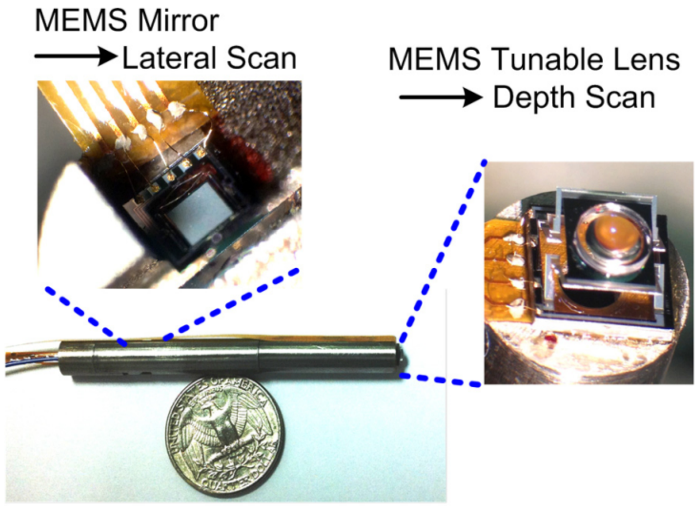

Figure 1.9. Photograph of an assembled the endoscopic probe [10].

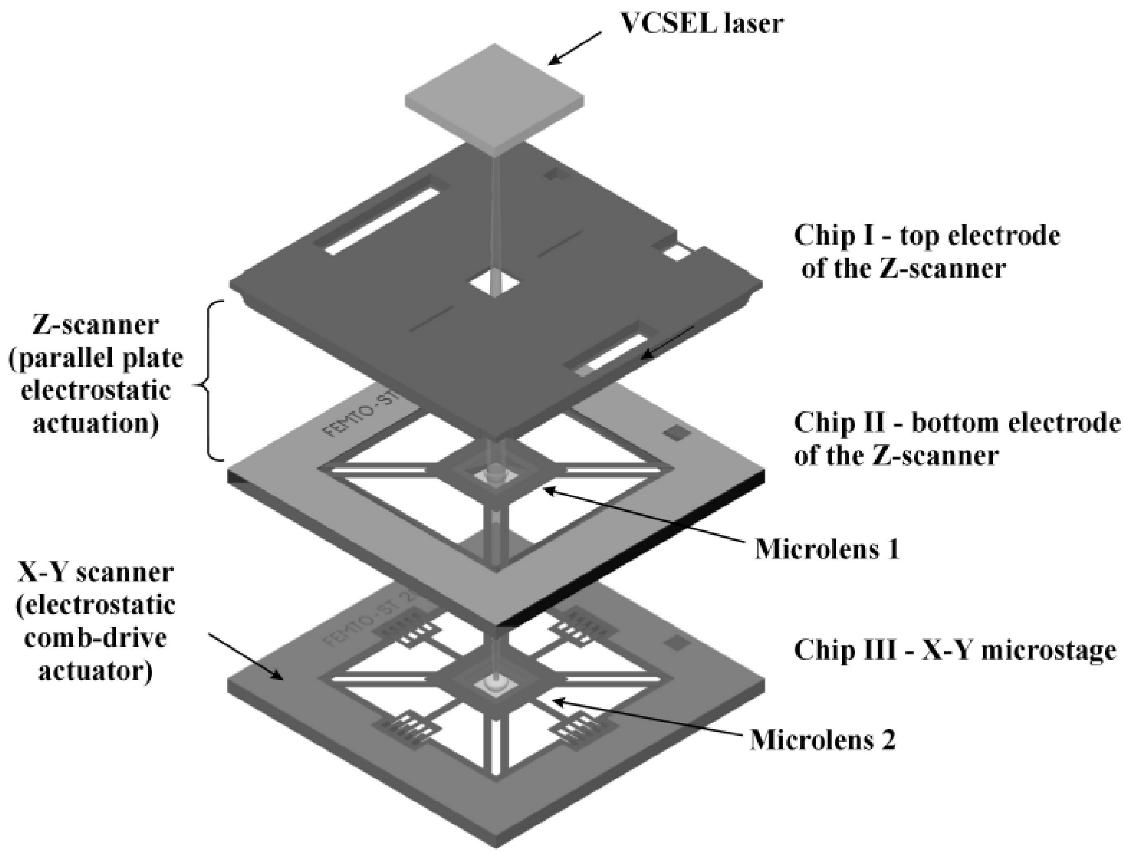

Figure 1.10. Schematic of the miniaturized scanning optical confocal microscope on-chip [11].

Multiple MEMS chips have also been integrated with a vertical-cavity surface-emitting laser (Figure 1.10), which enables transmissive scanning of the light beam, where one MEMS chip performs lateral scanning of a microlens, while the other axially scans another microlens, which leads to 3D scanning [11].

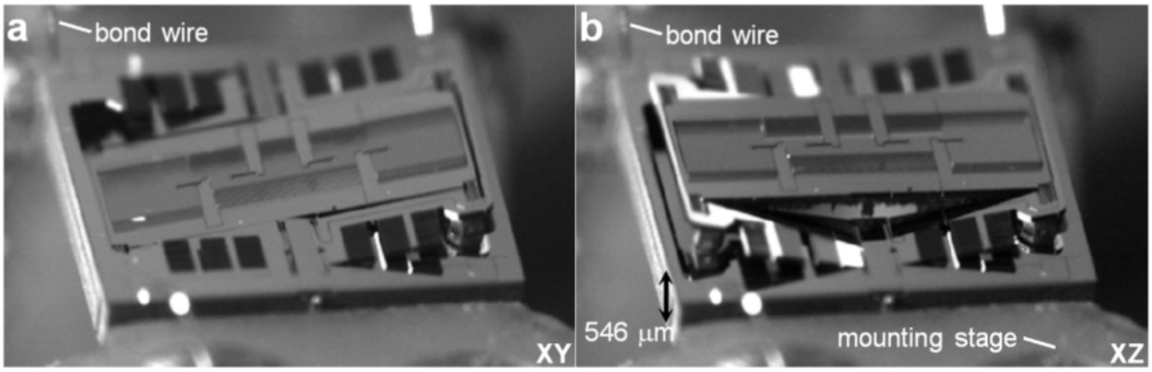

Figure 1.11. 3D scanner motion. (a) angular tilting of the mirror to produce images in the XY-plane and (b) large out-of-plane motion of the gimbal frame supporting the mirror in the XZ direction [12].

MEMS scanners (Figure 1.11) were manufactured for 3D scanning with a single device, for dual axes confocal imaging [12].

In all of the summarized literary studies, either multiple scanning devices are used, or complicated MEMS systems have been designed, necessitating more than 5 lithography steps. Many studies in literature have used surface curvature control to change focus while they were working with collimated incident beam, surface aberration and high voltage requirements during actuation can be problematic [49, 50].

1.2. Contributions of the Thesis

In this work, 3D printing technology is used to fabricate a polymer micro-scanner and stainless-steel based micro-scanners are built with laser-machine technology. These devices are easy to manufacture with low cost (as opposed to Silicon micro-scanners) and they are designed with particular topologies (depending on their applications) such that their sizes, resonant frequencies and total optical scan angles (TOSA) are taken into consideration. Following the fabrication and characterization steps, these scanners are integrated in different custom confocal microscopy setups for 2D and 3D imaging.

The ratio of the orthogonal torsional resonance frequencies of all the proposed micro-scanners are less than three and their deflections severely reduces if they are not actuated at their resonance frequencies. Therefore, they are not applicable for the traditional raster scanning method. However, they are specifically designed with mutually prime resonance frequencies which makes them suitable for generating Lissajous trajectories.

Notable contributions of the thesis work are summarized below:

- *A polymer based micro-scanner is fabricated via 3D printing technology:* 3D printing technology is gaining more and more popularity in diverse research areas ranging from robotics to biomedical engineering and for the first time this methodology is utilized for the realization of a low cost micro-scanner. The technology has a pretty simple fabrication process as compared to the lithography steps used in silicon devices. Moreover, the method also offers additional flexibility in controlling the cross-sectional profile as well as the stress distribution along the flexures of the micro-scanner compared to the traditional planar process technologies. A proceeding and an article were published in *IOP, Journal of Physics: Conference Series* [17] and *SPIE, Optical Engineering* [18], respectively.

- *Stainless-steel micro-scanners are manufactured using laser-machining technology.* Polymer based micro-scanners were having rather slow resonant frequencies and that issue motivated us to built new devices out of stainless steel by using a novel technique; laser-machining technology. This method allows us to create fine shapes on a given substrate easily with high accuracy within a small amount of time. The whole process routine of this technique is quite easy as in the previous study. Moreover, a special type of stainless steel, namely, grade:430, is used as base material due to its high relative magnetic permeability which provides more displacement as opposed to other kind of stainless steels. First micro-scanner is designed for 2D confocal imaging and this study is published as a proceedings in *MDPI, Proceedings of Eurosensors 2017.* Second micro-scanner with its multi gimbaled topology, is suitable for controling the focus of a 3D confocal system and this study is published in *MDPI, Proceedings of Eurosensors 2018.* Last micro-scanner is designed with better performance specifications such as TOSA, power consumption and total size as opposed to the previously designed scanning devices. Also a novel 3D imaging confocal configuration is proposed and the validty of the 3D beam steering of this system is tested on a custom benchtop confocal setup. This work is published as an article in *IOP, Journal of Physics D: Applied Physics.*

1.3. Organization of the Thesis

This work is organized as follows. Theoretical background of optical designs and resonance frequency calculations of the micro-scanners are explained in the following chapter. Chapter 3 reports the design, fabrication and implementation of a 3D-printed micro-scanner. In chapter 4, implementation of laser-machined stainless-steel micro-scanners for different confocal applications are explained. Conclusion and discussions are supplied in the final chapter.

2. THEORETICAL BACKGROUND

Theoretical background of the optical design preferences, resonance frequency calculations, scanning methods and Gaussian optics are provided in this chapter of the thesis. Two of the important optical system design criteria, namely, full-width half-maximum and field-of-view are defined and their relation with each other and other crucial system parameters such as magnification constant of the relay lens pair, wavelength of light, numerical aperture (NA) of the objective lens and zero-to-peak optical scan angle are explained. Also, the question of how to build an infinity-corrected optical system, which is a critical building block of a confocal microscope, is addressed. The resonance frequency calculations of micro-mirror devices are derived. Moment of inertia (MOI) computations of highly symmetrical composite structures are illustrated with a simple example. Furthermore, two of the basic scanning methods, namely, raster and Lissajous scan are explained and compared with each other. Two of the important 3D confocal imaging design criteria are the depth-of-focus and depth-of-field and for that reason some Gaussian beam optics formulas are provided.

2.1. Optical Design for 2D Imaging

Imagine that you are going to buy a new microscope to your laboratory, two questions come to your mind about the technical properties of this imaging tool without much thinking: How small things can I observe with this machine and how much area can I see when I look at the eyepiece of the microscope. These questions are addressed by looking at the numerical values of FWHM spot diameter (w) and FOV, respectively. For a typical 2D confocal microscope, these two parameters can be determined as optical design constraints. In order to choose the suitable objective lens, magnification constant of the relay lens pair (M) and finally, zero-to-peak optical scan angle (θ_o) of the scanner to be integrated for the confocal system, the above mentioned constraints are plugged into the following equations [51, 52].

$$\mathrm{w} = \frac{2\sqrt{\ln 2}\; 0.32\ \lambda}{NA} \tag{2.1}$$

$$\mathrm{FOV} = \frac{2\ \theta_o\ F}{M} \tag{2.2}$$

where, λ is the input laser wavelength, NA is the numerical aperture and F is the focal length of the objective lens. From these two equations, one can deduce that there is a trade-off between spot size and FOV. The reason behind this is that if you choose an high NA objective lens, the focal length of the objective lens will be small and it will reduce the FOV or vice versa (assuming that all the other parameters are constant).

Table 2.1. FWHM and FOV values for various thorlabs reflective objective lenses [21].

NA	**F (mm)**	**λ (nm)**	**θ_0 (degrees)**	**M**	**w (μm)**	**FOV (μm)**
0.3	13.3	650	5	1	1.15	1160
0.4	8	650	5	1	0.86	698
0.5	5	650	5	1	0.69	436

In Table 2.1, FWHM and FOV values for various thorlabs objective lenses with different numerical apertures are calculated using Equations 2.1 and 2.2. As you can see, while the NA of an objective increases, its focal length reduces which, in turn, causes the trade-off between FWHM and FOV (assuming that all the other parameters are constant).

Let us consider one of the building blocks of confocal microscope system which provides an infinity-corrected optical system as shown in Figure 2.1. The crucial advantages of using such a system are all the rays reaching the objective lens are collimated beams and even the micro scanner moves, as it is pointed out in the Figure 2.1, the rays fills the back aperture of the objective lens.

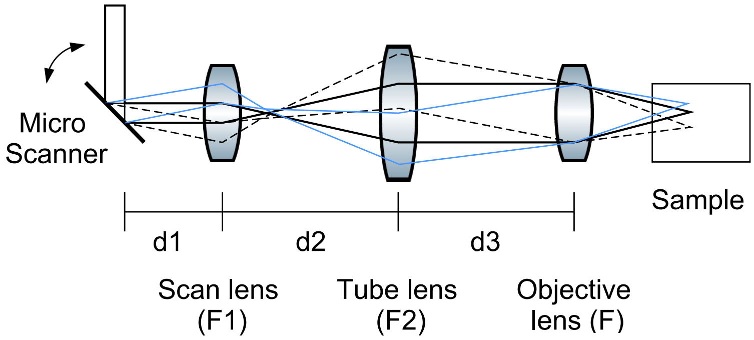

Figure 2.1. Schematic of infinity-corrected configuration for lateral scan.

The first lens, which is called scan lens, has effective focal length (F_1) and the second relay lens, namely tube lens, has effective focal length (F_2). Using the focal lengths of the relay lens pair and the distance between the center of the micro-scanner to the center of the scan lens, represented by d1 in Figure 2.1, the distance from tube lens to the objective (d_3) is found by using the following formula [53] which ensures an infinity-corrected configuration.

$$d_3 = \frac{\frac{F_1^2}{F_2} + F_1 - d_1}{\left(\frac{F_1}{F_2}\right)^2} \tag{2.3}$$

2.2. Resonance Frequency Calculations of Micro-Scanners

Resonance frequency is one of the most important properties of a micro-scanner. It has a huge impact on the frame rate when it is used as a light manipulator in an imaging system. Also, together with the total-optical-scan-angle, resonance frequency determines which scanning method is going to be used in a confocal microscopy. In general, the natural freuquency of a micro-scanner is desired to be as high as possible and before the fabrication and finite-element-mode simulations, estimating the resonance frequency by analytical calculations saves us time and money.

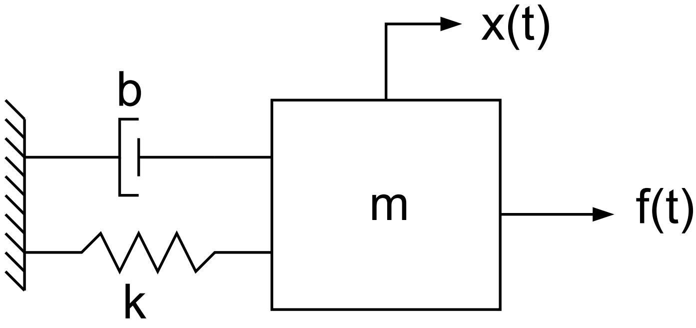

Figure 2.2. Spring-mass-damper system.

The micro-scanner can be modeled as a spring-mass-damper system (Figure 2.2. Since it has a negligible effect on the natural frequency for underdamped systems, damping factor can be ignored ($Q \geq 10$). Resonant frequency of the structure for the torsion mode can be approximated as a simple harmonic oscillator [54].

$$f_{\mathrm{t}} = \frac{1}{2\pi}\sqrt{\frac{k_{\mathrm{t}}}{J_{\mathrm{eff}}}} \tag{2.4}$$

where k_{t} is the torsional spring constant and J_{eff} is the effective moment of inertia of the proposed device.

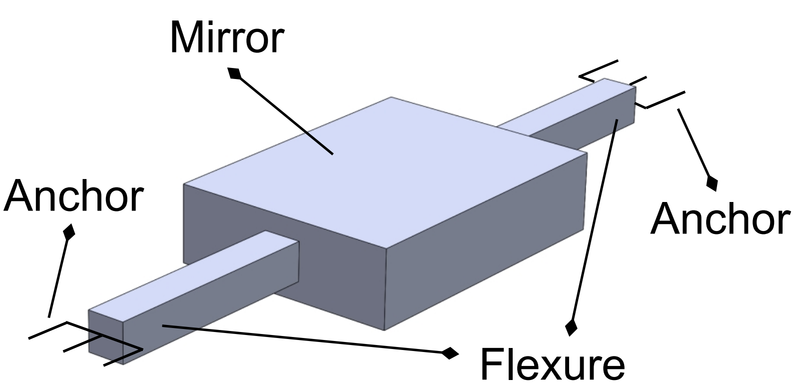

Figure 2.3. One-dimensional (1D) scanning micro-scanner with simple geometry.

As seen in Figure 2.3, a 1D micro-scanner with highly symmetrical structure consists of a mirror part and two flexures. The MOI of these sections can be calculated one by one and the effective MOI for a micro-scanner can be derived approximately in terms of the geometric parameters of the structure and given densities of the materials.

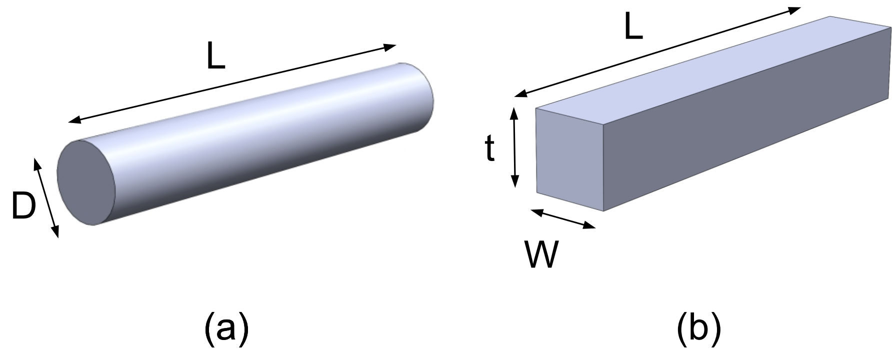

Figure 2.4. Flexure beam with circular (a) and rectangular (b) cross-section.

Depending on the profile shape of the flexure, which can be circular (Figure 2.4a) or rectangular (Figure 2.4b), k_t is denoted by either k_c or k_r, respectively. For instance, torsional spring constant of a beam with circular cross-section is given as follows [55]:

$$k_{\mathrm{c}} = \frac{G\pi r^4}{2L} \tag{2.5}$$

where G is shear modulus of the material, r and L are the radius and the length of the flexure, respectively (Figure 2.4a). Similarly, torsional spring constant of a rectangular cross-sectional beam, based on isotropic material, for the structures when $t \geq W$ and $W \geq t$, are given in order as follows [54]:

$$k_{\mathrm{r}} = \frac{W^3\, t}{8L}\, G \left[5.33 - 3.36\left(\frac{W}{t}\right)\left(1 - \frac{1}{12}\left(\frac{W}{t}\right)^4\right)\right] \tag{2.6}$$

$$k_{\mathrm{r}} = \frac{t^3\, W}{8L}\, G \left[5.33 - 3.36\left(\frac{t}{W}\right)\left(1 - \frac{1}{12}\left(\frac{t}{W}\right)^4\right)\right] \tag{2.7}$$

where W, L and t are the width, length and thickness of the beam (Figure 2.4b). Whereas, resonance frequency of out-of-plane mode of a micro-scanner can be calculated using the following equation [54]:

$$f_{\mathrm{o}} = \frac{1}{2\pi}\sqrt{\frac{k_{\mathrm{o}}}{M_{\mathrm{eff}}}} \tag{2.8}$$

where k_{o} is the spring constant for out-of-plane movement and M_{eff} is the effective mass of the device. Mass of the mirror and flexure part of a micro-scanner device can be carried out individually in terms of the corresponding dimensions and material density of the structure. Spring constant of out-of-plane mode can be found using following equation [56]:

$$k_{\mathrm{o}} = \frac{24EI_{xx}}{L^3} \tag{2.9}$$

where E is the Young's Modulus of the material, I_{xx} is the polar moment of inertia around x axis and L is the length of the flexure.

2.3. Moment of Inertia of Composite Structures

The torsional and out-of-plane resonance frequencies of the micro-scanners can be found by using the necessary equations explained in the previous section. However, in those expressions, MOI of a designed micro-scanner has to be calculated.

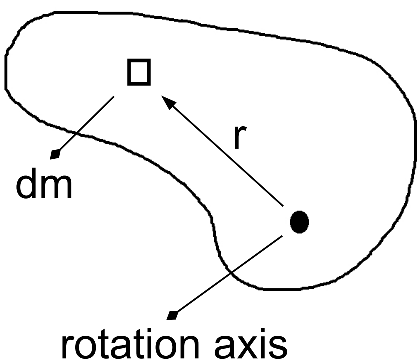

Figure 2.5. MOI integral demonstration for an arbitrary shaped object.

Since the scanner devices have complex geometry, MOI computations should be explained in detail. The moment of inertia of an arbitrary shaped rigid body (Figure 2.5) can be calculated as follows: [57]:

$$I = \int_0^M r^2\, dm \tag{2.10}$$

where r is the distance from the rotation axis, dm is an infinitesimal and M is the total mass of the object. Instead of using their mass, volume of the elements is used to calculate the moment of inertia easily. This change can be made by $\rho = \frac{m}{V}$ where, ρ is the density and V is the volume of the object. Therefore, the mass for very small elements becomes $dm = \rho\, dV$. Plugging this result in Equation 2.10 provides

$$I = \int_0^V \rho r^2\, dv \tag{2.11}$$

If the structure is homogeneous, ρ is constant and for a given geometry, the integral can be evaluated easily. If the structure is inhomogeneous, then the dependence of density to the position must be known to solve the integration.

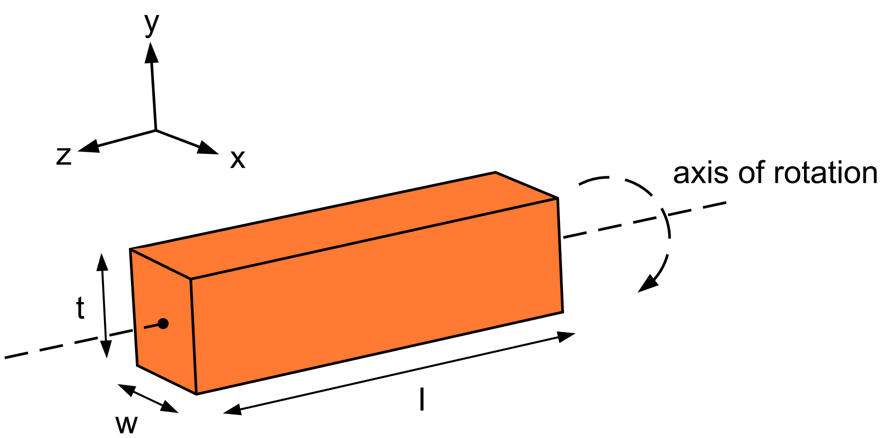

Figure 2.6. Rectangular prism with its parametric dimensions.

Let us use the Equation 2.11 to derive the MOI of a rectangular solid (Figure 2.6) about its axis of rotation (z axis). Assuming that the whole structure is homogeneous, the rectangular prism can be divided into beams having a width, length and thickness of dx, l and dy, respectively. Hence, the infinitesimal volume in Equation 2.11 becomes $dv = l\,dx\,dy$. The distance of each beam to the rotation axis in x-y plane can be described as $r = x^2 + y^2$. The total volume of the prism can be expressed as sum of the volumes of all slender beams; therefore, the distance of each beam to the rotation axis changes between $\frac{-w}{2}$ to $\frac{w}{2}$ and $\frac{-t}{2}$ to $\frac{t}{2}$ for the x and y axis, respectively.

$$I = \int_{\frac{-t}{2}}^{\frac{t}{2}} \int_{\frac{-w}{2}}^{\frac{w}{2}} \rho l(x^2 + y^2)\,dx\,dy \tag{2.12}$$

Since ρ and l are constant, they can be taken outside the integral and the first integral is evaluated as follows:

$$I = \rho l \int_{\frac{-t}{2}}^{\frac{t}{2}} \left[\frac{x^3}{3} + xy^2\right]_{\frac{-w}{2}}^{\frac{w}{2}} dy \tag{2.13}$$

After using the limits of the first integral, the expression becomes

$$I = \rho l \int_{\frac{-t}{2}}^{\frac{t}{2}} \left(\frac{w^3}{12} + wy^2\right) dy \tag{2.14}$$

If we take the second integral the equation will be as follows:

$$I = \rho l \left(\frac{w^3 y}{12} + \frac{wy^3}{3}\right)_{\frac{-t}{2}}^{\frac{t}{2}} dy \tag{2.15}$$

Using the limits in this last function, the simplified following equation is obtained.

$$I = \frac{1}{12} m(w^2 + t^2) \tag{2.16}$$

where m is the mass of the rectangular block and $m = \rho lwt$ is used in the last equation.

As mentioned before, a simple 1D micro-scanner consists of mirror part and flexure beams (Figure 2.7). The moment of inertia of the device about x axis can be

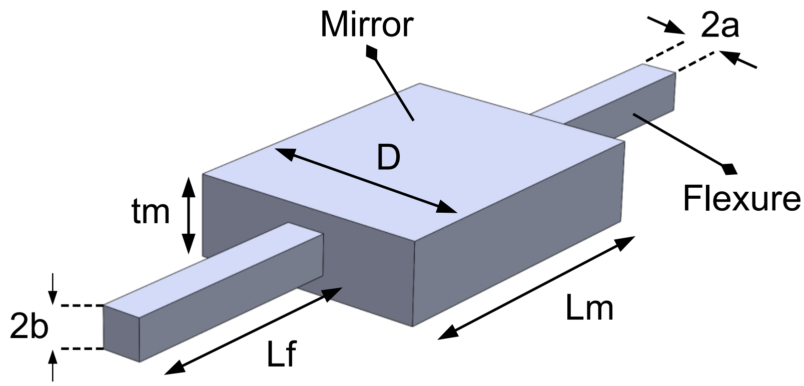

Figure 2.7. A torsional resonant scan mirror with simple geometry.

evaluated by dividing the whole structure into small elements. Here in this particular example, MOI of mirror and flexure part can be found individually. These building blocks are rectangular solids as previously demonstrated in Figure 2.6 and it's MOI is derived with Equations 2.11-2.16. Hence, the total MOI is equal to sum of the MOI of the mirror and two flexures in terms of parametric distances shown in Figure 2.7 as follows:

$$I = \frac{1}{12}M_m(D^2 + t_m^2) + \frac{2}{3}M_f(a^2 + b^2) \tag{2.17}$$

where M_m and M_f are the mass of the mirror and flexure, respectively.

2.4. Scanning Pattern Approaches: Raster Scan or Lissajous Scan?

After the micro-scanner design and fabrication, a custom confocal microscope setup is construted. In this setup, the input laser beam is manipulated via the motion of the micro-scanner. This directed light beam passes through the optics of the confocal system and scans the specimen with a specific pattern. In order to reconstruct the image of a given target, various scan patterns are available in literature such as raster scan [58], Lissajous scan [59], spiral scan [60] and cycloid scan [61].

Here in this section, the oldest and the most popular scanning technique, raster scan, and the trending method for last ten years, Lissajous scan, which is also the preferred method for scanning in this study, are explained in detail.

2.4.1. Raster Scan

Raster scan is a line-by-line image reconstruction technique commonly used in cathode ray tube (CRT) and television. The pattern of a raster scan is very similar to a person's gaze when reading a book. The word raster comes from the Latin word rastrum (a rake), which is derived from radere (to scrape). In 1880, French engineer Maurice Leblanc was used the term raster scanning in television for the first time [62].

A conventional raster scan involves a triangular pattern in the x-axis while shifting the sample position in steps or continuously in the y-axis and there are two type of raster scan approaches, namely, unidirectional scan and bidirectional scan. As the name implies, unidirectional raster scan works in only one direction which is from left to right. On the other hand, bidirectional method scans the area both from left to right and right to left. One key difference between these two scanning methods is that the vertical distances between the pixel points gets smaller on the edges of the screen for bidirectional scan, whereas it is constant for all pixel points in unidirectional scan. Although unidirectional scan increases the horizontal scanning frequency by two fold, it brings difficulties for the image reconstruction part and requires more precise control on scanning unit. Curious readers may also look at the paper published by Urey et al. [63] for more discussion on these two scanning approaches.

The frame rate of a raster scan is equal to the frequency (f_y) of a signal applied for the y axis. The number of rows (N_{row}) of a raster pattern is determined by the ratio of frequency of the signal applied (f_x) for the x-axis scan to the frequency of the signal on y-axis.

$$N_{row} = \frac{f_x}{f_y} \tag{2.18}$$

In addition, the number of pixels in horizontal axis (N_x) for a raster pattern can be found as follows:

$$N_x = \frac{f_s}{2f_x} \tag{2.19}$$

where f_s is the sampling frequency of the raster scan. On the other hand, the size of a raster scan depends on the amplitudes of the applied signals in x-axis and y-axis.

Let us have a look at the following example in order to visualize applied signals and the resulting raster scan pattern.

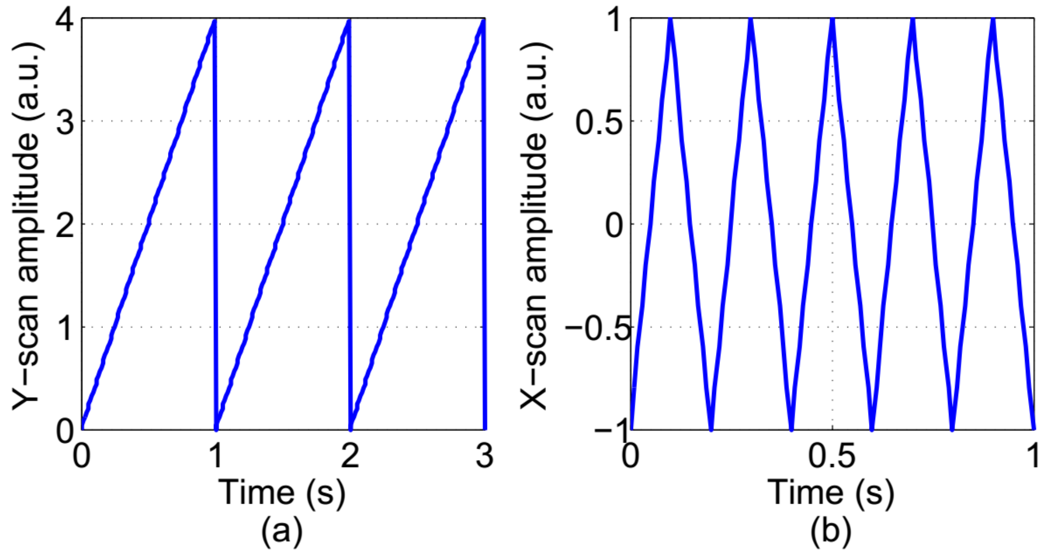

Figure 2.8. Applied signal for horizontal (a) and vertical (b) scan.

In Figure 2.8, a continuous ramp signal with $f_y = 1$ Hz frequency and 4 arbitrary unit (a.u.) amplitude (Figure 2.8a) and a triangular wave with $f_x = 5$ Hz frequency and 1 au amplitude (Figure 2.8b) are generated for y-axis and x-axis scan, respectively. The sampling frequency for both signals are $f_s = 100$ Hz.

The resulting bidirectional and unidirectional raster patterns are provided in Figure 2.9a and 2.9b, respectively. Note that, the red marks are the data points or pixel locations.

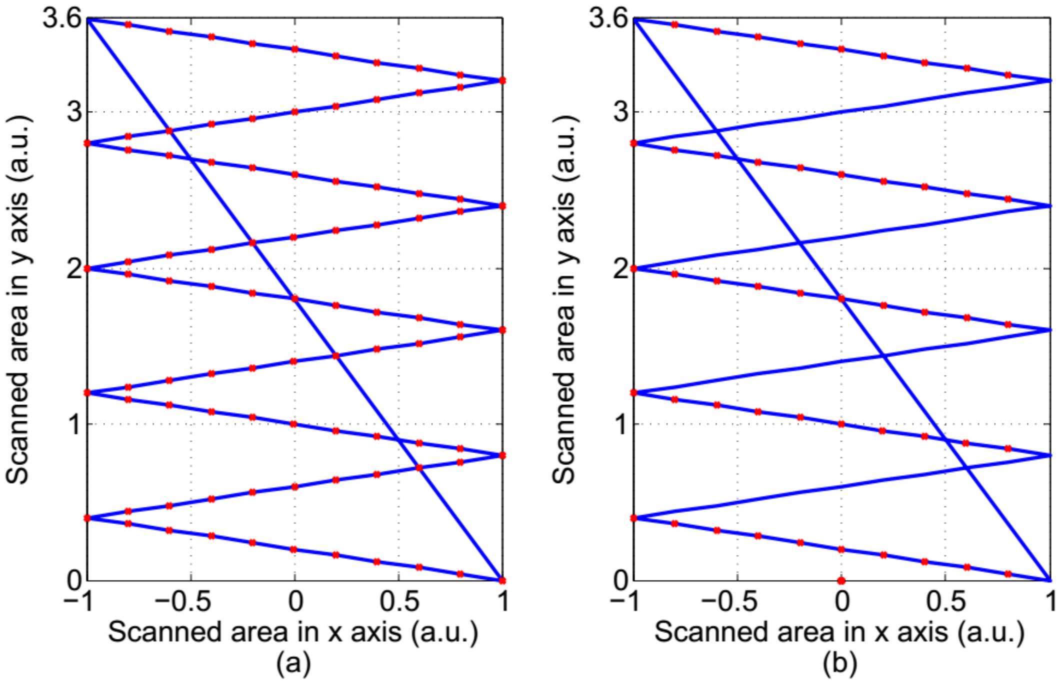

Figure 2.9. Bidirectional (a) and unidirectional (b) raster scan patterns for the signals provided in Figure 2.8.

The unidirectional raster scan trajectory starts at the top left corner of the image (Figure 2.9b). After the signal reaches the limit of the x-axis scan at the right side, it moves lower left to scan the next line of the image. Finally, when the ramp signal of y-axis starts to repeat itself, the raster pattern goes back to its initial point from bottom right to top left as seen in Figure 2.9b. Bidirectional raster scan pattern provided in Figure 2.9a. As previously explained, this method scans the area both from left to right and right to left and it repeats itself as in the bidirectional case.

For unidirectional scan, the number of scanned rows is equal to 5 from the ratio given in Equation 2.18 and it is two times more for bidirectional scan. The number of pixels in one row is the same for both types of scan and it can be found equal to 10 using the Equation 2.19 for the given values of $f_s = 100$ Hz, and $f_x = 5$ Hz (Figure 2.8b).

In reality, in order to increase the number of pixels in one row, an imaging system with high sampling frequency is desired. Moreover, the ratio of the fast scan to the slow scan should also be high enough to scan as many rows as possible. The designed resonant micro-scanners in this study do not provide high ratio between fast and slow scan and also when they are driven with DC or some other frequencies other than resonant ones, their deflections drastically reduces. Thus, they are not suitable to be used in a raster scan fashion.

2.4.2. Lissajous Scan

Lissajous scan is originated after Lissajous curves in mathematics. This interesting curves was examined by Nathaniel Bowditch in 1815, and later extensively by French physicist Jules Antoine Lissajous in 1857. Lissajous curves are governed by the following equations:

$$x = Asin(w_x t + \phi) \tag{2.20}$$

$$y = Bsin(w_y t) \tag{2.21}$$

where, A and B are the amplitudes, w_x and w_y are the angular frequencies of the sinusoidal signals for x and y axes, respectively. Also, ϕ is the phase difference between these two signals. The xy graph of these functions gives Lissajous curves which is described as complex harmonic motion. The ratio of the angular frequencies is defined as follows and it has a significant impact on the shape of curves.

$$N = \frac{w_x}{w_y} \tag{2.22}$$

As illustrated in Figure 2.10, while the value of N decreases down to 1, the filled region on the graph is increases for the case when the phase difference is equal to zero. Note that each graph has the same total area.

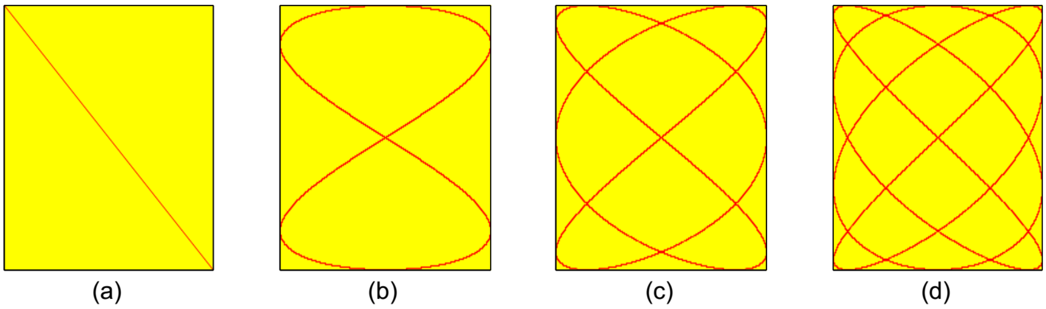

Figure 2.10. Lissajous curves for different N values when $\phi = 0$. (a) N=1 (b) N=2 (c) N=$\frac{3}{2}$ (d) N=$\frac{4}{3}$.

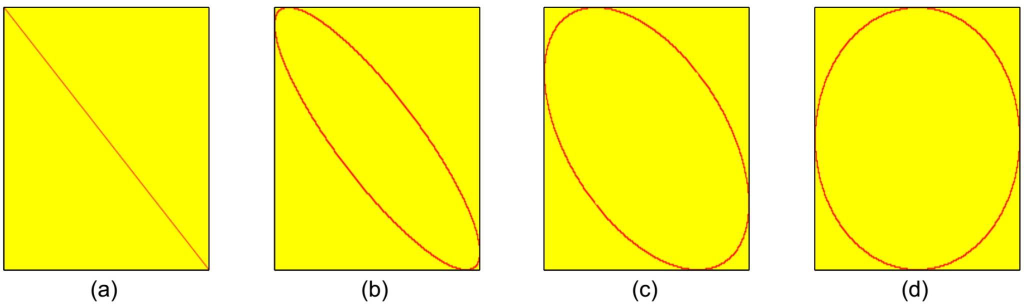

Figure 2.11. Lissajous curves for different ϕ values when N=1. (a) $\phi = 0$ (b) $\phi = \frac{\pi}{6}$ (c) $\phi = \frac{\pi}{3}$ (d) $\phi = \frac{\pi}{2}$

On the other hand, the value of the phase difference also effects the shape of the Lissajous curve as demonstrated in Figure 2.11. Again, the size of the graphs are equal to each other.

Now, let us consider the application of Lissajous curves for image reconstruction. Suppose that the focused beam on the sample is steered with the sinusoidal functions. Then, the pixel locations (x(t),y(t)) of the reconstructed image in x and y coordinates are described with the following expressions [64]:

$$x(t) = \frac{1}{2}X\left[sin(2\pi f_x t + \phi_x) + 1\right] \tag{2.23}$$

$$y(t) = \frac{1}{2}Y\left[sin(2\pi f_y t + \phi_y) + 1\right] \tag{2.24}$$

where, X and Y are the maximum values of FOV in x and y axes in pixel units (p.u.) and f_x and f_y are the driving frequencies of the light manipulating micro-scanner device. Moreover, ϕ_x and ϕ_y are the phase shifts of the applied sinusoidal signals. An important parameter, the pattern repeat rate of a Lissajous scan, is given as follows [64]:

$$f_p = \frac{f_x}{n_x} = \frac{f_y}{n_y} \tag{2.25}$$

where, n_x and n_y are the smallest integers that satisfies the equation above. Greater values of n_x and n_y will increase the amount of lines scanned across the FOV over one completion of the Lissajous scan. The Equation 2.25 also implies that an increase in line density intrinsically decreases the pattern repeat rate. When the frame rate (f_r) is made equal to (f_p), and it is generally the case, there exists a trade-off between fill rate and frame rate. This discrepancy is best explained with an illustrative example.

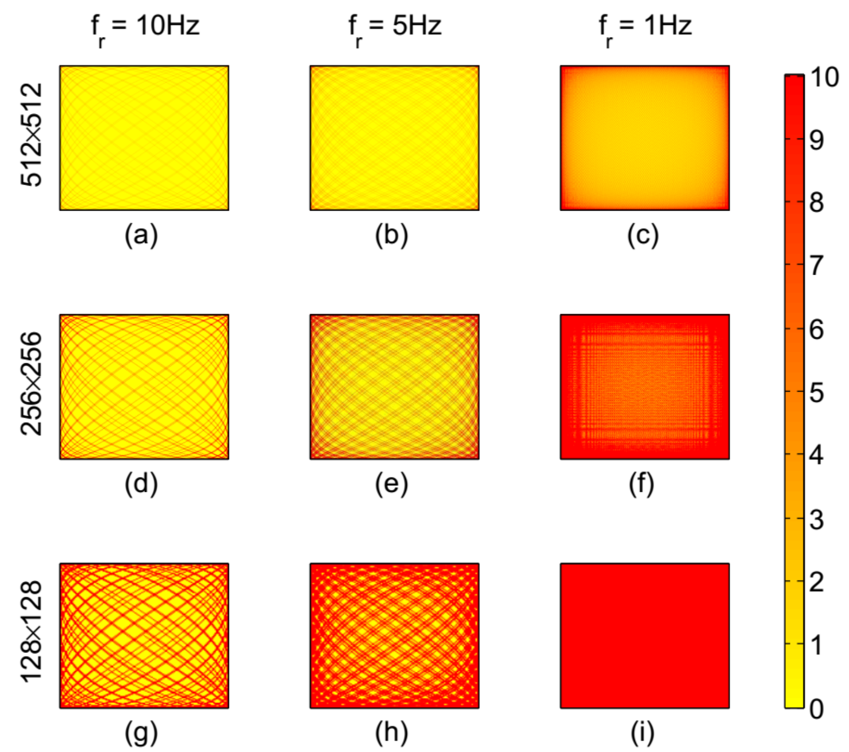

Figure 2.12. Lissajous patterns for various pattern repeat rates and pixel sizes for constant scan frequencies (f_x=301Hz, f_y=249Hz). The color bar denotes the number of times a given pixel is visited before one cycle of the Lissajous scan finishes. Image sizes are given on the left in pixel units (p.u.).

Figure 2.12 shows MATLAB simulations of Lissajous patterns for a pair of constant scan frequencies f_x=301Hz and f_y=249Hz which are comparable with the resonance frequencies of a polymer scanner [17]. The sampling frequency is taken as f_s=1MHz. Here, each row has the same image size and each column has the same frame rate (f_r) as given at the left and on the top of the figure, respectively. It is clear that as the frame rate decreases or the size of the image reduces, the fill rate of the Lissajous scan increases and the numerical results are provided in the table below.

Table 2.2. Percentage fill rates of Lissajous patterns for each sub image given in Figure 2.12.

		Frame rate (Hz)		
		10	**5**	**1**
Image size (p.u.)	**512**	16.95	31.39	63.31
	256	33.19	57.46	94.23
	128	54.50	82.98	100.00

As a result, Lissajous scan is practical when the driving signals of a micro-scanner are high and are mutually prime in order to cover most of the area on the image in minimum time.

Using Lissajous trajectories has paved the way for rapid imaging in atomic force microscopy and multiphoton microscopy [65, 66] through providing a preview of the entire scanned area, in contrary to spiral or raster scanning that only show a limited portion of the FOV, within a fraction of the overall scan time. Owing to its improved speed, Lissajous trajectories were also utilized in rapid ablation of tissues [67]. Coupled with image interpolation algorithms, 2D Lissajous scaning has been demonstrated to provide an unprecedented frame rate of 1 kHz [68].

2.5. Gaussian Beam Optics

In order to determine the depth-of-focus, depth-of-field and to obtain the radius of the beam values from the experimental setup for axial scan, the following expressions will be recalled in the next subsections. A Helium-Neon laser source is used in our axial scan setup and in our simulations that offers TEM_{00} mode which has a Gaussian intensity profile.

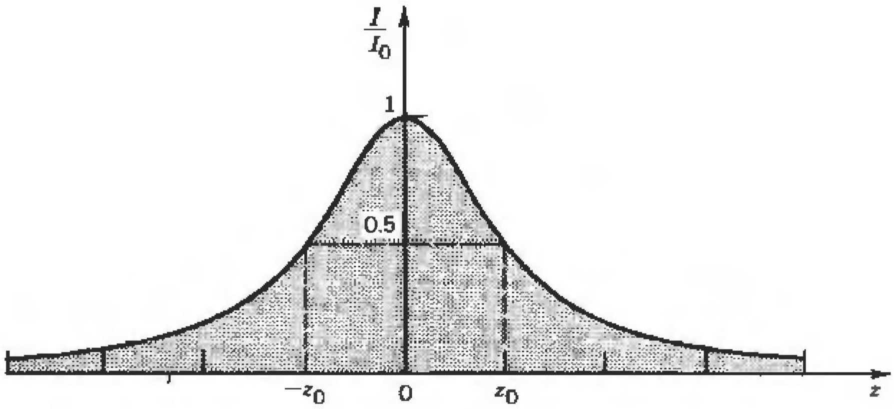

Figure 2.13. The normalized beam intensity I/I_0 at points on the beam axis (r=0) as a function of z [13].

The spatial distribution of the electric field magnitude (Figure 2.13) for the Gaussian beam intensity ($I(r, z)$) is given by the following equation [13]:

$$I(r, z) = I_0 \left(\frac{w_0}{w(z)}\right)^2 \exp\left(\frac{-2r^2}{w^2(z)}\right) \tag{2.26}$$

where I_0 is the intensity at the center of the beam at its waist, w_0 is beam waist that is the minimum value of the spot size, $w(z)$ is spot size, $r = \sqrt{x^2 + y^2}$ is the radial distance from the $z-$axis and the z is the distance along the direction of propagation. Now, let's consider a typical Gaussian function:

$$f_{\text{gaussian}}(y) = \frac{1}{\sqrt{2\pi\sigma^2}} \exp\left(\frac{-(y-\mu)^2}{2\sigma^2}\right) \tag{2.27}$$

where μ is the mean, σ is standard deviation, and σ^2 is the variance. FWHM of this Gaussian function is defined as follows:

$$\mathrm{FWHM} = 2\sigma\sqrt{\ln 2} \tag{2.28}$$

Therefore, the spot size of the Gaussian beam intensity can be expressed as some ratio of FWHM.

$$w(z) = \frac{\mathrm{FWHM}}{2\sqrt{\ln 2}} \tag{2.29}$$

The relation between beam radius (spot size) and the corresponding axial position, z, is given as [13]

$$w(z) = w_0\sqrt{1 + \left(\frac{z}{z_R}\right)^2} \tag{2.30}$$

As mentioned above, the spot sizes are individually measured for all axial positions as z values are changing. After obtaining $w(z)$ values for different axial positions, derived beam radius dataset fit into a curve that is modelled with Equation 2.30 where z_R is called Rayleigh length and w_0 is the minimum beam waist. The irradiance of the beam drops half of its maximum value at Rayleigh range and two times of this parameter is called depth-of-focus [13].

$$I(r,z) = I_0\left(\frac{w_0}{w(z)}\right)^2 = \frac{I_0}{1 + (z/z_0)^2} \tag{2.31}$$

3. 3D POLYMER BASED PRINTED MICRO-SCANNER FOR CONFOCAL MICROSCOPY

In this chapter of the thesis, a magnetically actuated micro-scanner is fabricated via 3D printing technology to use it in LSCM application.

As previously mentioned in Chapter 1, first confocal microscopy systems were using the principle of moving the specimen. These systems were very slow and prone to image distortions. The idea of steering the beam instead of moving the target gives rise to the development of galvanometer scanners [69, 70]. These devices bring significant improvements in vibration reduction, accuracy, and speed, when compared to moving stage designs. There are two types of galvanometer scanners, namely servo-controlled and resonant. Servo controlled galvano scanners have a closed loop control mechanism and this control system offers a very precise movement; however, they have rather slow frequency around 1 kHz [71]. On the other hand, resonant galvo scanners provides high frequencies between 4-16 kHz but they are inherently noisier than traditional galvanometers and generates worse quality images as compared to the servo-controlled ones.

As the technology advances, MEMS scanners are built various kind of materials such as silicon, stainless-steel, piezo-electric, polymer, etc. These scanners are more compact as oppose to the bulky galvanometers and can be integrated into endoscopic microscopy systems. Even though various structural materials are present for fabrication, a great majority of the micro-scanners are getting implemented using planar microfabrication processes, irrespective of the material, which restricts shaping the profile of these devices, in turn limiting their performance. To get a low-cost, deformable micro-scanner having low stress distribution hence long life time, one can resort to additive manufacturing process such as 3D printing.

3D printing technology is gaining more and more popularity in diverse research areas ranging from robotics to biomedical engineering. Different kind of sensors and actuators are fabricated for various applications. Two different kinds of force sensors are fabricated via this fabrication process which are used for robotic manipulation (Figure 3.1) and robotic catheter instrument (Figure 3.2) [14, 15].

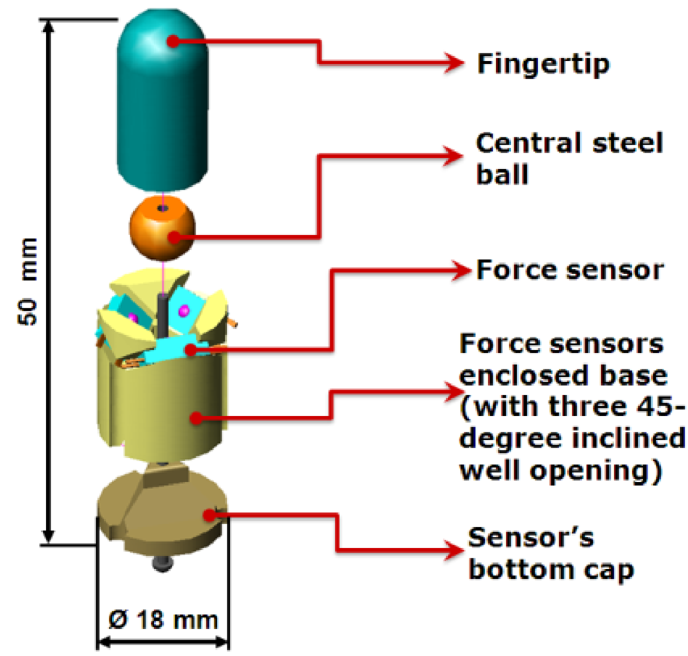

Figure 3.1. 3D CAD model of the fingertip sensor [14].

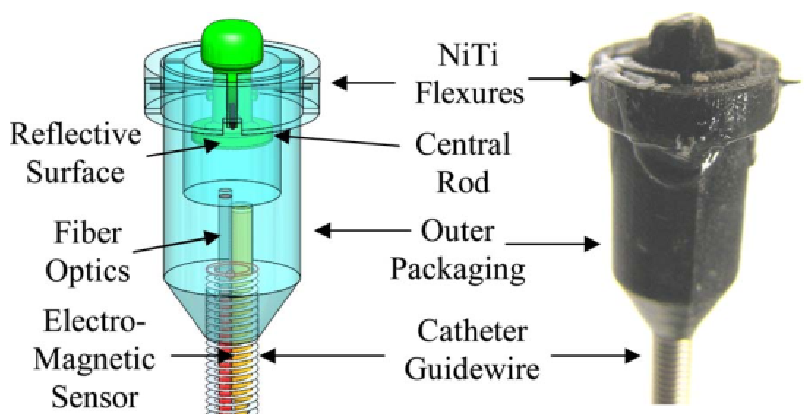

Figure 3.2. Solid model of the 3D printed sensor integrated with the catheter and EM tracker and images of the assembled sensor. [15].

The fingertip sensor, seen in Figure 3.1 is consist of five components, namely, a fingertip (can be coated with silicone rubber), a plated central steel ball, a force sensor enclosed base, a cantilever-bolt mounted bottom cap, and three force sensors (Honeywell FSS015WNSX). The central steel ball (9.4 mm in diameter), force sensors and all the other parts were 3D printed by the Dimension BST 768 (Stratasys Corp., Eden Prairie, MN) within one hour, except the extended cantilever-bolt (a M2.5 steel screw). Using this device, they measured the direction of contact forces in the radial plane of the fingertip sensor.

The outer packaging part of the force sensor, seen in Figure 3.2, is fabricated by The Objet Connex500 3D printer (Objet Geometries Ltd., Billerica,MA). Minimum resolution of the 3D printing device is 16 μm and it can print a range of photopolymers from a stiff acrylic plastic to a rubber-like flexible plastic. The base material of the fabrication is Veroblack photopolymer because it is a stiff plastic (2 GPa) with a high tensile strength (50 MPa). Moreover, this material is opaque, therefore, minimizes the light transmission through the sensor packaging that could potentially impact the fiber optic transducer signal.

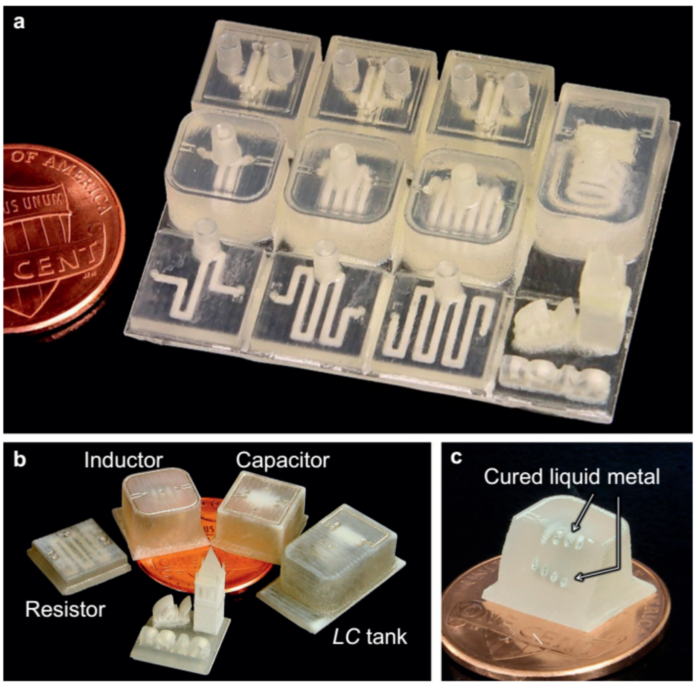

Figure 3.3. (a) 3D printed microelectronics components without the embedded conductive structure. (b) Fabricated 3D components. (c) 4-turn solenoid coil. [16].

Passive wireless sensors (Figure 3.3) are constructed with embedded electrical components such as resistances, inductors and capacitors [16]. Capacitive sensors are arbitrarily formed with additive manufacturing [72]. Quantum dot-based light emitting diodes are also 3D printed with diverse classes of materials [73].

In this chapter of the thesis study, 3D printing technology is used for implementation of the device because this method offers added flexibility in controlling the cross-sectional profile as well as the stress distribution compared to the traditional planar process technologies. Moreover, polymer based 3D printing technology has pretty simple fabrication routine as compared to the lithography steps used in silicon devices.

Proposed device consists of a circular suspension holding a rectangular mirror and can generate a 2D scan pattern. Stress distribution along the circular-profiled flexure is compared with a rectangular counterpart in finite element environment. Magnetic actuation mechanism of the scanning unit is explained in detail. Moreover, reliability of the scanner is tested for 3×10^6 cycle. The scanning device is designed to meet a confocal microscopy application providing 100 μm $\times$ 100 μm field-of-view and less than 3 μm lateral resolution. The resonance frequencies of the device were analytically modeled, where we obtained 130 and 268 Hz resonance values for the out-of-plane and torsion modes, respectively. The scanning device provided an optical scan angle about 2.5 degrees for 170 mA drive current, enabling the desired field-of-view for our custom built confocal microscope setup. Finally, imaging experiments were conducted on a resolution target, showcasing the desired scan area and resolution.

3.1. Optical Design

With the integration of the 3D-printed scanning unit into the custom built confocal microscope, we wish to accomplish i) A resolution better than 3 μm resolution for sub-cellular imaging capability and ii) 100 μm $\times$ 100 μm FOV which is equal to state-of-the-art benchtop laser scanning microscopes [37, 74].

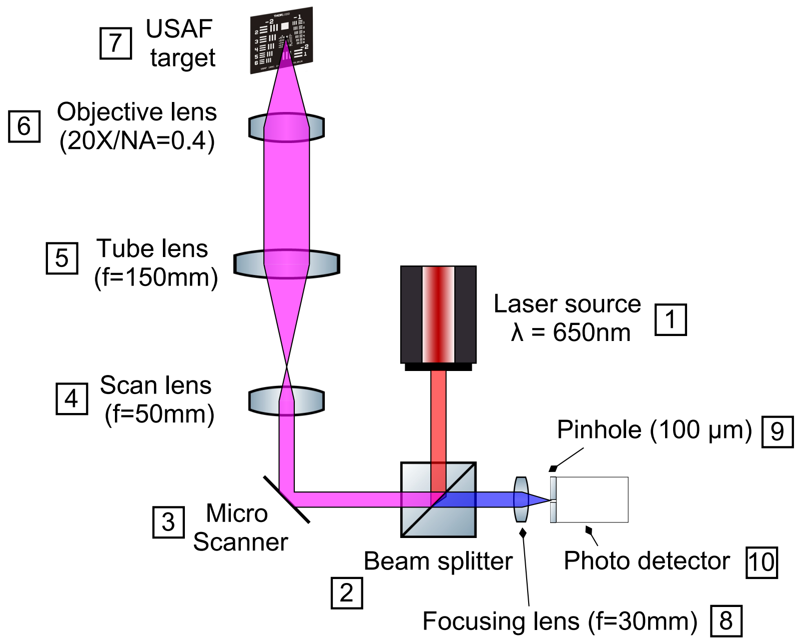

Figure 3.4. Schematic of the custom-built confocal microscope for 2D imaging.

Table 3.1. Parametric distances between the optical components in 2D imaging setup (Figure 3.4)

Pair	1-2	2-3	3-4	4-5	5-6	6-7	2-8	8-9
Symbol	d_1	d_2	d_3	d_4	d_5	d_6	d_7	d_8

The optical architecture of our custom-built confocal microscope in which 3D printed scanner is integrated for 2D imaging is illustrated in Figure 3.4. The setup consists of a fiber-coupled laser (Thorlabs/ITC 4001) that is directed onto the scanning unit via a beam splitter. The scanner plane is relayed onto the objective lens (Olympus/PLN20x), which focuses and collects light to / from the target, via a lens pair that impose a $\times 3$ magnification to the applied input beam diameter. The light is finally epi-collected onto a photomultiplier unit (Hamatsu/H10721-20), after getting focused onto a 100 μm pinhole to eliminate out-of-focus light from the target.

In this confocal setup, the distances from laser source, micro-scanner and focusing lens to the beam splitter, denoted by d_1, d_2 and d_7 (Table 3.1), are kept small as small as possible to reduce the cumulative error stems from misalignments in the optical setup. For a typical red light laser source ($\lambda = 0.65$ μm) with 1.1 mm input diameter, a minimum effective NA of 0.115 is needed for 3 μm resolution. Consider an objective lens (Olympus/PLN20x) having 0.4 NA, focal length of 9 mm and a clear aperture of 10 mm. In order to reach the minimum effective NA (0.115), the clear aperture of the objective must be filled with at least 28 % according to Equation 2.1. If the input beam from the laser is $\times 3$ magnified on the objective lens, it reaches a diameter of 3.3 mm and fills more than 28 % of the objective lens clear aperture and the effective NA becomes 0.132. For the above mentioned conditions in our custom built setup, the spot FWHM diameter at the target can be calculated, via Equation 2.1, as 2.62 μm satisfying our desired lateral resolution of less than 3 μm. The relation between FOV and zero-to-peak optical scan angle is previously explained in Equation 2.2. Therefore, according to the desired FOV of 100 μm with $M = 3$, one needs a zero-to-peak optical scan angle of 1.9 degrees for the specified objective lens having a focal length of 9 mm.

3.2. Mechanical Design & Analytical Calculations

Optical design of device is completed satisfying the targeted constraints. The device is then constructed within a computer-aided-design (CAD) tool. The cross-section of flexure is made circular to reduce the stress at the junction points. In order to use magnetic actuation, pockets are opened to place small circular hard magnets having a diameter and thickness of 3 mm and 1 mm, respectively. Resonant frequency of the structure for the torsion mode can be approximated as a simple harmonic oscillator as shown in Equation 2.4. This composite structure consists of a mirror part and a flexure as shown in Figure 3.5.

The effective MOI of this complex device can be derived by dividing the structure into known objects (Figure 3.6) as explained in Section 2.3. Effective MOI of the micro-scanner can be derived approximately in terms of the distances (Table 3.2) and given

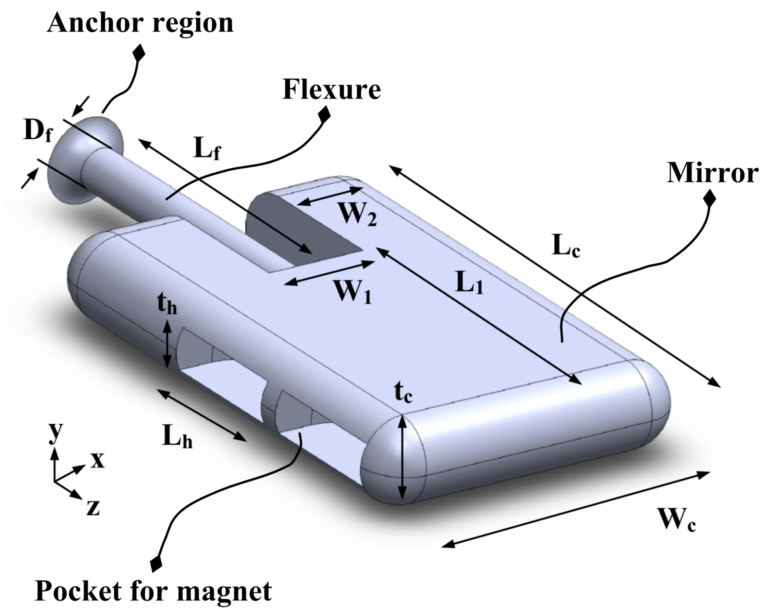

Figure 3.5. Drawing of the micro-scanner parametrically showing its dimensions [17].

Table 3.2. Dimensions of the micro-scanner (all in mm).

Parameter	**Symbol**	**Value**
Diameter of flexure	D_{f}	1
Length of flexure	L_{f}	8
Total length of cantilever	L_{c}	12
Central length of cantilever	L_1	8
Total width of cantilever	W_{c}	8
Inner width of cantilever	W_1	2,5
Side width of cantilever	W_2	1,75
Thickness of cantilever	t_{c}	2
Length of pocket	L_{h}	3
Thickness of pocket	t_{h}	1

Table 3.3. Material properties of VeroClear and Neodymium.

	VeroClear	**Value**	**Neodymium**	**Value**
Young's Modulus	E_v	2.5 GPa	E_n	160 GPa
Density	ρ_v	1045 kg/m^3	ρ_n	7500 kg/m^3
Poisson's ratio	ν_v	0.35	ν_n	0.24

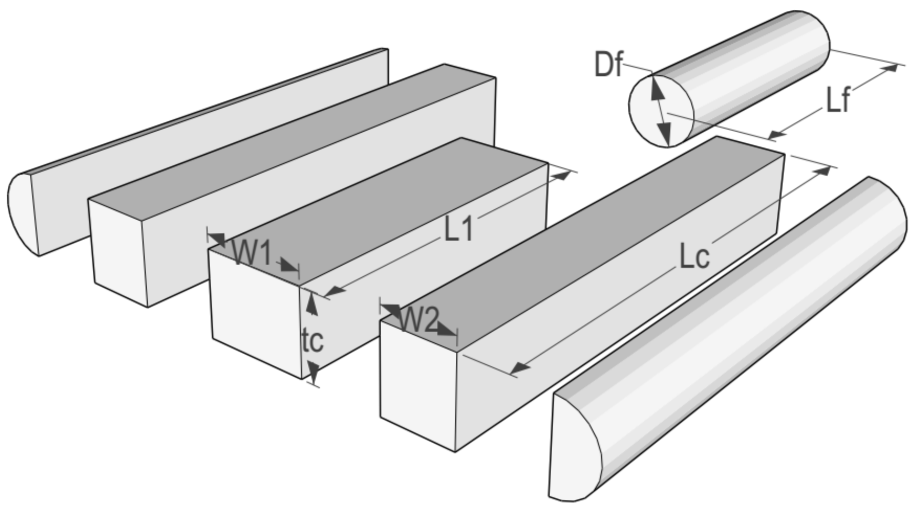

Figure 3.6. Approximated drawing of the designed micro-scanner.

densities of the materials (Table 3.3) as follows:

$$
\begin{aligned}
J_{\text{eff}} = \frac{\rho_v}{6}\Bigg(& L_{\text{c}} W_2 t_{\text{c}} \Big(({W_2}^2 + {t_{\text{c}}}^2) + 3(W_1 + W_2)^2 \Big) \\
& + \frac{3\pi L_{\text{c}} {t_{\text{c}}}^2}{16} \Big({t_{\text{c}}}^2 + 2(W_{\text{c}} - t_{\text{c}})^2 \Big) \Bigg) \\
& + \rho_v \Big(\frac{L_1 W_1 t_{\text{c}}}{12} ({W_1}^2 + {t_{\text{c}}}^2) + \frac{\pi L_{\text{f}} {D_{\text{f}}}^4}{32} \Big) \\
& + (\rho_n - \frac{\rho_v}{2}) \pi t_{\text{h}} {L_{\text{h}}}^2 \Big(\frac{{L_{\text{h}}}^2}{16} + \frac{{t_{\text{h}}}^2}{3} + (\frac{W_1}{2} + W_2)^2 \Big)
\end{aligned} \tag{3.1}
$$

On the other hand, spring constant of a beam with circular cross-section for torsional movement can be found via Equation 2.5 as follows:

$$k_{\mathrm{t}} = \frac{G\pi {D_{\mathrm{f}}}^4}{32L_{\mathrm{f}}} \tag{3.2}$$

where G is shear modulus of the material, D_{f} and L_{f} are the diameter and the length of the flexure, respectively. Whereas, out-of-plane movement of the micro-scanner is the second mode of concern and the resonant frequency of this mode can be calculated using Equation 2.8. Effective mass M_{eff} of the device and spring constant k_{o} for out-of-plane movement and can be derived as follows:

$$\begin{aligned} M_{\mathrm{eff}} &= \rho_v \left(\frac{35}{576}\pi L_{\mathrm{f}} {D_{\mathrm{f}}}^2 + L_1 W_1 t_{\mathrm{c}} + \frac{L_{\mathrm{c}}}{4}\left(8W_2 t_{\mathrm{c}} + \pi {t_{\mathrm{c}}}^2\right)\right) \\ &\quad + (\rho_n - \frac{\rho_v}{2})\pi t_{\mathrm{h}} {L_{\mathrm{h}}}^2 \qquad (3.3) \\ k_{\mathrm{o}} &= \frac{3}{64}\frac{E_v \pi D_{\mathrm{f}}^4}{L_{\mathrm{f}}^3} \qquad (3.4) \end{aligned}$$

As a result, substituting Equations 3.1-3.2 into the Equation 2.4 and using the values provided in Table 3.2 and Table 3.3, natural frequency of the torsion can be found as 260 Hz. Likewise, inserting Equations 3.3-3.4 into the Equation 2.8 and plug in the values given in Table 3.2 and Table 3.3, natural frequency of the device for the out-of-plane is obtained as 134 Hz. Note that, out-of-plane movement of the micro-scanner is modeled as a one end is fixed and the other end is free cantilever and the applied force is assumed as a point force and it is concantrated at the center of mass. Therefore, the length of the flexure is extended to the center of mass and it is taken as $L_f = L_f + 3.5$ mm $= 11.5$ mm.

Both torsional and out-of-plane resonant frequencies are produced by the designed scanner structure, owing to the scanner dimensions and its material properties (Veroclear). Section 3.4.4 will discuss how these frequencies satisfy the desired frame-per-second (FPS) and fill rate requirements for laser scanning microscopy application.

3.3. FEM Simulations

The mode shapes and eigenfrequencies of the micro-scanner are obtained via finite element method (FEM) simulations. Mode shape and the corresponding eigenfrequency determines how the structure vibrates when it is subjected to an external voltage. Before the fabrication process, finite element simulation results give a rough idea about the resonant frequencies of the corresponding mode shapes of the micro-scanners. Structural material of the micro-scanner device is VeroClear has a manufacturer specified density $\rho_v = 1045\,\mathrm{kg/m^3}$ and Young's Modulus $E_v = 2 - 3\,\mathrm{GPa}$ making it a suitable material for low-frequency resonant actuators. In order to model the micro-scanner in finite element simulations, E_v is set to $2.5\,\mathrm{GPa}$ and Poisson's ratio ν_v is assumed to be 0.35 for VeroClear material, which lies in the natural range for polymers. Moreover, the magnets attached to the device are made of Neodymium and the corresponding material properties are summerized in Table 3.3. The mode shapes for the movement

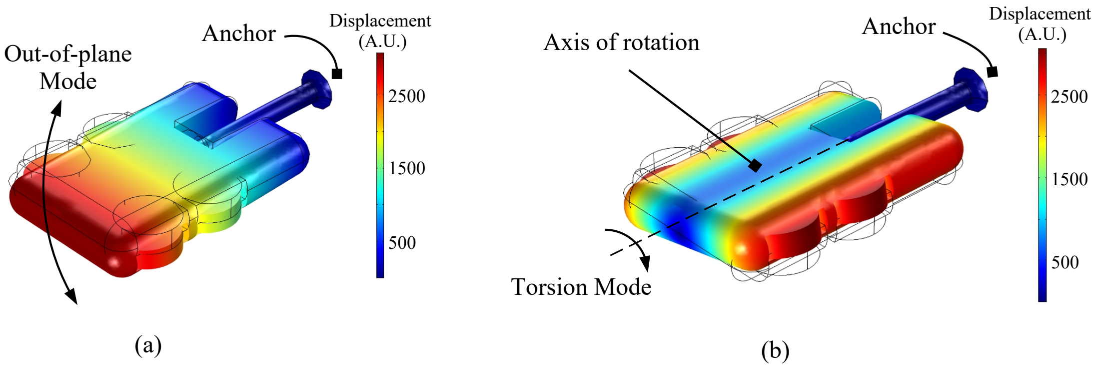

Figure 3.7. (a) Out-of-plane bending at 137 Hz. (b) Torsion at 335 Hz.

of the micro-scanner are shown in Figure 3.7. The combination of the second and the third modes are used to get Lissajous patterns. The first mode of the device is in-plane sliding mode which is not useful for a 2D scan in our optical setup. The second mode of the micro-scanner is out-of-plane bending movement at 137 Hz (Figure 3.7a). Torsion, which is the third mode, around the flexure is observed at 335 Hz (Figure 3.7b).

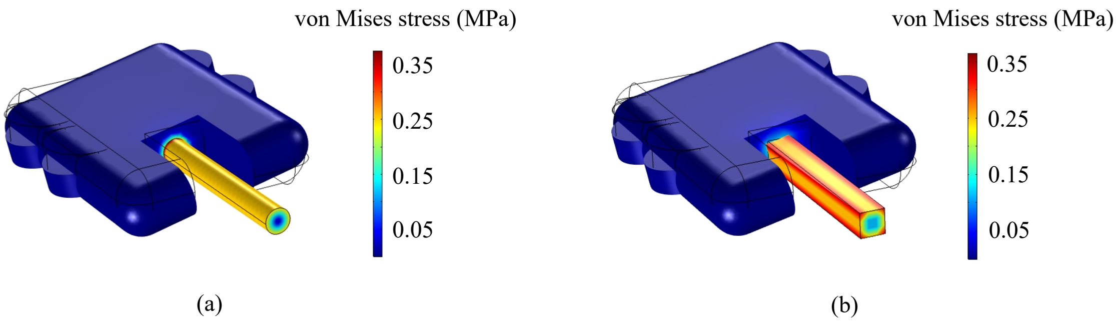

Figure 3.8. Von Mises stress comparison of circular cross section (a) with rectangular cross section (b) [18].

Von Mises stress, which is a value used to determine if a given material will yield or fracture, is expressed with the following equation [75]:

$$\sigma_e = \sqrt{\frac{1}{2}\left[(\sigma_{xx}-\sigma_{yy})^2+(\sigma_{yy}-\sigma_{zz})^2+(\sigma_{zz}-\sigma_{xx})^2\right]+3(\sigma_{xy}^2+\sigma_{yz}^2+\sigma_{xz}^2)} \tag{3.5}$$

where σ_{xx}, σ_{yy}, σ_{zz}, σ_{xy}, σ_{yz} and σ_{xz} are all rectangular components of stress. Von Mises stress distribution on the flexures having a circular and rectangular cross section are compared on the designed device via FEM simulations (Figure 3.8). The length of the flexures fixed to 8 mm and the area of the cross sections are adjusted so that both flexures have the same spring constant for the torsion mode. The applied static force to the devices also adjusted to provide same displacement. While the stress distribution along the flexure with a circular cross section is uniform and around 0.25 MPa, rectangular cross sectioned flexure has a varying stress distribution between 0.25-0.35 MPa. Note that these values are quite less than the yield strength of the base material which has a Young's modulus in the range of 2-3 GPa.

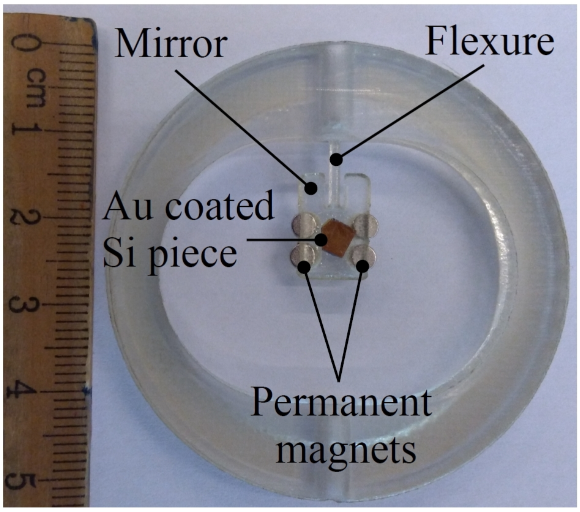

Figure 3.9. Fabricated polymer micro- scanner via 3D printing technology and attached permanent magnets [18].

3.4. Experimental Results

3.4.1. Implementation

3D model designed in a CAD sofware is exported to the 3D printing device. There are several kind of available 3D printing technologies and our device uses photopolymer jetting method. In this approach, solid structures converted into series of thin slices to be physically fabricated layer by layer. Liquid photopolymer material (VeroClear was our preference) is selectively exposed to a UV light source, causing it to cure into a solid object. Polyjet printing technology shares the minimum layer thickness with stereolithography and material jetting techniques. For instance, we used OBJET Eden 260v polyjet printing device which has a axial resolution of 16 μm and a lateral resolution of 40 μm. Polyjet and binder jetting devices offer multi-materials and multi-color parts which makes them advantageous among other 3D printing methods.

Following the fabrication process, small neodymium magnets were embedded into the device via epoxy resin. Moreover, gold-coated silicon piece was glued to the front side of the mirror to have a reflective surface. The micro-scanner is integrated with a

5 cm circular mount that was fabricated using the same material just to facilitate the optomechanical setup of the LSCM (Figure 3.9).

3.4.2. Frequency Response

A characterization setup, which includes an oscilloscope (Tektronix TDS 3032B), signal generator (Tektronix AFG 3101), laser doppler vibrometer (LDV) (Polytech OFV 2500), and PC is used to measure the frequency responses of the micro-scanner as illustrated in the figure below. A GPIB interface provided the communication of

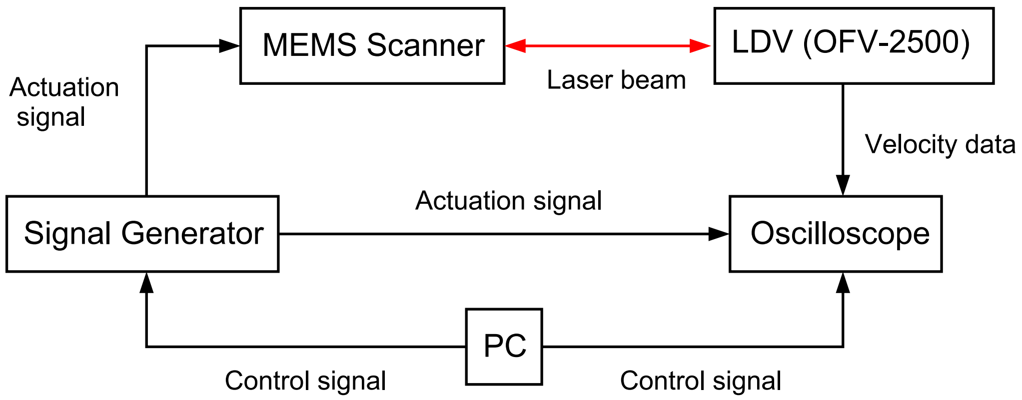

Figure 3.10. Schematic of the characterization setup.

PC with the oscilloscope and function generator. The focusing laser beam coming from LDV hits the section of interest on the micro-scanner. Then, the reflected light from the scanner device returns back to the LDV unit which measures the Doppler shift between the generated reference beam and reflected beam to give a voltage at its output. Using following expression, the displacement values (x(t)) of the micro-scanner are calculated.

$$x(t) = \int v(t)\ dt \tag{3.6}$$

In fact, velocity data is a sinusoidal signal: $v(t) = Asin(wt)$. Therefore, in order to obtain the displacement value for each frequency, the corresponding velocity is divided by $w = 2\pi f$ because of the integral given in Equation 3.6. Note that, the voltage per millimeter over second is adjustable on the LDV device. For instance, if $1V = 100\ mm/s$ is selected, then each voltage value should be multiplied with 100 before the integration process.

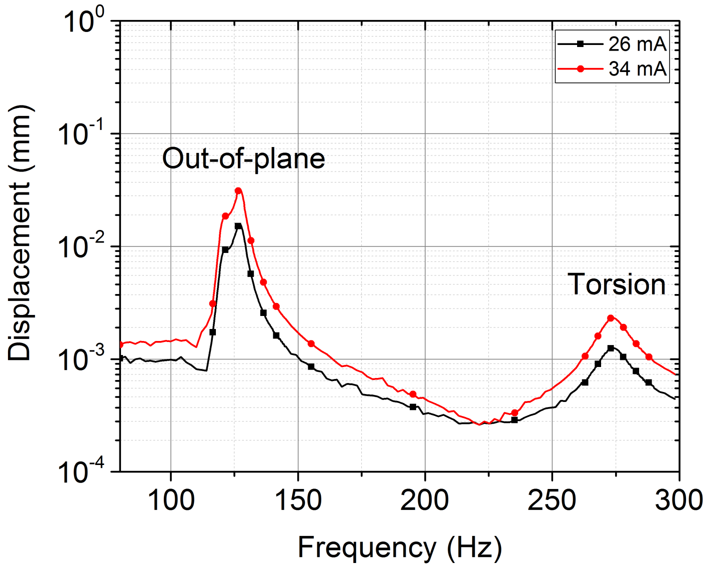

Figure 3.11. Frequency response of the micro-scanner for varying electrocoil current drives [17].

The dynamic deflection of the micro-scanner as a function of frequency is shown in Figure 3.11. The electro-coil is fed with a constant sinusoidal amplitude and by varying frequency of the signal, the vibration velocity values are collected by the LDV in ambient air. As seen in Figure 3.11 the slow resonance peaks of the micro-scanner corresponds to the out-of-plane bending mode are at 127 Hz. At this frequency, micro-scanner generate maximum deflections of 32 μm for a 34 mA current. Moreover, quality factor of the device is around 31 for the out-of-plane movement. Torsion around the flexure is observed at 274 Hz. At this frequency, micro-scanner generate maximum deflection around 2.4 μm. Furthermore, quality factor of the micro-scanner is around 25 for the torsion.

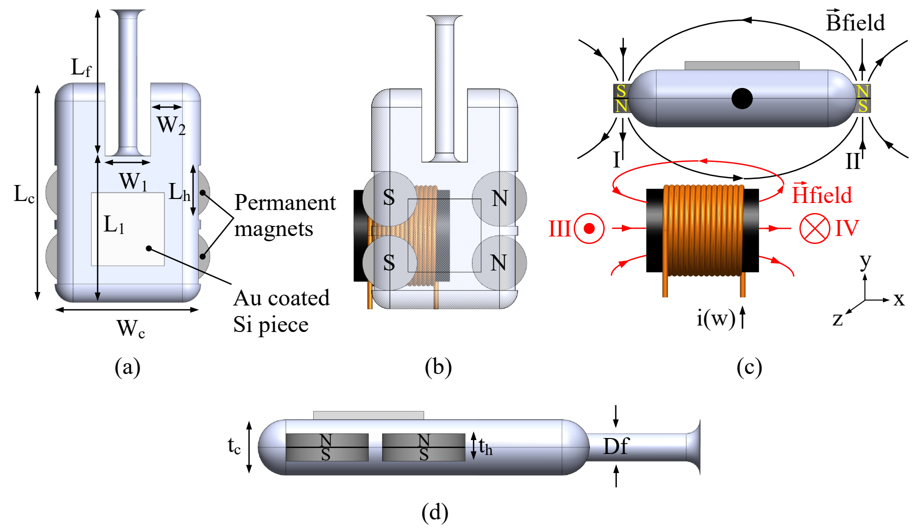

Figure 3.12. Front (a) and side (d) view of the micro-scanner. (b) Position of the coil with respect to the scanner. (c) Magnetic actuation principle schematic of the scanner [18].

3.4.3. Magnetic Actuation Principle, TOSA Results and Reliability Tests

The scanning unit that consists of a circular flexure, and a mirror element in which 4 cylindrical Neodymium magnets (part number N35, remanence $B_r = 1.17$ T, coercivity $H_c = 868$ kA/m) are embedded in for magnetic actuation as illustrated in Figure 3.12. The dimensions were set to enable a compact scanner design that fits within a 5 cm circular mount which is traditionally used in the optomechanical setup of the confocal microscope and they are given in Table 3.2. The design is tailored to provide an out-of-plane bending and torsional modes, combination of which provides a Lissajous scan to address a 2D FOV. Instead of using one magnet on each side of the mirror, two pairs of magnets are placed side by side as in Figure 3.12 in order to increase the magnetic field strength and hence to generate more torque while keeping the thickness of the mirror as low as possible. The actuation of the micro-scanner is realized with the interaction of the H-field, generated by the external coil (inner core diameter: 13 mm, length: 15.4 mm, inductance: 330 μH, 75 copper wire windings) with the B-field of the magnets. The B-field tries to align itself with the H-field in the xy plane results torsion movement about z axis. For the purpose of out-of-plane movement demonstration, consider the H-field vectors in the xz plane denoted by III and IV. These vectors interacts with B-field vectors of I and II creates a clockwise rotation around x axis (Figure 3.12c).

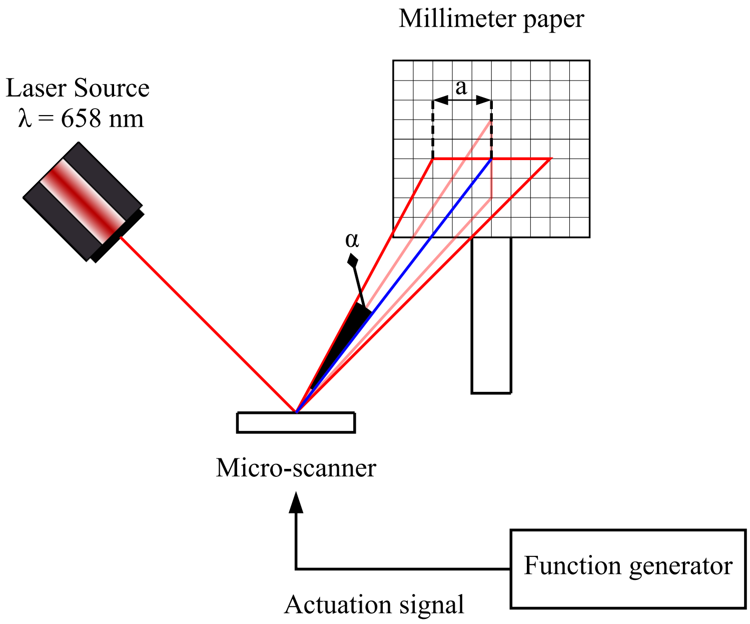

Figure 3.13. Schematic of the TOSA measurement setup.

Total optical scan angles of the fabricated micro-scanner are obtained from the experimental setup given in Figure 3.13. Scanner device is actuated for its resonance frequencies and the length of the scan lines on the millimeter paper are noted. The angle α gives us zero-to-peak-optical scan angle and it can be calculated from $tan\ \alpha = a/L$ where L is the distance from micro-scanner to the millimeter paper which is highlighted by blue (Figure 3.13). As a result, TOSA for horizontal or vertical axis is obtained by multiplying the corresponding zero-to-peak-optical scan angle by two.

The maximum vertical and horizontal scan lines created by LSCM system is shown in Figure 3.14. TOSA of 4.58 and 6.34 degrees are acquired for vertical and horizontal scanning movements, respectively. Finally, a Lissajous pattern has been formed for the vertical driving frequency of 117 Hz and horizontal driving frequency of 262 Hz as can be seen on Figure 3.14c. Reliability of the proposed polymer device

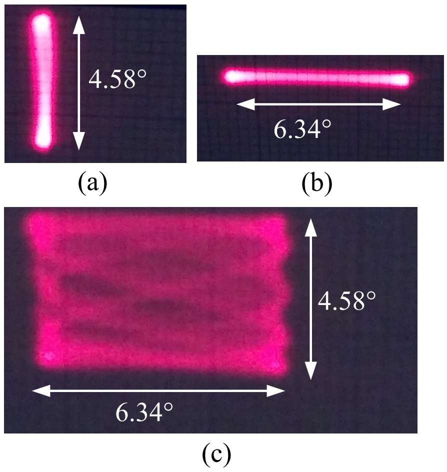

Figure 3.14. TOSA of the vertical (a) and horizontal (b) scan lines and the Lissajous pattern given in (c) for a driving current of 170 mA [18].

is examined by operating it for an extended period of time. The scanner is actuated at its both slow and fast resonant frequencies for approximately 3×10^6 cycles at a drive current of 135 mA, in ambient air. Scanner's resonant frequencies are measured periodically during the experiment. Figure 3.15 indicates the measured percentage change in each measured parameter. For both of the resonance frequencies, maximum deviation is found below 2.5 %.

3.4.4. Implications of the Micro-Scanner Frequency Response on Frame-Rate

We investigate the fill-rate and frame-rate achieved with the observed scan frequencies, for the desired spot size of 2.66 μm and FOV of 100 μm $\times$ 100 μm. As shown in Figure 3.16, horizontal and vertical frequencies for (a)-(d) and (e)-(h) are f_{x} = 100 Hz, f_{y} = 250 Hz and f_{x} = 127 Hz, f_{y} = 262 Hz, respectively. Frame rates from (a) to (d) and from (e) to (h) are 20, 10, 5 and 1 Hz. Fill rates for (a)-(d) are %31.8 and from (e) to (h) are %64.7, %80.5, %99 and %100, respectively. Keep in mind that in Lissajous scan, the coverage improves at mutually prime orthogonal scan frequencies, at the expense of reduced frame rate to 1 Hz. However, the micro-scanner

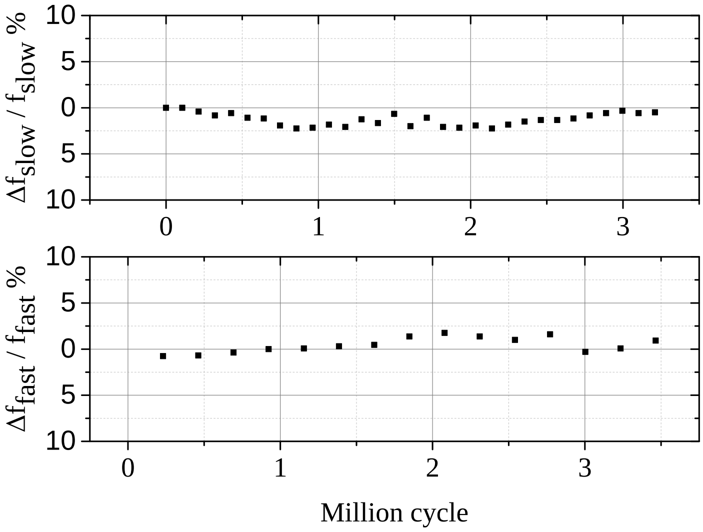

Figure 3.15. Reliability test results of the fabricated scanner [18].

can be operated with a non-repeating sub-frame rate Lissajous algorithm to significantly improve the frame rate with some compromise in the fill rate of the scanned image [67]. Note that frame and fill-rate analysis based on measured values in Section 3.4.2, as opposed to analytical values derived in Section 3.2. Owing to the quality factor of the micro-scanner for both vibration modes, one can slightly tailor the scan frequencies for optimal Lissajous coverage. Driving the micro-scanner at or near its resonance frequencies and by taking FOV and lateral spot size into account, one can obtain the coverage (fill-rate) patterns, in which color codes represents how many times each resolvable spot is visited. For example, assuming that the natural frequencies of the orthogonal movement of the micro-scanner are 100 and 250 Hz (non-mutually prime) for the given FOV (100 μm $\times$ 100 μm) and spot diameter 2.66 μm, one obtains the Lissajous patterns as shown in Figure 3.16a. Note that the coverage does not improve with reduced frame-rate (Figure3.16(b-d)) for the set of non-mutually prime frequencies, as the scan time is very low in duration. On the other hand, simulations based on measured resonance frequencies of 117 and 262 Hz, reveal a dramatically increased fill-fate, as illustrated in Figure3.16h at the expense of reduced frame rate. Yet, increasing the frame-rate still results in appreciable amount of coverage of the FOV, which could be further compensated through various interpolation algorithms [68].

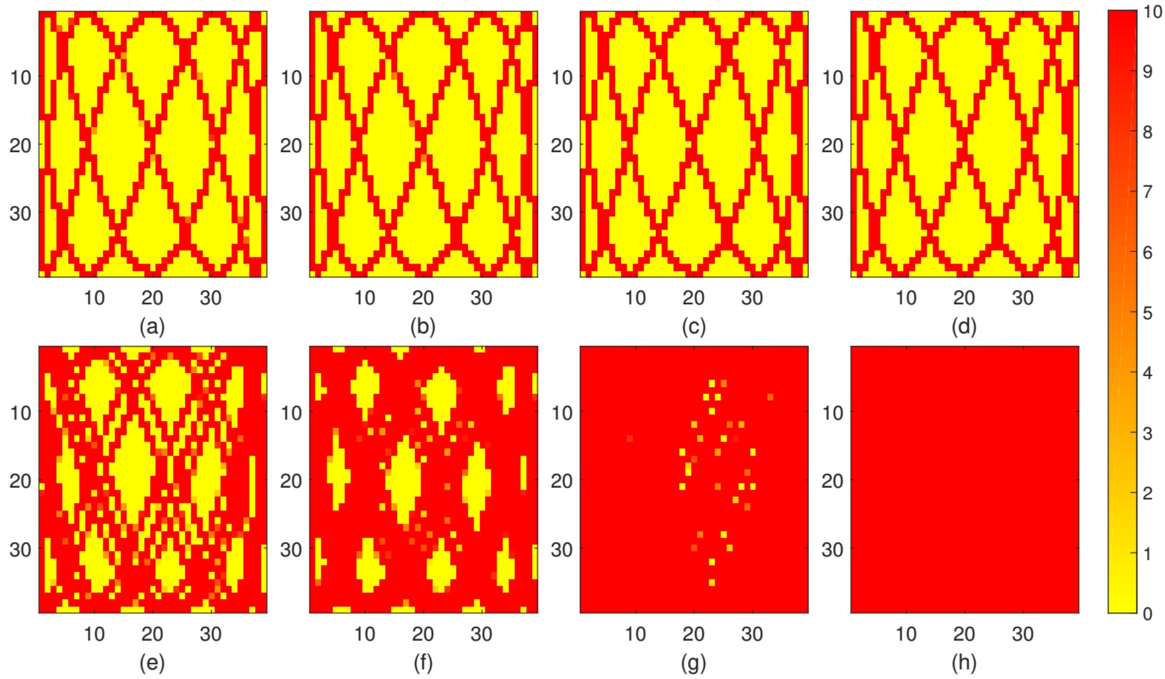

Figure 3.16. Lissajous patterns for various scan frequencies and frame rates for a constant FOV of 100 μm $\times$ 100 μm [18].

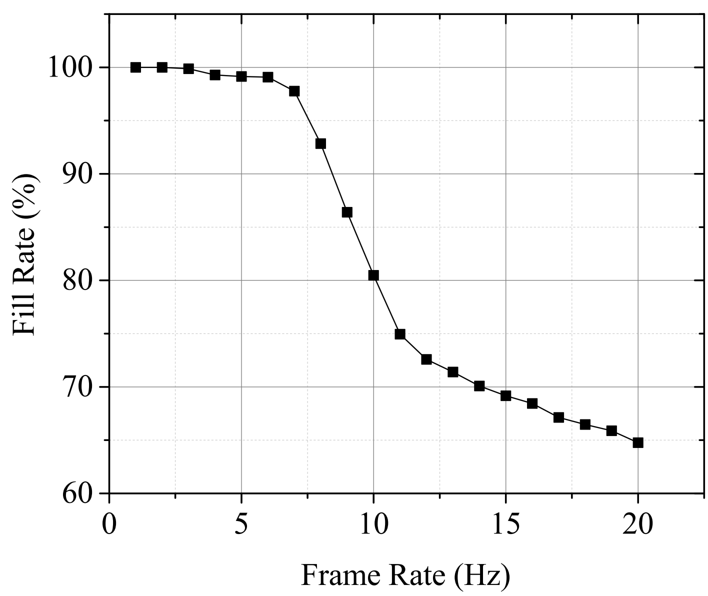

Figure 3.17. Percentage fill rates of Lissajous scan patterns for different frame rates and targeted FOV: 100 μm $\times$ 100 μm [18].

Figure 3.17 illustrates the fill-rate vs. frame-rate based on the actual resonance frequencies (117 and 262 Hz) of the micro-scanner, for the FOV of 100 μm $\times$ 100 μm. While the fill-rate reduces for increased frame rates (reduced scan durations), it approaches 100 percent at larger scan durations (lower frame-rates). Based on fill-rate frame-rate trade-off, scan duration can be set based on the content of the target image. Low spatial content, sparse targets may be imaged with great speeds, with the aid of interpolation operation. Meanwhile, high spatial-content images should be acquired at low frame-rates ensuring acquisition of all the details within the FOV. Our findings reveal that, approximately 65% of the FOV is visited by the laser, when operated at a frame rate of 20 Hz.

3.4.5. Image Acquisition

The micro-scanner was driven with a root-mean-square current of 170 mA at its resonance frequencies of 117 and 262 Hz. The sampling time and the total acquisition time were 1 μs and 1 s, respectively. Electrocoil position is altered with respect to the scanner to establish a near-square shape FOV.

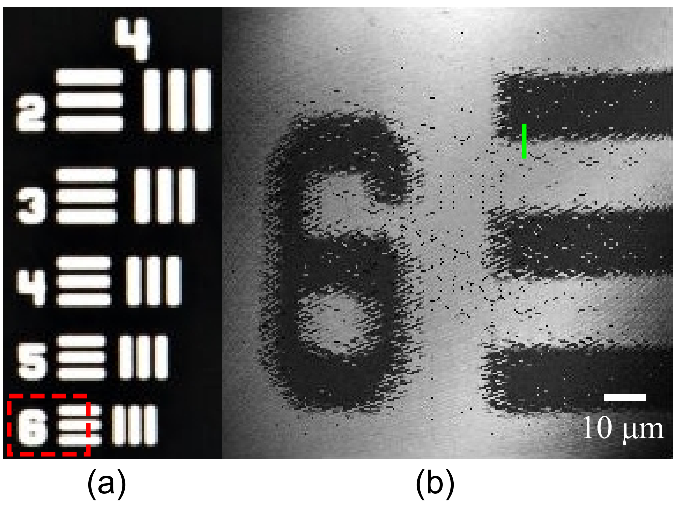

Figure 3.18. (a) Thorlabs negative 1951 USAF resolution target. (b) The image of the stripes of element 6 in group 4. FOV is 105 μm $\times$ 105 μm [18].

In order to observe the imaging performance of the microscope system, a United States Air Force (USAF) resolution target was placed at the focus, where element 6 of group 4 was imaged via home-built software that assisted the setup. As the line width of the featured group is 17.5 μm, the FOV was estimated to be 105 μm $\times$ 105 μm, which is slightly more than our expected FOV of 100 μm $\times$ 100 μm (Figure 3.18b).

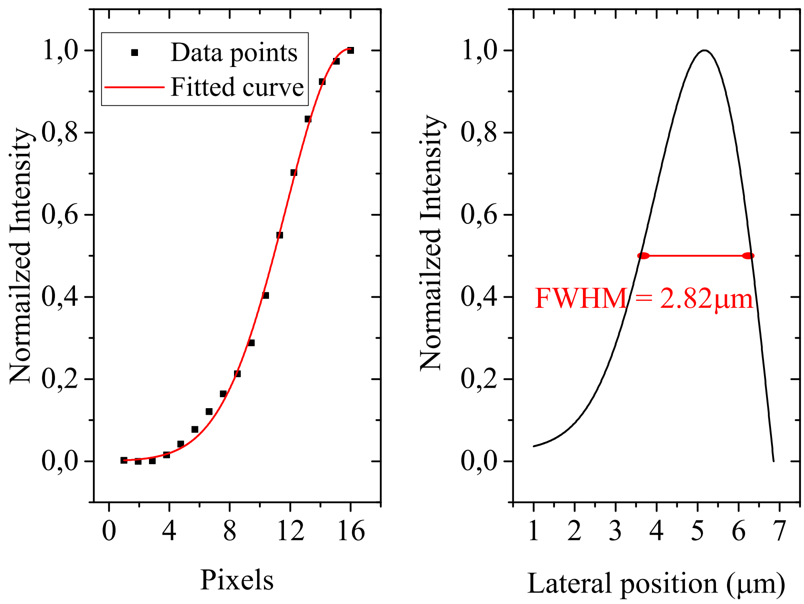

Figure 3.19. FWHM resolution of the target. a) Line profile along the green line in Figure 3.18b. b) Derivative of the fitted curve in (a) [18].

Furthermore, the resolution was specified using the profile of a step, which corresponds to the green line that is acquired in Figure 3.18b. Optical resolution of the system can be found by evaluating the derivative of the step that corresponds to the impulse response of the system. FWHM resolution based on Figure 3.19 is calculated as 2.82 μm which is in good agreement with our theoretical prediction of 2.66 μm.

The performance of our system is compared with a commercial microprobe as in Table 3.4. Fabricated scanner produces a 105 μm $\times$ 105 μm square having a 2.82 μm diameter spot size (corresponding to a 38 $\times$ 38 image). Although this resolution is below that can be produced by the state-of-the-art MEMS [37] and galvanometric scanner [76], the designed and manufactured device offers desired specifications for laser

Table 3.4. Performance comparison of our system with a commercial product (Cell Visio unit [22], Mauna Kea Technologies) [18].

	Off-the-shelf confocal endo/microscopy system (Cell Visio unit)	**3D-printed scanner based confocal endo/microscopy system**
Lateral resolution	1.4-3.3 μm	2.8 μm
FOV	240-600 μm	100 μm
FPS	9-12 fps	10 fps with %80 coverage
Cost of scanning unit	2100 euros	10 euros
Manufacturing	Complex and slow	Simple and fast

scanning microscopy, at a much lower cost, compact volume (as opposed to galvanometric scanner), and easier fabrication routine. Moreover, FOV of the fabricated device can be improved by using a different material or some combination of two different materials. Also, a mixture of NaOH and water can be used to release the support material of the 3D printing device which prevents us to reduce the crossectional diameter of the flexure.

4. LASER-MACHINED STAINLESS-STEEL MICRO-SCANNERS FOR CONFOCAL MICROSCOPY SYSTEMS

The micro-scanners used in LSCM systems have various topologies and been built using different kind of structural materials, for improved scan angle, imaging and stress performance [77]. The choice of fabrication material is crucial in lowering the cost of these micro-scanners. MEMS based micro-scanners reported in handheld LSCM system applications mainly use Si as the main fabrication material [78–80]. Fire Retardant 4 (FR4) based micro-scanners, which are actuated magnetically, implemented for barcode scanning application, are shown in literature [81]. Furthermore, micro-scanners that use polymer as the structural material have been implemented for display applications [82]. Electrical discharge machining is used as a micro-machining technique to produce an stainless steel based micro-scanner which is integrated in a two-photon hyperspectral fluorescence microscope [83]. Electrochemical etching is another fabrication method used on stainless steel to create a micro-scanner [84] and this device is used in a two-dimensional display.

In this chapter, there are three different studies and in each of these works, a laser-machined stainless-steel micro-scanner is designed, fabricated and utilized for a specific confocal microscopy application. Stainless-steel (grade:430) is preferred as structural material for scanner devices because of its high relative magnetic permeability property to attain larger deflections in a magnetic actuation mechanism. Moreover, these micro-scanners have higher resonant frequencies than the previously reported 3D polymer printed counterparts. Besides, laser micro-machining technology is chosen as a manufacturing method due to its low cost and it enables the fabrication of fine detailed structures with high accuracy and fast production speed.

In the first part, the micro-scanner is designed, fabricated, characterized and used in a 2D confocal imaging application. In the following study, another micro-scanner is designed and produced for 3D Lissajous confocal imaging application. This device can work in three different out-of-plane modes in order to control the focus of the confocal system. Finally, the last study contains a novel micro-scanner for 3D beam steering with better performance specifications, such as higher TOSA for less current consumption, increased resonance frequencies and smaller total size of the device as opposed to the previously designed micro-scanners. Also, fabricated micro-scanner is integrated in a confocal system and 2D image of a biological sample; convallaria rhizome, is obtained. Furthermore, a novel confocal microscopy configuration is proposed and it's validty is tested for 3D beam steering on a custom confocal setup in the last study.

4.1. Laser-Machined Stainless-Steel Micro-Scanner for 2D Confocal Microscopy

In this study, a 2D micro-scanner is fabricated out of stainless steel (grade:430) using laser-cutting technology. The presented scanner delivers a Lissajous scan pattern, with high-fill rate. In order to maximize both slow and fast scan line lengths, a DC magnetic field with an inclination of 45 degrees to the fast axis line is induced. The slow and the fast torsional resonant frequencies of the micro-scanner are observed at 663 Hz and 2211 Hz, respectively. An additional out-of-plane pumping mode is found at 1625 Hz. Fabricated device also integrated in a confocal setup and the imaging performance of the micro-scanner is tested on a USAF resolution target.

4.1.1. Optical Design

Firstly, optical targets of our confocal system are determined as follows: i) less than 3 μm resolution and ii) 200 μm $\times$ 200 μm FOV that is comparable to state-of-the-art benchtop laser scanning microscopes [74]. An objective lens having an NA of 0.4 and a clear aperture of 10 mm is chosen to achieve the desired lateral resolution. After $\times$3 magnification by the relay lens pair, the diameter of the input beam reaches 3.3 mm and fills less than half of the objective lens clear aperture. Hence, the effective NA reduces from 0.4 to 0.132. The spot full-width half-maximum (FWHM) diameter at the target can be calculated using Equation (2.1).

For the above mentioned conditions in our custom built setup and for a 0.658 μm wavelength input laser, we calculate the spot diameter to be 2.66 μm, satisfying our desired lateral resolution of less than 10 μm. Furthermore, in accordance with the desired FOV of 200 μm, one needs a TOSA (θ_o) of 3.82 degrees for the objective lens having a focal length of 9 mm using the Equation 2.2.

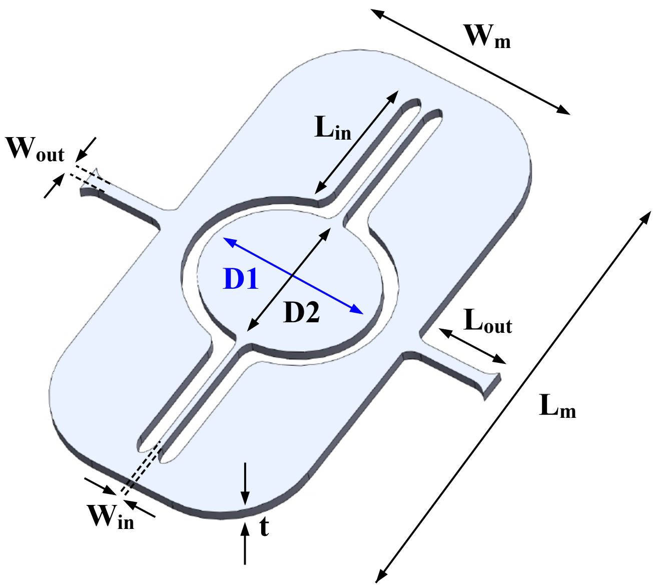

Figure 4.1. 3D view of the proposed device and its parametric dimensions [19].

Table 4.1. Dimensions of the stainless-steel micro-scanner (all in mm) [19].

Parameter	D_1	D_2	L_{in}	W_{in}	L_{out}	W_{out}	L_{m}	W_{m}	t
Value	6	5	5	0.25	3	0.4	17.1	8	0.4

4.1.2. Mechanical Design

The stainless-steel micro-scanner is developed to satisfy the FOV requirements that was set in the previous section. In Figure 4.1, CAD drawing of the device is given. The dimensions of the micro-scanner (Table 4.1) is adjusted to achieve the desired

TOSA that is determined in the previous section. Therefore, the gap between the inner flexure and gimbal is reduced to have more magnetic area on the gimbal for the interaction with the external B-field. Another aim of this design is to keep the slow and fast resonance frequencies of the scanner mutually prime and as high as possible in order to increase the fill factor of the Lissajous pattern.

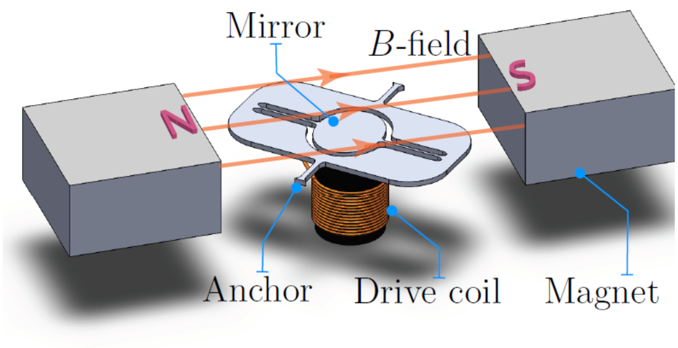

Figure 4.2. Magnetic actuation schematic of the designed stainless-steel micro-scanner with permanent magnets [19].

As shown in Figure 4.2, two permanent magnets are located close to the mirror with an inclination of 45 degrees to the fast axis scan to get maximum displacement for both slow and fast scan.

4.1.3. Experimental Results

Laser machining technology allows us to create fine shapes on a given substrate, which is stainless-steel for our case, easily with high accuracy within a small amount of time. After fabrication process, two permanent magnets are attached close to the mirror with an inclination of 45 degress to obtain maximum displacement for both slow and fast scan axes (Figure 4.2).

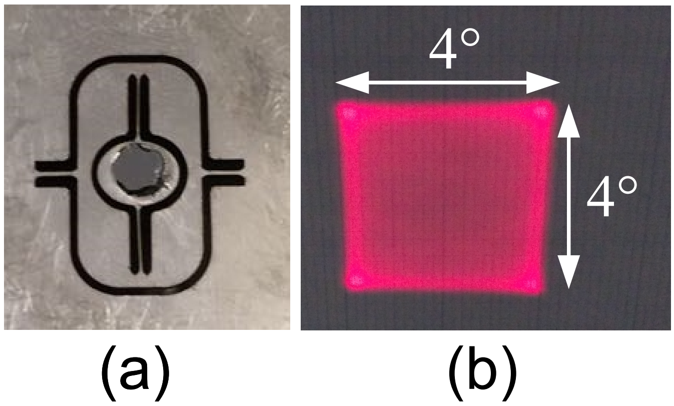

Figure 4.3. (a) Fabricated stainless-steel scanner. (b) Lissajous pattern with the corresponding total optical scan angles.

Figure 4.3b shows the Lissajous pattern at 663 and 2209 Hz for the LSCM system. TOSA of 4 degrees is observed for both slow and fast scan movements for a 180 mA driving current.

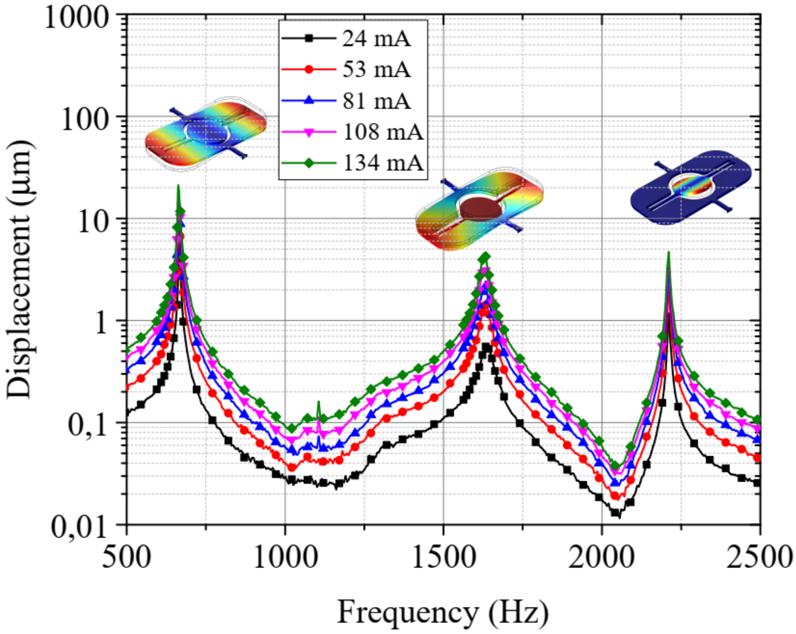

Figure 4.4. Frequency response of the stainless-steel micro-scanner for varying electrocoil current drives [19].

The deflection of the mirror as the frequency of the coil drive current is swept between 500-2500 Hz. Torsion around the slow and the fast axis is observed at 663 and 2211 Hz, respectively. An additional out-of-plane pumping mode occurs around 1625 Hz which could potentially be used for third dimension scan in future. Quality factors of slow and fast scan, in air operation, are measured as 110 and 275, respectively.

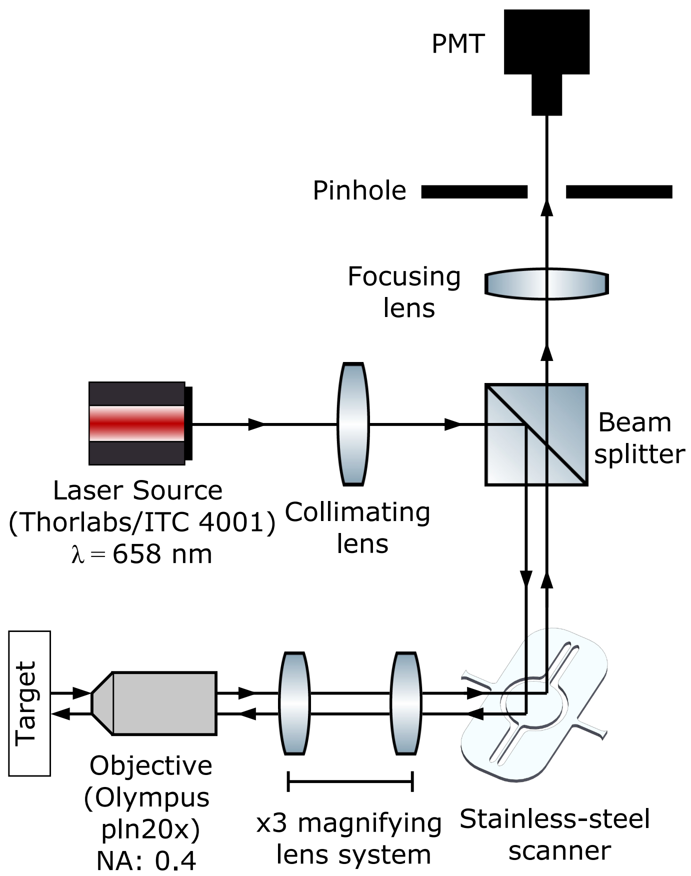

Figure 4.5. Schematic of the custom-built confocal microscope for 2D imaging.

Fabricated scanner is integrated in our custom-built confocal microscope (Figure 4.5 and Figure 4.6). The setup consists of a fiber-coupled laser (Thorlabs/ITC 4001) that is directed onto the scanning unit via a beam splitter. The scanner plane is relayed onto the objective lens (Olympus/PLN20x), which focuses and collects light to / from the target, via a lens pair that impose a x3 magnification on the 1.1 mm input beam diameter. The light is finally epi-collected onto a photomultiplier unit (Hamatsu/H10721-20), after getting focused onto a 100 μm pinhole to eliminate out-of-focus light from the target.

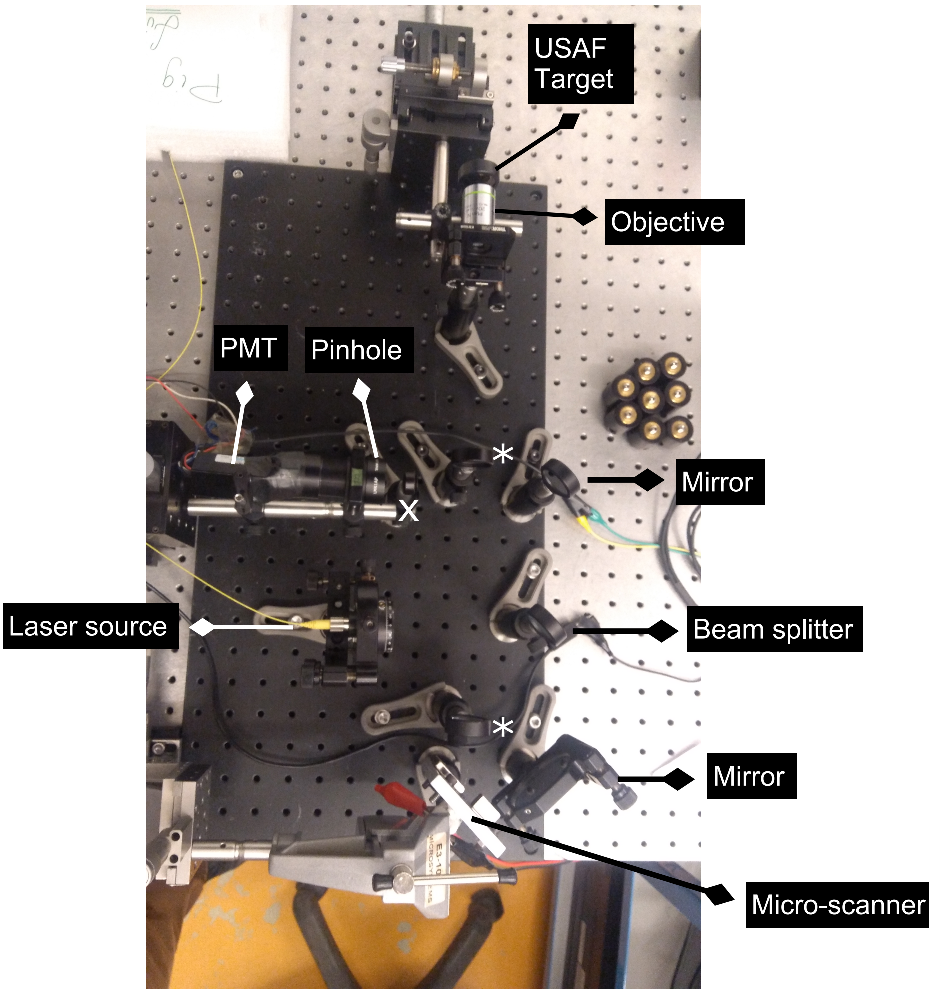

Figure 4.6. Custom benchtop confocal microscope setup. Relay lens pair is denoted by * and x denotes the focusing lens.

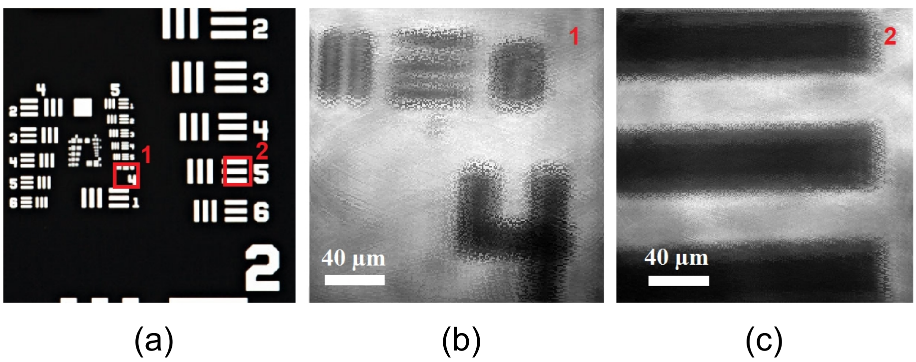

Figure 4.7. (a) Thorlabs 1951 USAF resolution target. (b) The image of the stripes of element 6 in group 5. (c) The image of the stripes of element 5 in group 3. FOV is 200 μm $\times$ 200 μm for both images [19].

In Figure 4.7, the USAF target, and the acquired images using custom-built confocal microscope setup, utilizing the steel-scanner presented in this study (test areas are shown in Figure 4.7a and 4.7b, having 8.77 μm and 39.37 μm line width, respectively). The FOV is observed as 200 μm $\times$ 200 μm with the achieved scan angles. The FWHM resolution based on Figure 4.7, is found as 3 μm.

4.2. Stainless-Steel Micro-Scanner for 3D Confocal Imaging Application

In this work, we are focusing on a 3D scanning micro-scanner fabricated out of stainless steel with high relative magnetic permeability (grade:430) which can work in different out-of-plane modes. Laser cutting technology is preferred as fabrication technique since it provides rapid production, high resolution and high accuracy. The proposed scanner generates Lissajous scan pattern satisfying high fill rate. The mode frequencies of the micro-scanner are found using finite element simulations and verified using Laser Doppler Vibrometer. After comparison of simulation and LDV results, a detailed study is provided for different out-of-plane modes in simulation environment using MATLAB.

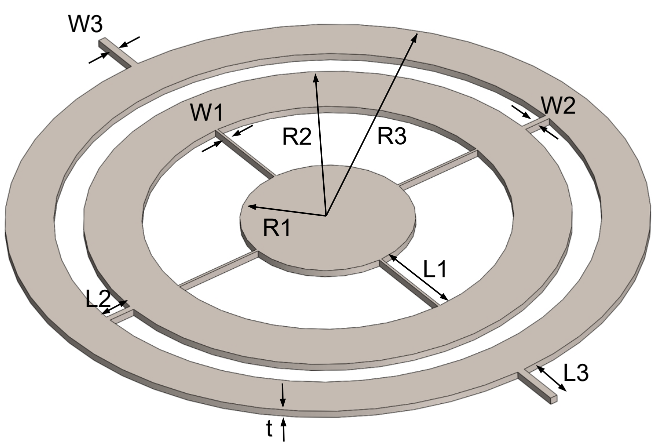

Figure 4.8. Designed multi-gimbaled scanner [20].

Table 4.2. Dimensions and material properties of the fabricated stainless-steel micro-scanner [20].

Parameter	**Symbol**	**Value**
Radius of the mirror	$R1$	9 mm
Radius of the first gimbal	$R2$	12.5 mm
Radius of the second gimbal	$R3$	16.5 mm
Width of the inner flexures	$W1$	0.14 mm
Width of the center flexures	$W2$	0.32 mm
Width of the outer flexures	$W3$	0.41 mm
Length of the inner flexures	$L1$	5 mm
Length of the center flexures	$L2$	1.5 mm
Length of the outer flexures	$L3$	2.8 mm
Thickness of the device	t	0.4 mm
Young's modulus	E	200 GPa
Density	ρ	7740 kg/m^3
Poisson's ratio	ν	0.28

4.2.1. Mechanical Design

Multi-gimbaled scanner is designed to work in different out-of-plane modes along with two orthogonal torsional modes for 3D scan (Figure 4.8). In order to demonstrate the operation of the proposed device with different out-of-plane modes, the frequency of the first out-of-plane mode is made as low as possible by playing with the width of the outer flexures. Moreover, the displacement of this mode is also considered and increased to scan the whole sample area. The areas of the gimbals adjusted in a fashion that slow and fast scan modes are separated from the first out-of-plane mode. While the outer flexures controls the slow scan movement of the device, central flexures determines the fast scan. Moreover, inside flexures creates an additional out-of-plane mode with higher frequency to be used to scan a specified location on the sample.

On the other hand, second out-of-plane mode is designed to have higher frequency to provides better fill ratio; hence, a more detailed scan. The dimensions and material properties of the proposed scanner are given in Table 4.2.

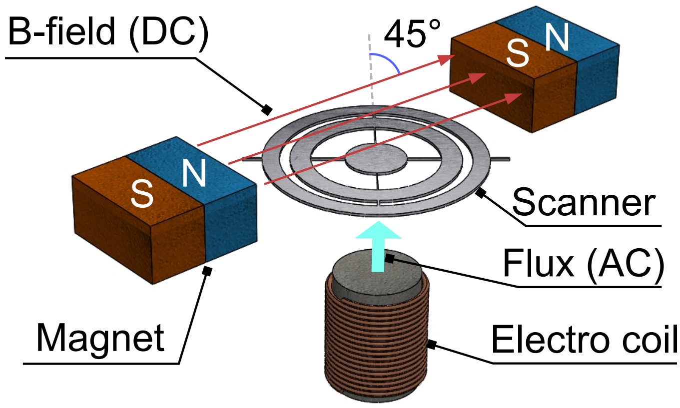

Figure 4.9. The magnetic actuation principle of the scanner in terms of the interaction of the DC B-field generated by the permanent magnets and the AC flux induced by the external coil [20].

In order to actuate the scanner, two permanent magnets are fixed close to the mirror with an inclination of 45 degrees to the fast axis scan to get maximum displacement for both slow and fast scan (Figure 4.9).

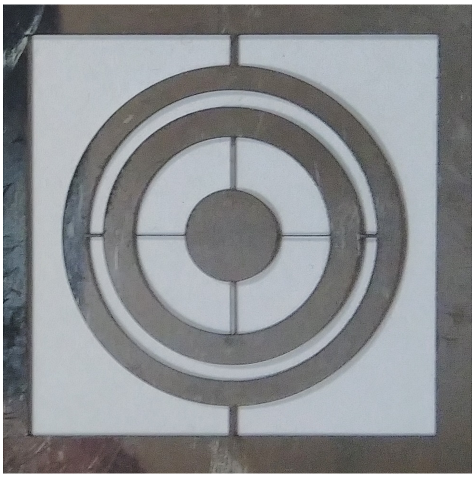

Figure 4.10. Fabricated multi-gimbaled stainless-steel scanner [20].

4.2.2. Experimental Results

Laser machining technology makes small patterns for a given material easier with high accuracy within a short amount of time. Fabrication process starts with the scanner design in a CAD software. The proposed design is imported to the software of our custom laser-cutter which directs the focused beam on to the stainless-steel substrate and this process gives the structure its final shape via burning the edges. In order to generate a DC magnetic field, two permanent magnets are fixed close to the mirror with an inclination of 45 degress to get maximum deflection for both slow and fast scan axes.

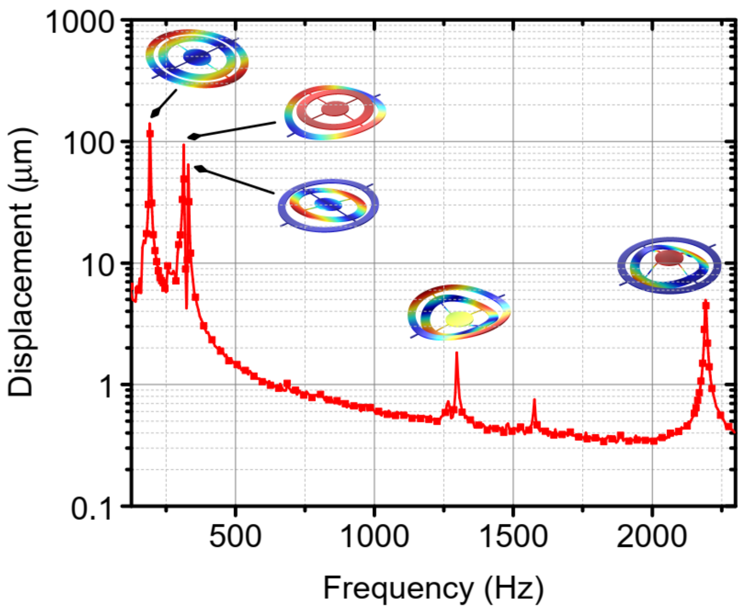

Figure 4.11. Frequency response of the device. Exact frequency values of the corresponding modes are provided in Table 4.3 [20].

As the frequency of the coil drive current is swept between 200-2600 Hz the deflection of the mirror is observed using a Laser-Doppler-Vibrometer (LDV) as given in Figure 4.11.

Resonance frequencies of the scanner are found by finite-element-method simulations and LDV results, show in good agreement and provided in Table 4.3.

Table 4.3. Comparison of mode frequencies (all in Hz) [20].

	FEM Results	LDV Results
Slow Scan	197	190
Out-of-plane 1	315	313
Fast Scan	337	329
Out-of-plane 2	1357	1296
Out-of-plane 3	2196	2192

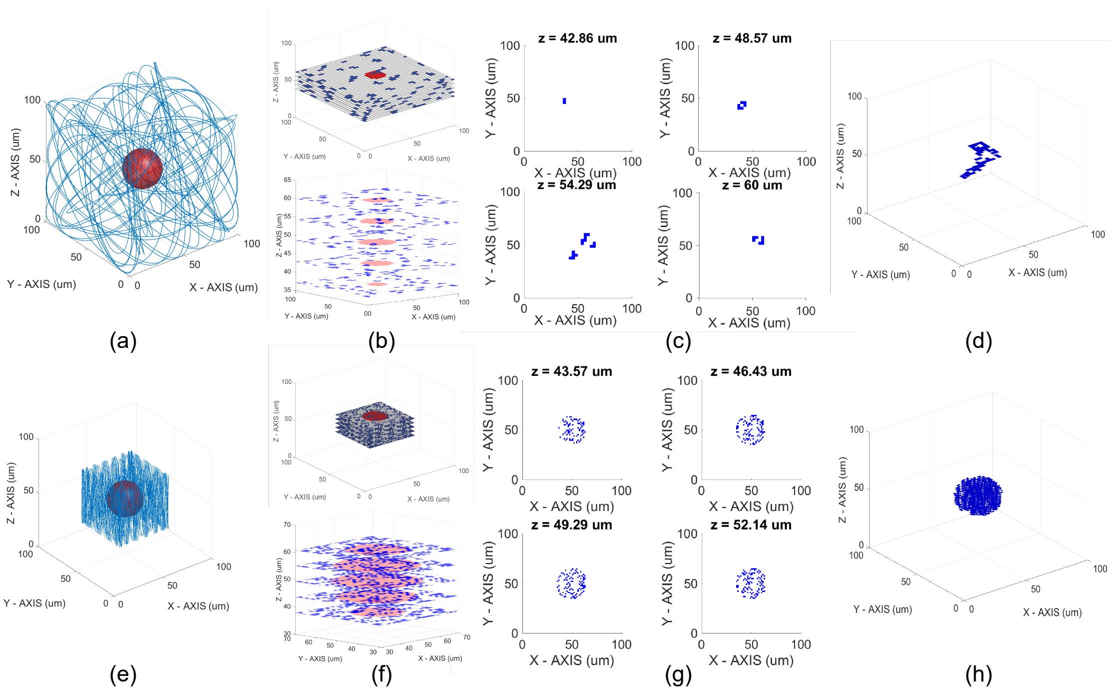

Figure 4.12. 3D Lissajous scan of a spherical solid with a radius of 15 μm within a volume of 100 μm $\times$ 100 μm $\times$ 100 μm for slow scan (a) and within a volume of 50 μm $\times$ 50 μm $\times$ 50 μm for fast scan (e). Demonstration of z axis slices for slow (b) and fast scan (f). Detected pixels of five different slices for slow (c) and fast scan (g). Reconstructed image for slow (d) and fast scan (h) [20].

4.2.3. 3D Scan Analysis

3D scan analysis is performed to observe three dimensional scan performance of the designed scanner. For that purpose, out-of-plane 1 (slow) and out-of-plane 3 (fast) modes, given in Table 4.3, are chosen to investigate fill rates of considered volumes for slow and fast out-of-plane modes, respectively. A spherical solid with a radius of 15 μm is considered as a target within a volume of 100 μm $\times$ 100 μm $\times$ 100 μm. Firstly, the whole volume is scanned with slow out-of-plane mode which has better displacement (Figure 4.11). Scanned volume is considered as a 3D matrix (36, 36, 36) which results in 36 slices along the z-direction. Scan duration is set to 0.15 s for demonstration purpose, and fill rate of the target is found as 8% (Figure 4.12a). The corresponding axial slices for five different axial positions are given in Figure 4.12b. There are three different color seen on the slices such as white, blue and red. They represents unscanned, scanned and sphere unit cells, respectively. Then, intersection of blue and red unit cells is gathered to construct scanned unit cells of the sphere. The corresponding slices of constructed sphere is shown in Figure 4.12c. Thus, rough image of the target is detected by the scanner that operates in slow out-of-plane mode as shown in Figure 4.12d. Since the rough image of the sample obtained, this time the sample is scanned within a volume of 50 μm $\times$ 50 μm $\times$ 50 μm with fast out-of-plane mode which has better fill ratio. As expected, fill rate of the target is increased to 25.7 % for the same scan duration as shown in Figure 4.12e. The corresponding axial slices for five different axial position are found as in Figure 4.12(f,g) and the reconstructed image is shown in Figure 4.12h. The axial positions are chosen as close as possible to the slow out-of-plane mode case. Furthermore, for a scan duration of 0.5 s, 24 % and 69% fill rates are found for slow and fast out-of-plane mode, respectively.

4.3. A Stainless-Steel Micro-Scanner for Rapid 3D Confocal Imaging

This work summarizes the design, fabrication, and characterization of a magnetically actuated stainless-steel based micro-scanner. The out-of-plane deflection of the proposed device is calculated by using a custom depth scan setup. The main advantage of laser cutting technology, which is utilized in manufacturing the proposed steel scanner, is its rapid fabrication capability at low cost, while still offering high frequency scan for imaging and/or ablation with high frame-rates. In the lateral plane, the scanner delivers 5 degrees of total optical scan angle for a current drive of 60 mA for both slow scan and fast scan axes at 998 Hz and 2795 Hz, respectively. Furthermore, the device provides an out-of-plane pumping mode at 1723 Hz that could be utilized for axial scanning to create focal shift at the target. Fabricated scanner is integrated into a confocal microscopy setup and tested with a resolution target and a Convallaria Rhizome sample, accomplishing a 240 μm $\times$ 240 μm field of view with 2.8 μm resolution. The device offers 218 μm depth of field (in tissue) and based on acquired resonance frequencies, we estimate rapid scanning of a three-dimensional block of tissue (240 μm $\times$ 240 μm $\times$ 218 μm size) with approximately 3 block per second with 50% fill rate and total coverage of 87% for 1 second scan. Finally, a custom setup is proposed for 3D imaging and validity of the 3D beam steering of the micro-scanner is tested.

4.3.1. Scanner Design

The proposed micro-scanner is designed to meet the following requirements. First of all, it is aimed to achieve mutually prime resonant frequencies of at least 1 kHz to have a proper fill ratio for rapid imaging [85]. Secondly, the total size of the device is made less than 2 cm $\times$ 2 cm to integrate it in a hand-held imager that is being targeted for future studies. Finally, it is required from the micro-scanner to accomplish a 240 μm $\times$ 240 μm FOV (for a confocal setup with an objective lens with 20$\times$ magnification and 0.4 NA) which is comparable to state-of-the-art benchtop laser scanning microscopes [86, 87].

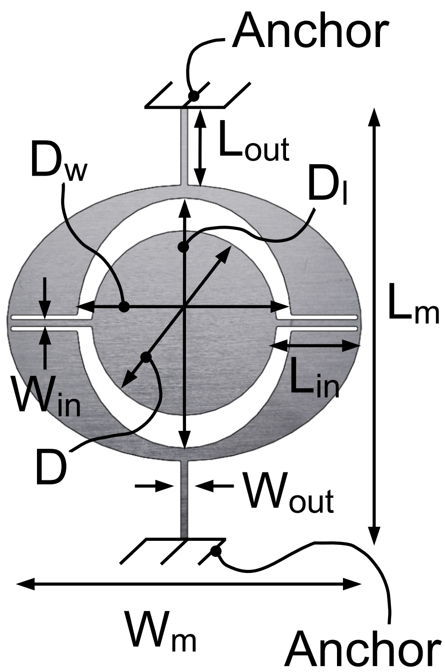

Figure 4.13. Top view of the micro-scanner parametrically showing its dimensions.

Based on our knowledge from the previously designed device [19], length of the inner (L_{in}) and outer flexures (L_{out}) are decreased to increase the resonant frequency of fast and slow scan, respectively. This manipulation is also reduces the total width (W_{m}) and length (L_{m}) of the device. The diameter of the mirror is not minimized since this change reduces the deflection of the fast scan and it is not increased due to the total size requirement. Although it has a decreasing effect on the resonance frequencies, narrowing the width of the inner (W_{in}) and outer flexures (W_{out}) increases the displacement of the fast and slow scan, respectively. The two-dimensional (2D) gimbaled scanner design, illustrated in Figure 4.13, offers two orthogonal torsional mechanical modes to scan laterally the specimen and an out-of-plane pumping mode for focus shift on the target. Table 4.4 provides the exact dimensions and material properties of the device.

Table 4.4. Dimensions and material properties [23] of the fabricated stainless-steel micro-scanner.

Parameter	**Symbol**	**Value**
Total scanner length	L_{m}	11.4 mm
Total scanner width	W_{m}	9.39 mm
Outer flexure length	L_{out}	2.05 mm
Outer flexure width	W_{out}	0.18 mm
Inner flexure length	L_{in}	2.15 mm
Inner flexure width	W_{in}	0.18 mm
Mirror diameter	D	4.89 mm
Elliptical Hole length	D_{l}	6.96 mm
Elliptical Hole width	D_{w}	5.02 mm
Thickness	t	400 μm
Young's modulus	E	200 GPa
Density	ρ	7740 kg/m^3
Poisson's ratio	ν	0.28

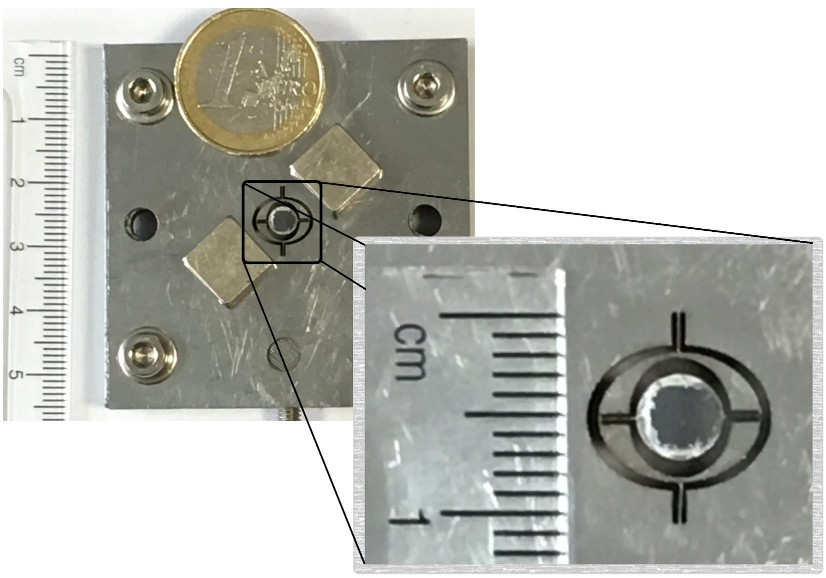

Figure 4.14. Fabricated stainless-steel micro-scanner using laser machining technology and attached permanent magnets.

Owing to its lowered cost (as opposed to Silicon micro-machining), high resolution and accuracy, and rapid production, the device is fabricated with laser-cutting technology using stainless steel with thickness (t) of 400 μm. 2D model designed in a CAD software is converted into G-code, which provides the instructions to a machine controller. The motion control system of our custom laser-cutter directs the focused beam on to the stainless-steel plate and this process gives the structure its final shape via burning the edges. The scanner is fabricated by our custom 400 Watt laser cutter which provides 30 μm beam diameter. This results in minimum 15 μm thickness faults in every drawn line if the beam is focused perfectly. A 50 μm thick aluminum-coated silicon piece was glued to the front side of the mirror to have a fine reflective surface. The micro-scanner is integrated with a 56 mm $\times$ 56 mm square mount that was fabricated using the same material just to facilitate the optomechanical setup of the LSCM (Figure 4.14).

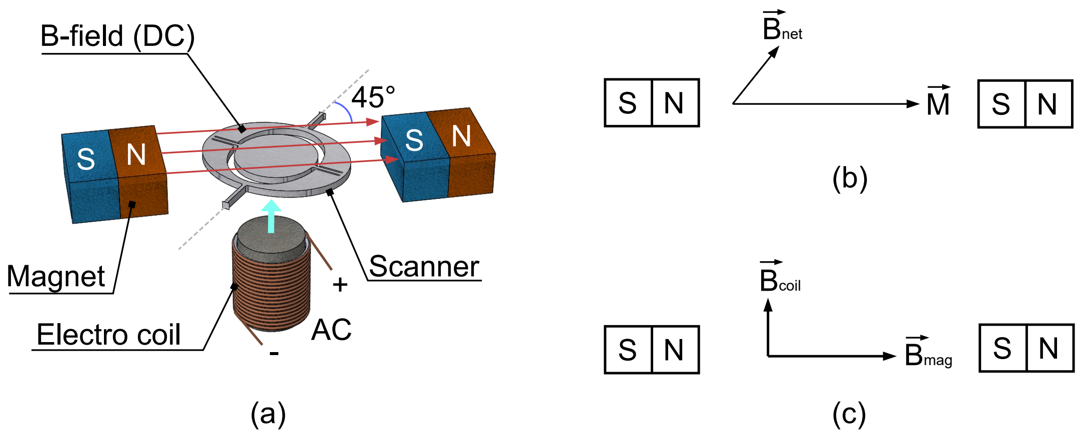

Figure 4.15. (a) The magnetic actuation technique of the scanner in terms of the interaction of the DC B-field generated by the permanent magnets and the AC flux induced by the external coil. (b), (c) The acting forces and torques on the mirror (top figure) and the gimbal (bottom figure)

4.3.2. Magnetic Actuation Principle

Magnetic actuation enables achieving high optical scan angles with low drive current. The base material (stainless-steel grade:430) that has high relative magnetic permeability providing larger deflections in a magnetic actuation mechanism. Two neodymium permanent magnets (1 cm × 1 cm × 0.6 cm each) are attached close to the micro-scanner with an inclination of 45 degrees to the fast axis scan to obtain optimized displacement for both slow and fast scan (Figure 4.15b). Micro-scanner and the electrocoil (model: LHL 10NB 104J, inductance: 100 mH) are fixed to the corresponding holders in a robust manner to prevent the energy coupling. The permanent magnets are fixed on the substrate (Figure 4.15a) and they create a magnetization vector in the lateral plane of the scanner device as illustrated in Figure 4.15b. The contribution of electrocoil to the magnetization is ignored since it has a little effect. When an AC signal is applied to the electro coil, at the positive cycle, there will be a B field ($\vec{\mathrm{B}}_{\mathrm{coil}}$) as indicated in Figure 4.15c. Moreover, there is also another B field ($\vec{\mathrm{B}}_{\mathrm{mag}}$) because of the permanent magnets. The combination of these two B fields is shown as $\vec{\mathrm{B}}_{\mathrm{net}}$ in Figure 4.15b. The resulting torque due to the interaction of magnetization with magnetic field intensity is described as follows:

$$\tau = \vec{m} \times \vec{B} \tag{4.1}$$

where $\vec{m}$ is magnetic moment and $\vec{B}$ is the magnetic field intensity and the relation between magnetic moment and magnetization is given as

$$\vec{M} = \frac{\vec{m}}{V} \tag{4.2}$$

where V is the volume of the substrate. Using Equation 4.2 in Equation 4.1 gives

$$\tau = V\vec{M} \times \vec{B} \tag{4.3}$$

the cross product of $\vec{M}$ and $\vec{B}_{net}$ creates a counter-clockwise torque (Figure 4.15b) and $\vec{B}$ can be described as

$$\vec{B} = \mu_0(\vec{H} + \vec{M}) \tag{4.4}$$

where $\mu_0 = 4\pi \times 10^{-7}$ T·m/A is the permeability of vacuum and $\vec{H}$ is the magnetic field intensity. Hence, Equation 4.3 becomes

$$\tau = V\vec{M} \times \mu_0(\vec{H} + \vec{M}) \tag{4.5}$$

after expanding this expression

$$\tau = V\mu_0(\vec{M} \times \vec{H} + \vec{M} \times \vec{M}) \tag{4.6}$$

where $\vec{M} \times \vec{M} = 0$. Therefore, one can reach the following equation.

$$\tau = V\mu_0(\vec{M} \times \vec{H}) \tag{4.7}$$

Here, $\vec{H} = \vec{H}_{coil}$ because H field due to the magnet ($\vec{H}_{mag}$) is in the direction of $\vec{M}$. Hence, $\vec{H}_{mag} \times \vec{M} = 0$. As a result, Equation 4.7 becomes

$$\tau = V\mu_0(\vec{M} \times \vec{H}_{coil}) \tag{4.8}$$

Since the magnetic field density due to $\vec{H}_{coil}$ is measured in the air, internal magnetization of the material can be ignored ($\vec{B}_{coil} = \mu_0\vec{H}_{coil}$) and it is assumed that $\vec{H}_{coil}$ is uniform on the micro-scanner having 90 degrees angle with the magnetization ($\vec{M}$). Hence, Equation 4.8 simplifies as follows

$$\tau = VMB_{coil} \tag{4.9}$$

The attached two permanent magnets saturate the magnetic flux density and it becomes $B_s = 1.51$ T for stainless-steel (grade:430) [88]. Since this material is ferrimagnetic, it has high relative magnetic permeability (μ_r); therefore, $\mu_r \gg \mu_0$ and saturation magnetization becomes $M_s \approx B_s = 1.51$ T.

The magnetic field intensity generated by the external electro coil and the corresponding magnetic flux density (B) values are measured in the air via a gaussmeter (AlphaLab / GM2) (Figure 4.16). Throughout the measurements, the orientation of the tip of the gaussmeter was in line with the B field lines.

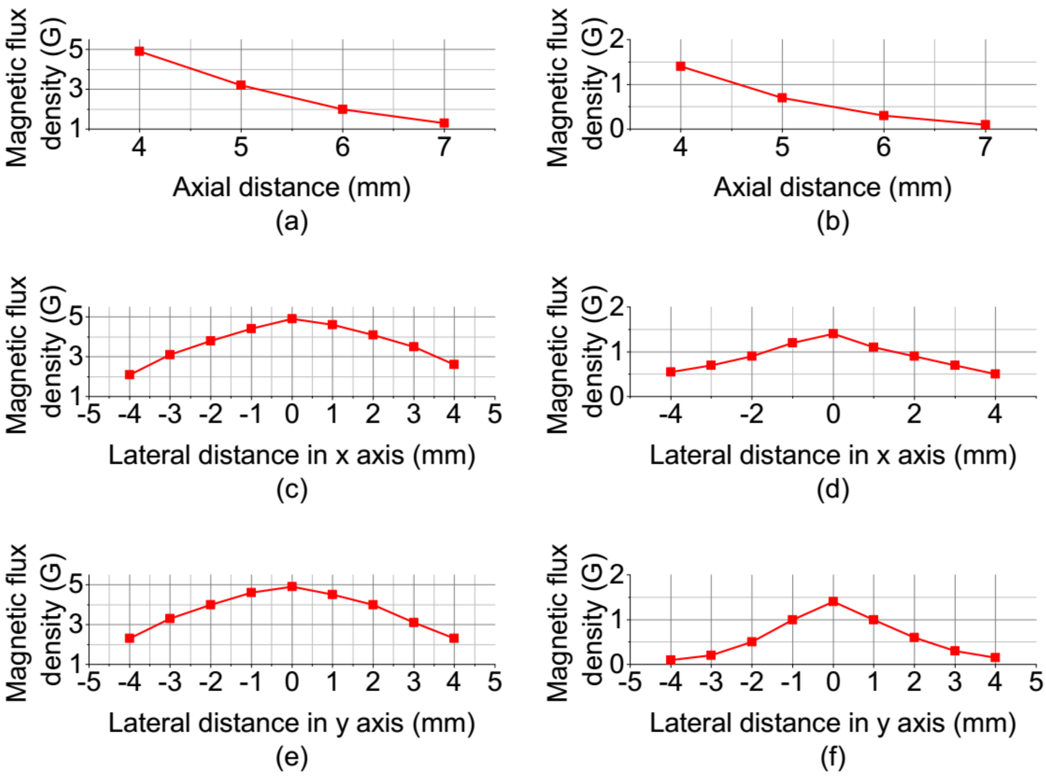

Figure 4.16. Magnetic flux densities at various distances from the center of the coil. (a), (c) and (e) are for different axial, lateral in x and lateral in y distances; respectively, for a driving current of 9.41 mA at 998 Hz. (b), (d) and (f) are for different axial, lateral in x and lateral in y distances; respectively, for a driving current of 3.75 mA at 2795 Hz.

The magnetic flux density generated by electro-coil is measured along all three axes. Moreover, magnetic flux density is observed separately for both torsional mode frequencies of 998 and 2795 Hz. When 10 volt peak to peak sinusoidal signal with frequency of 998 Hz is applied to the coil, the coil draws 9.41 mA current. The magnitude of the drawn current drops to 3.75 mA when the frequency of the signal is increased to 2795 Hz but the magnitude of the voltage kept the same. This is expected since the impedance of the inductor increases with increasing frequency. The magnetic flux density induced by the coil is decreasing from 4.9 Gauss to 1.3 Gauss when the distance is measured from the top of the coil at 998 Hz. Laterally, the highest magnetic flux density is acquired when the measurement is taken directly in front of the coil. As the probe of the gaussmeter is moved away from the center of the coil, the intensity decreases as expected. When the frequency of the signal is increased to 2795 Hz, the magnetic flux density decreases dramatically. For the axial distance case the maximum value is 1.4 Gauss whereas it drops down to 0.1 Gauss as the measurements taken away from the coil. The density decays similarly when the probe is moved laterally similar to 998 Hz case.

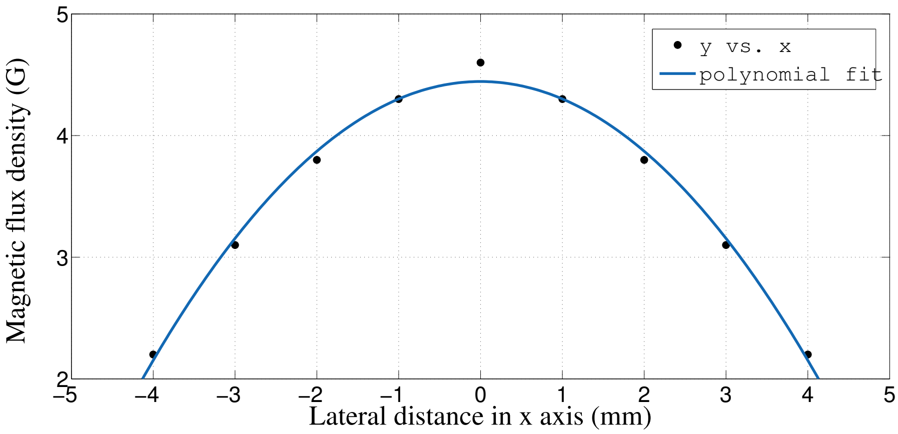

(c)

Figure 4.17. Polynomial curve fitted version of Figure 4.16c.

Note that, for each Figure we took only one measurement. The decay in Figure 4.16d and 4.16f should be polynomial as provided with Figure 4.17. The root-mean-square error for the polynomial fit is 8 %. In order to solve that discrepancy, the average of several measurements should be taken as data points.

As a result, approximate values of the acting torques on the mirror and the gimbal part can be found separately. For the sake of simple calculation, the geometry of the mirror part of the scanner is assumed as a cylinder having a diameter D with thickness of t and the geometry of the gimbal part is assumed as an elliptical cylinder with a width of W_m and length of $L_m - 2L_{out}$ and thickness of t (Figure 4.13). The distance between the center of the coil and the scanner was 4 mm throughout the image taking process and for that specific location of the coil, observed magnetic field densities are $B_{coil1} = 0.49$ mT and $B_{coil2} = 0.14$ mT (Figure 4.16). Using the values obtained for M_s, B_{coil1} and B_{coil2} and the dimensions of the micro-scanner device provided in Table 4.4 inside the Equation 4.9, acting torques around the slow and fast axis are carried out as $T_1 = 2.76$ μNm and $T_2 = 2.26$ μNm.

4.3.3. Analytical Calculations, FEM Results and Scanner Characterization

Aformentioned spring-mass-damper system can be used as a mathematical model to calculate the resonance frequencies of the micro-scanner. Once again, due to its small effect on the system output (Q-factor of the system is greater than 10), damping factor is neglected and since it has small mass compared to the base of the micro-scanner, Aluminum coated Silicon piece (thickness: 50 μm) also is ignored in the model.

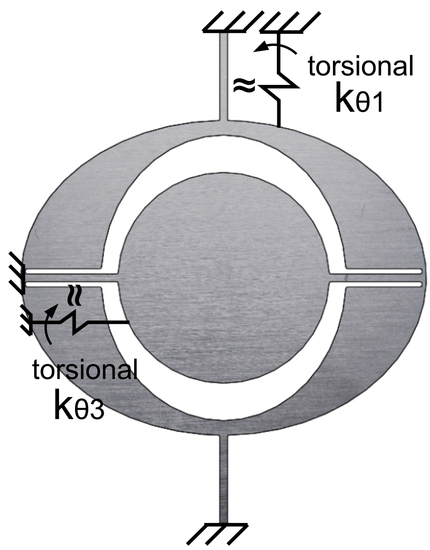

Figure 4.18. Designed micro-scanner with torsional spring constants.

Resonant frequency for the first (outer frame torsion) and the third (inner frame torsion) modes of the device can be approximated as a simple harmonic oscillators [54].

Resonance frequencies of the principal modes for the scanner are

$$\omega_1^2 = \frac{k_{\theta 1}}{J_{\theta 1}}, \quad \omega_2^2 = \frac{k_2}{M_2}, \quad \omega_3^3 = \frac{k_{\theta 3}}{J_{\theta 3}} \tag{4.10}$$

where ω_1 and ω_3 are the resonance frequencies of the modes where the outer frame and inner mirror part have a torsional movement about the springs, respectively. In addition, $k_{\theta 1}$ and $k_{\theta 3}$ models the torsional spring constant of the springs that suspend the outer frame and inner mirror to the anchor points, respectively (Figure 4.18). $J_{\theta 1}$ and $J_{\theta 3}$ are the mass moment of inertia of the rotating parts about the slow-scan and fast-scan axes, respectively. Furthermore, ω_2, k_2 and M_2 are the resonance frequency, spring constant and effective mass of the out-of-plane mode, respectively. The scanner structure consists of a mirror part, gimbal and flexures as shown in Figure 4.18. The effective mass moment of inertia for the proposed micro-scanner can be derived approximately in terms of the distances and provided density of the material [54] as follows:

$$\begin{aligned} J_{\theta 1} = & \frac{\rho\pi}{4}(L_{\mathrm{m}} - 2L_{\mathrm{out}})W_{\mathrm{m}}t\left[\frac{1}{4}\left(\frac{W_{\mathrm{m}}}{2}\right)^2 + \frac{1}{3}t^2\right] \\ & - \frac{\rho\pi}{4}D_{\mathrm{l}}D_{\mathrm{w}}t\left[\frac{1}{4}\left(\frac{D_{\mathrm{w}}}{2}\right)^2 + \frac{1}{3}t^2\right] \\ & + \frac{\rho\pi}{4}D^2t\left[\frac{1}{4}\left(\frac{D}{2}\right)^2 + \frac{1}{3}t^2\right] + \frac{1}{6}\rho W_{\mathrm{out}}L_{\mathrm{out}}t(W_{\mathrm{out}}^2 + t^2) \end{aligned} \tag{4.11}$$

As explained in Equation 2.6, spring constant of the rectangular cross-sectional outer beam made of stainless-steel (grade:430), which is assumed as an isotropic material, can be found in terms of the provided distances (Table 4.4) as follows:

$$k_{\theta 1} = \frac{W_{\mathrm{out}}^3\, t}{8L_{\mathrm{out}}} G\left[5.33 - 3.36\left(\frac{W_{\mathrm{out}}}{t}\right)\left(1 - \frac{1}{12}\left(\frac{W_{\mathrm{out}}}{t}\right)^4\right)\right] \tag{4.12}$$

where G is shear modulus of the material. ω_2, given in Equation 4.10, is the resonance frequency of the out of plane deflection of the scanning mirror, where k_2 is the spring constant for out-of-plane movement and M_2 is the effective mass of the device. It is assumed that the micro-scanner is a clamped-clamped beam and the dimension of its length is L_m and the applied force is a point force in the middle of the device. Hence the derived equations are as follows [54]:

$$k_2 = \frac{24\,E\,I}{\left(\frac{L_\mathrm{m}}{2}\right)^3} \tag{4.13}$$

$$M_2 = \frac{\rho\,\pi\,t}{4}\left[(L_\mathrm{m} - 2L_\mathrm{out})W_\mathrm{m} - D_\mathrm{l}D_\mathrm{w} + D^2\right] + 2\rho W_\mathrm{out}L_\mathrm{out}t \tag{4.14}$$

Last mode of the device that concerns scanning operation is the torsion of the mirror producing the fast scan. The resonant frequency (ω_3) for this mode is set by the torsional spring constant of the inner suspensions ($k_{\theta 3}$) and the effective mass moment inertia ($J_{\theta 3}$).

$$k_{\theta 3} = \frac{W_\mathrm{in}^3\,t}{8L_\mathrm{in}}\,G\left[5.33 - 3.36\left(\frac{W_\mathrm{in}}{t}\right)\left(1 - \frac{1}{12}\left(\frac{W_\mathrm{in}}{t}\right)^4\right)\right] \tag{4.15}$$

$$J_{\theta 3} = \rho\pi\frac{D}{2}^2 t\left[\frac{1}{4}\left(\frac{D}{2}\right)^2 + \frac{1}{3}t^2\right] + \frac{1}{6}\rho W_\mathrm{in}L_\mathrm{in}t\left(W_\mathrm{in}^2 + t^2\right) \tag{4.16}$$

As a result, using aforementioned material properties and the geometry given in Table 4.4, natural frequencies for the first, second and the third mode are calculated as 1088, 2105 and 3359 Hz where these modes are outer frame torsion (slow scan), out of plane pumping (depth scan) and mirror torsion (fast scan), respectively.

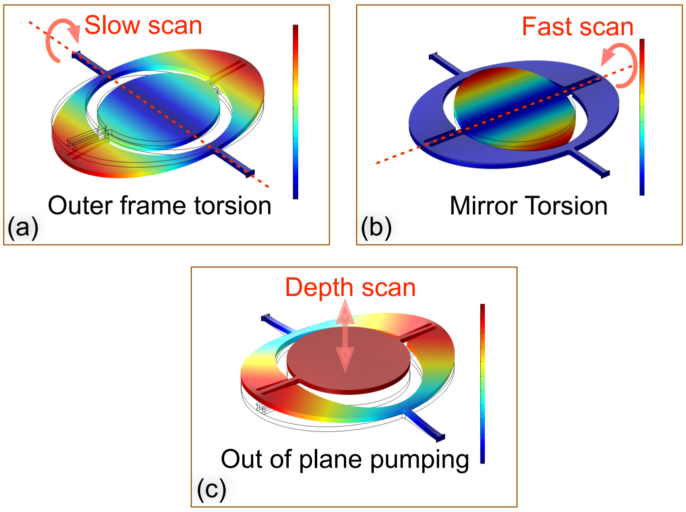

Figure 4.19. Mode shapes of the device calculated with FEM software. a) Slow scan at 1037 Hz. b) Fast scan at 2933 Hz. c) Out-of-plane at 1808 Hz.

Mode frequencies of the scanner are also investigated using a Finite Element Method (FEM) software. The micro-scanner device is made out of stainless-steel (grade:430) which has the manufacturer specified material properties given in Table 4.4. These parameters are specified in the simulations. The first and the third modes are targeted for lateral scan, while the intermediate mode offers axial scanning. The first mode of the micro-scanner is found to be torsional and it provides a rotation about the outer flexure at 1037 Hz. The second mode is out-of-plane bending movement at 1808 Hz which offers depth scan. The second torsional movement, around the inner flexure is observed at 2933 Hz and it orthogonally assists the first mode in lateral scanning. Mode shapes of the micro-scanner obtained from FEM simulations can be seen in Figure 4.19.

The deflection of the micro-scanner in different scanning modes are measured using a Laser Doppler Vibrometer (LDV) unit (Polytec OFV-534 sensor with OFV-5000 controller) as the scanning frequency is swept between 500-3000 Hz for a drive current of 60 mA. As shown in Figure 4.20, the first measured mode is related to the torsional movement of the whole structure around the slow scan axis at 999 Hz. Quality factor of this mode is extracted as 170. The second mode in the spectrum is the out of plane pumping mode of the mirror which occurs at 1723 Hz. Quality factor

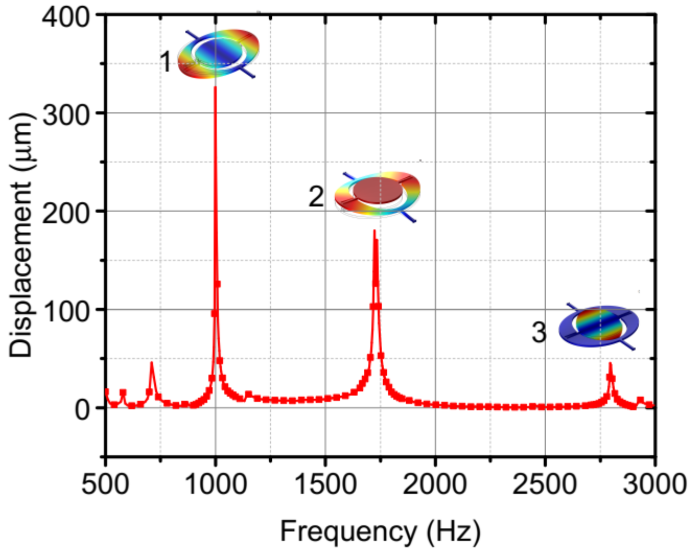

Figure 4.20. Frequency response of the stainless-steel micro-scanner. 1) Torsional-movement about slow-scan axis, 2) Out-of-plane pumping mode for axial movement and 3) Torsional-movement about fast-scan axis

of this resonance is 220. The torsion about the fast axis is observed at 2795 Hz having a quality factor of 280. All the measurements are performed in ambient air. For a drive current of 60 mA, the micro-scanner delivers 5 degrees of total optical scan angle for both slow and fast axes at 999 Hz and 2795 Hz, respectively.

Table 4.5. Calculated, simulated and experimentally characterized resonance frequencies for the scanner (all in Hz).

	f_1	f_2	f_3
Analytical Calculation	1088	2105	3359
Finite Element Simulation	1037	1808	2933
Experimental Characterization	999	1724	2795

Calculated, simulated and experimental resonant frequencies are summarized in Table 4.5. Here, f_1, f_2, f_3 denotes slow scan, out-of-plane and fast scan movements, respectively. Since the mathematical model used for the analytical calculation is for slender beams with sufficiently low frequencies and the attached Aluminum coated Silicon piece is ignored in the computations, analytical results for the out-of-plane mode and torsional mode for fast scan are found higher than expected. Comparison of the quality factors of principal peaks of the present device with its polymer based counterpart reveals an order of magnitude improvement in the quality factor. Such quality factor values allows scanner to be driven with a significantly lower power consumption.

4.3.4. System Characterization for Two-Dimensional Scan

The proposed scanner, whose vibration modes and axial actuation capability is characterized, is placed in our custom-built confocal microscopy setup (Figure 3.4). In this setup, a fiber-coupled laser is directed onto the scanning unit via a beam splitter. The scanner plane is relayed onto the objective lens (20X magnification with an NA of 0.4), which focuses and collects light to / from the target, via a lens pair that impose a $\times 3$ magnification for a 1.2 mm input beam diameter. The first lens, which is called scan lens, has effective focal length (F_1) of 50 mm and the second relay lens, namely tube lens, has effective focal length (F_2) of 150 mm. Using the focal lengths of the previously mentioned relay lens pair and the distance represented by d4 in Table 3.4, the distance from tube lens to the objective is found by using the Equation 2.3 which provides an infinity-corrected configuration. The focused light is reflected from the sample, and follows the same path till it impinges upon the beamsplitter, finally reaching a 100 μm pinhole through a focusing lens (with a focal length of 30 mm). Pinhole eliminates out-of-focus light from the target, and the laser light is finally epi-collected onto a photomultiplier tube.

The performance of manufactured stainless steel micro-mirror is further tested inside the custom-built confocal microscope setup on USAF target. Figure 4.21 (no post-processing involved) illustrates portion of the resolution target, acquired with the manufactured scanner embedded within our home-built confocal microscope. Elements 3 and 4 of group 5 on the 1951 USAF target are easily resolved as expected. Furthermore, the edges of each strip could be used to determine both edge response, and the beam size (the impulse response, i.e. the derivative of the edge response), as we did

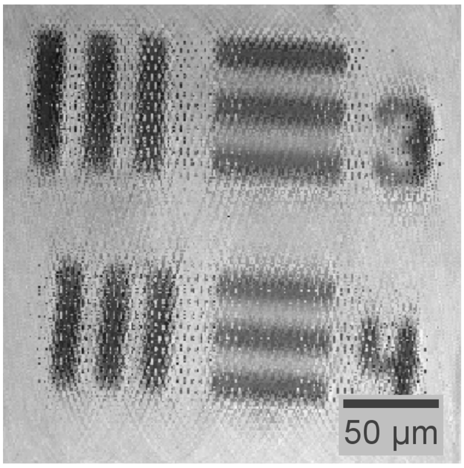

Figure 4.21. USAF image of the stripes of element 3 and 4 of group 5 captured with our custom-built confocal microscope setup.

in our previous study leading to a 2.8 μm resolution. Note that FWHM resolution depends on the NA of the objective lens, as well as the magnification offered by the relay lens pair, rather than the scanner itself (when dynamic deformation of the scanner is neglected). Yet, the scanner has a critical role on determining the number of resolvable spots and frame-rate. Moreover, the resolution could be further enhanced by increasing the input beam size or increasing the magnification ratio of relay lens pair, or using a higher NA objective. However, these alterations will diminish the field-of-view (FOV).

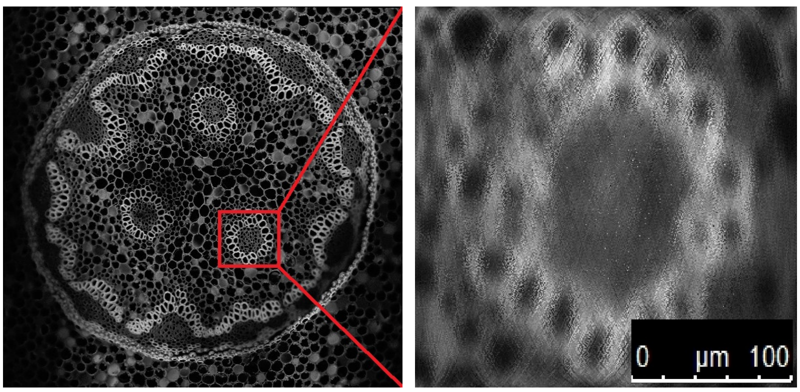

Figure 4.22. Images of Convallaria Rhizome. (a) The whole image of the sample captured with commercial Confocal Microscope. (b) Image of the red square taken with laser-machined stainless-steel scanner integrated in our custom microscope

Figure 4.22a shows the images of the Convallaria Rhizome captured with Leica TCS SP5 commercial confocal microscope device. The whole image, having 2 mm × 2 mm FOV, is captured with image stitching approach. Figure 4.22b illustrates the image acquired with our scanner integrated in confocal microscope. Despite taken at a lower NA (0.4 for commercial setup vs. 0.13 effective NA in our setup) our image delineates the well known honeycomb pattern in a Convallaria Rhizome. No filtering or post imaging processes are implemented for this capture.

4.3.5. 3D Imaging Analysis

4.3.5.1. Axial Scan Analysis. We utilize the setup, to observe the extent of axial actuation of the manufactured scanner, illustrated in Figure 4.23.

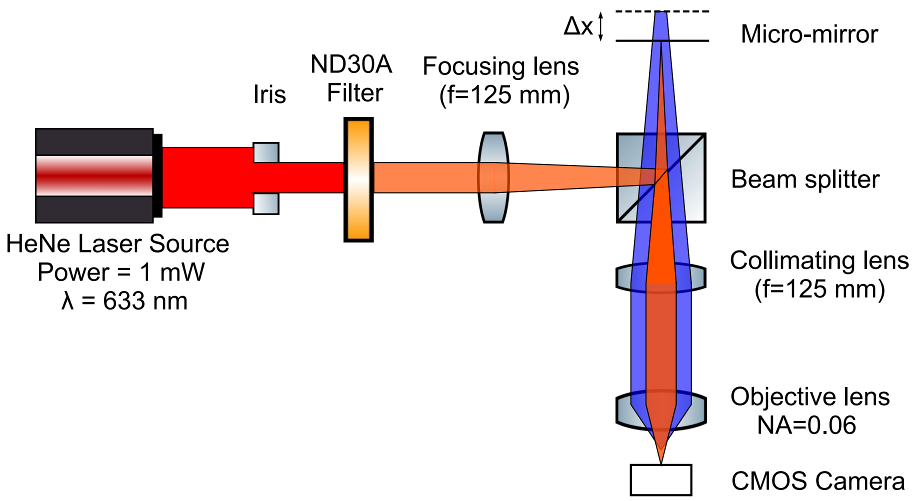

Figure 4.23. Out of plane movement detection setup.

This setup, which is a modified version of the custom confocal microscopy setup (to be mentioned later in the manuscript) consists of laser source, beam splitter, micro-scanner, focusing lens, collimating lens, an objective lens and a complementary metal oxide semiconductor (CMOS) camera. The size of the collimated beam coming out of the laser source is adjusted using an iris at the expense of reducing the laser power. Then ND30A filter which has 0.1% transmission, decreases the laser power further in order to avoid saturation of CMOS camera due to excessive laser power. A focusing lens of f = 125 mm is used to focus the beam onto the micro-scanner. At original configuration, the focused spot size on the scanner is imaged onto the CMOS camera (via a combination of f= 125 mm collimating lens and an objective lens - Correct Tokyo M-PlanAPO-2-5x - pair.), thus the scanner and the camera are at conjugate planes. As the micro-scanner is actuated in the out of plane mode, the spot size on the CMOS camera enlarges, from which one can deduce the amount of axial bending in the intermediate out-of-plane pumping mode. The data gathered by CMOS camera is processed by a PC.

In order to determine the displacement amount of the micro-scanner at its out-of-plane pumping mode (Figure 4.20), the scanner is actuated through driving the electrocoil with the corresponding AC signal with a driving current of 14 mA and the variation of the spot size is observed. In order to observe the change in the spot size at such high frequency, the scan period is strobed with a similar camera exposure duration (only slightly different to observe the scan in a slow-motion fashion). Movement of the scanner is recorded as a tiff file in this step and sorted out. In order to find the corresponding displacement amounts of the micro-scanner, when it is externally actuated at its out-of-plane pumping mode, the device is also manually driven with a translation stage. Using these results of the manually driven case, the displacement values of the externally actuated case are estimated. After the comparison of the beam sizes, a peak displacement of $\pm\,300\,\mu$m is observed. The beam size alteration data for externally actuated case is given with their fitted curve in Figure 4.24.

During the operation, the micro scanner is moved along z-axis. Intensity profile of the laser is recorded by using CMOS camera for each step of displacement between $z = \pm\ 300\ \mu$m. Then, value of beam waists are extracted for each different z-axis value as follows: Beam radius values are calculated considering intensity profile only on the vertical y-axis of the camera. Obtained intensity data for different z-axis values are curve fitted to Gaussian distribution. For each z value, different Gaussian curve fits are obtained and alterations in beam size are observed. As defined in Equation 2.27, the standard deviation for each z value, FWHM; therefore, spot size values, $w(z)$, can be obtained by using Equation 2.26. As mentioned above, the spot sizes are individually

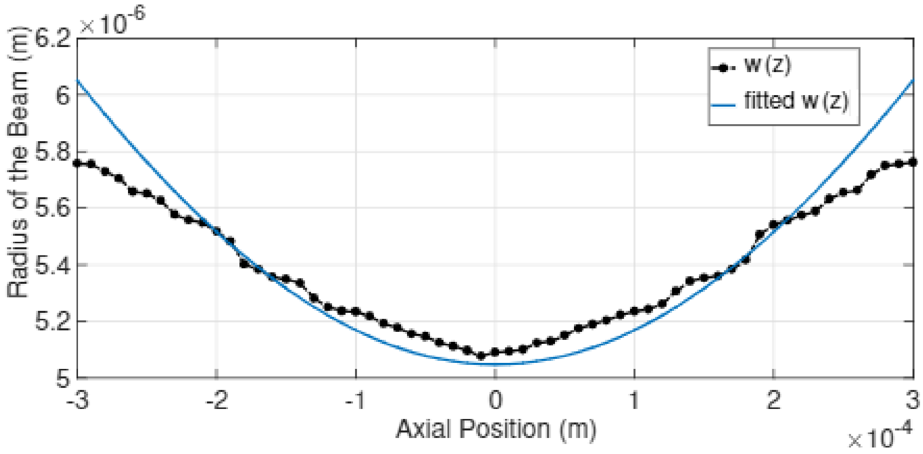

Figure 4.24. Out of plane deflection measurement data. Radius of the beam $w(z)$: (electromagnetic actuated scanner) and fitted curve of $w(z)$.

measured for all axial positions as z values are changing. After obtaining $w(z)$ values for different axial positions, derived beam radius dataset fit into a curve that is modelled with Equation 2.30. The results are demonstrated in Figure 4.24.

The radius of the beam on the detector plane at the initial position of the scanner for both cases are observed to be 5.1 μm (recorded in terms of full-width-half-maximum: FWHM). The actuation of the scanner for the manually driven case, enlarges the spot size to 5.9 μm and 6.1 μm for -300 μm and 300 μm, respectively. The difference in the spot size is due to the optical misalignments. Whereas, for the externally driven case, the spot size increases to 5.75 μm for both $\pm$ 300 μm displacement.

4.3.5.2. Proposed 3D Scanning Confocal Microscope Setup. The out-of-plane mode of the proposed scanner can be used in the proposed confocal setup to obtain axial slices of a given sample as shown in Figure 4.25. The reflected light from the sample should visit the micro-scanner before it reaches the pinhole, otherwise scanned light will be eliminated by the pinhole. Therefore, the beam splitter denoted as (3) is necessary to collect the intensity values reflected from the target. The second beam splitter denoted with (4) is also needed for a right angle of incidence on the micro-scanner.

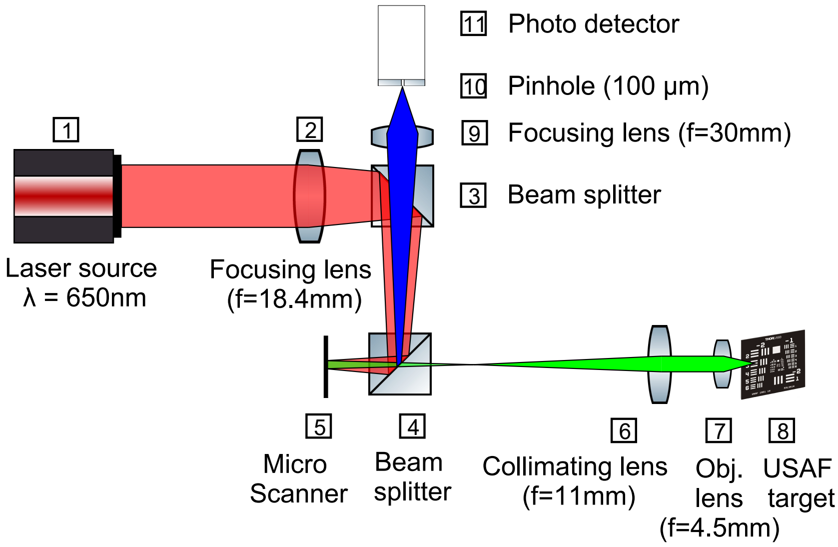

Figure 4.25. Confocal microscope setup for 3D imaging.

The lens (denoted by (2)) between laser source and the beam splitter (3) focuses the input beam between the beam splitter (4) and the lens numbered as (6). When the mirror rests, collimated light reaches the objective lens (7) before the sample. When the out-of-plane mode of the device is active, the micro-scanner moves back and forth; hence, changes the size of the converging light approaches to the lens (7) and creates an axial scan on the sample.

<u>4.3.5.3. Ray Tracing Simulations and Analytical Calculations.</u> Proposed confocal microscope system is constructed to have a depth-of-focus around 10 μm and to be able to produce at least 16 slices in axial scan. The setup is modeled for axial scan analysis in a ray tracing software to determine the depth-of-field and depth-of-focus of the proposed system (Figure 4.25). The ratio of the former to the latter provides how many different slices can be obtained from different depths within the sample. In this mode, collimated light is focused with the lens (2). While the collimated light is converging, it passes through beam splitter (3) and (4) before hitting the micro-scanner (5). The beam reaching the micro-scanner is not focused so that a 2D scan of a specimen is also realizable using this setup. After that, it passes through beam splitter (4) one more

Table 4.6. Properties of the optical components in proposed 3D scanning setup.

Enumerated pair	**Distance (mm)**
2-3	1
3-4	1
4-5	1.65
4-6	9.92
6-7	4
7-8	0.745
Enumerated lens	**Focal length (mm)**
2	18.4
6	11
7	4.51

time before reaching the lens pair denoted as (6) and (7) (Figure 4.25). These square beam splitters, having a side of 5-mm, are modeled as a BK7 glass in the software. It is assumed that the micro-scanner is located in the middle of the last two glasses. The thicknesses of the optical elements and the distances between these components are provided in Table 4.3.

The focal length of the first lens (2) is chosen as small as possible because increasing the focal length of the this lens reduces the diameter of the entering beam to the last lens (7). Decrease of the input beam to the last lens also reduces the effective NA of this lens; therefore, shrinks the depth-of-field of the proposed setup. Note that, the focal point of the first lens is also large enough that beam splitters and the micro-mirror can be placed before the diameter of the input beam reaches the desired amount, which, in turn, provides the effective NA (0.32) of the objective lens. Since a focused beam on the micro-scanner can not create a 2D scan, a converging beam (having a diameter of approximately 1.3 mm) hits the mirror and the beam is focused between the beam splitter (4) and lens (6). The distances between the first lens (2) - beam splitter (3) and between the two beam splitters are kept as small as 2 mm to squeeze these components before the focus of the input beam. The distance from the beam splitter (4) to the lens (6) is adjusted to ensure a collimated beam is reaching the final lens (7) when the micro-scanner rests.

The irradiance distribution of an optical system can be observed using the point spread function (PSF). As shown in Figure 4.25, the system is construted in the software and the image plane is forced to locate at the focus of the beam after lens (7). Then, the image plane is moved back and forth from the focus until the maximum irradiance reduces to half of its initial value. The total movement of this image plane is found as 10 μm which is actually the depth-of-focus. In order to determine the depth-of-field, both the distances before and after the micro-scanner are 250 μm increased and decreased. Although the micro-scanner is capable of moving more than $\pm$ 250 μm (Figure 4.23), this amount of motion is chosen in order not to compel the scanner into its limits by staying in well curve fitted range and therefore to provide a smooth scan. After each movement, the image plane is forced to move to the focus of the beam and the total difference between the new focal points found as 163 μm which is the depth-of-field. As a result of ray tracing simulations, this configuration provides $\frac{163}{10} \approx 16$ slides for axial scan.

The depth-of-focus of the system can also be calculated analytically. A Helium-Neon laser source is used in our axial scan setup and in our simulations which generates a laser beam that has intensity profile of TEM_{00} mode. The intensity profile of this specific laser light is modeled with a Gaussian function. Using the values given in Table 4.3, a collimated beam (having a radius of w_1) occurs between the lens (6) and lens (7). The FWHM radius of the spot size at the focal point of the last lens (7) can be found as $w_0 = 1.6$ μm by using following expression: [89]

$$w_0 = \frac{\lambda d}{w_1 \pi} \tag{4.17}$$

where d is the distance between the lens and focus of the light (Table 4.3). Using this FWHM radius of the beam (w_0) in a Gaussian function ,$\frac{1}{e^2}$ radius of the spot size can be found and this value can be denoted as w_2 and used in the following Equation [13].

$$z_0 = \frac{\pi {w_2}^2}{\lambda} \tag{4.18}$$

where z_0 is called Rayleigh length and two times of this parameter is depth-of-focus which is found as $z_{total} = 10.6\ \mu$m and very close to the one obtained from ray tracing simulations.

Secondly, the proposed system is modeled for 2D scan analysis. After the ray tracing simulations, for a mechanical tilt of $\pm$ 1.15 degrees, which provides 4.6 degrees of TOSA and it is less than the maximum TOSA of the fabricated micro-scanner, a FOV of 240 μm is obtained. Additionally, the lateral resolution of the proposed setup is found as 1.02 μm.

4.3.5.4. 3D Lissajous Scan Simulations. In the last part, the 3D scan analysis of the stainless-steel micro-scanner is performed in MATLAB, for the proposed 3D imaging system, based on the simulation results obtained in the previous subsection. Figure 4.26 illustrates the simulations of the fill rate of each slice, i.e the ratio of scanned area vs. unvisited areas denoted with yellow and red pixels, respectively. The images which are captioned from (a) to (p) demonstrate different slices in the 3D image and their fill pattern. While drawing the figure, pixels are counted as scanned if they are visited at least once. Hence, figure is plotted in a binary fashion.

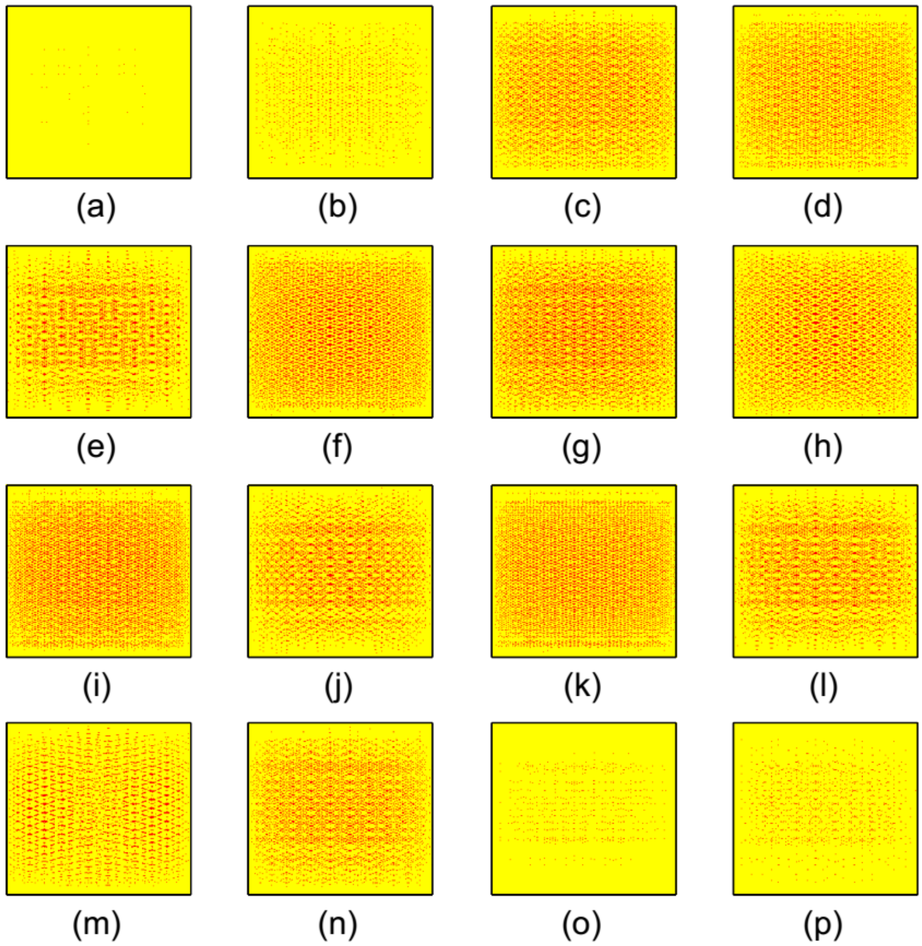

Figure 4.26. Coverage of 16 axial slices for a scan duration of 1 second. (yellow pixels: scanned area, red pixels: unscanned area)

The FOV for stainless-steel micro-scanner during this simulation is 240 μm $\times$ 240 μm which is in correspondence to previous ray tracing simulation results. The depth of field is taken as 163 μm in air, in accordance with the extent of axial movement in the ray tracing simulations. When a typical tissue refractive index of 1.34 at the utilized wavelength is considered, the axial scan in tissue is amplified to 218 μm. The scan duration is specified as 1 second and bandwidth of the amplifier that samples the incoming data stream is taken as 10 MHz, in accordance with the off-the-shelf available amplifiers. The effective NA of the scanning setup is found in ray tracing simulations as 0.32 while the wavelength of the input light is 0.65 μm. Therefore, FWHM values for lateral and axial scanning were calculated according to formulas below [51].

$$\mathrm{FWHM}_{xy} = \frac{2\sqrt{\ln 2} \times 0.32\lambda}{NA_{\text{eff}}} \tag{4.19}$$

$$\mathrm{FWHM}_{z} = \frac{2\sqrt{\ln 2} \times 0.532\lambda}{n - \sqrt{n^2 - NA_{\text{eff}}^2}} \tag{4.20}$$

FWHM_{xy} and FWHM_{z} calculated as 1.1 μm and 14.8 μm, respectively [51]. These values are in compatible with the lateral and axial resolution values found in ray tracing simulations if the refractive index of the medium is considered which is ignored during those simulations.

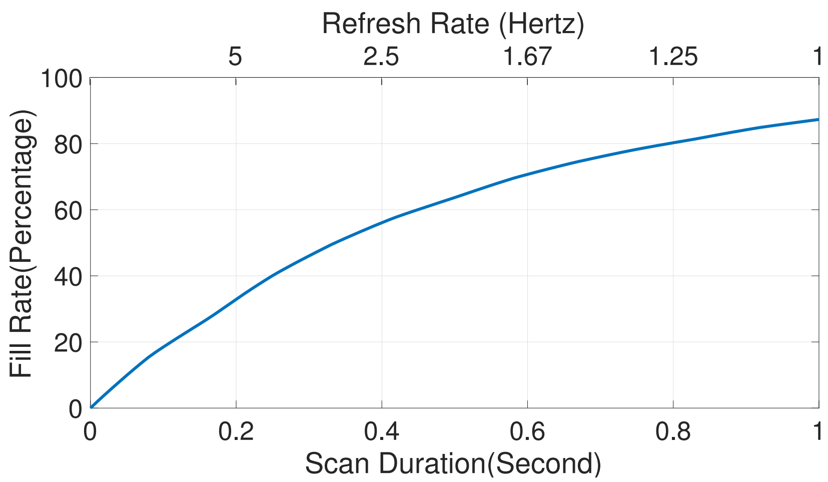

Figure 4.27. Fill rate as a function of scan duration and refresh rate.

The relationship between fill rate of the 3D Lissajous pattern and scan duration is observed in Figure 4.27, and is calculated based on formulations given elsewhere [64]. Although the acquired frequencies, and targeted FOV allows for a maximum fill rate of 87% at 1 fps, a significant portion of it can still be addressed at higher fps values. Lissajous scan allows for a fast preview of the majority of the fairly large 3D tissue block at $\approx$ 3 fps where the scanner provides 50% fill-rate.

3D beam steering of the proposed method is realized by an experimental setup which is very similar to the one in Figure 4.23. In order to emphasize the axial motion

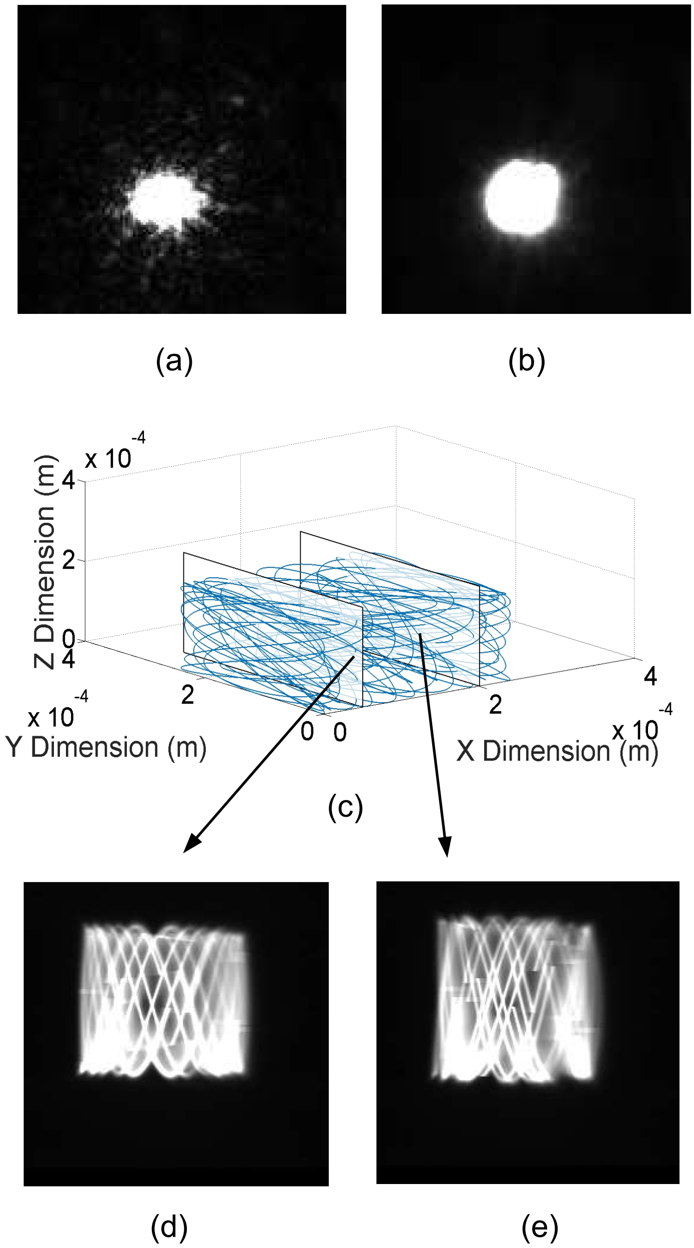

Figure 4.28. Demonstration of 3D Lissajous Scan with experimental data.

on the target, an off-the-shelf focusing lens with a focal length of 25.4 mm and a collimating lens with a focal length of 75 mm are used and the remaining components of the setup are kept the same.

In Figure 4.28a, the beam on the CMOS camera is observed when the mirror at rest. While the mirror is actuated for its out-of-plane motion, the beam moves away from focus and it gets larger as seen in Figure 4.28b. Since the circular hole shape of the iris is not flawless and due to surface flatness of the scanner, the shape of the beam is not perfectly circular and there are some noisy white pixels around the beam. During the out of plane motion of the mirror, these white pixels becomes blurred as the plane of focus constantly changes. The increased beam size is comparable to the micro-scanner out-of-plane movement of about 450 μm. The observed value could be improved upon applying a higher current to the coil, or with an optimized coil that would result in higher force for a 70 mA current. Similarly, a 2D Lissajous scan is observed on the camera when the micro-scanner is actuated for its orthogonal torsional modes which results coverage of 800 μm $\times$ 800 μm area (Figure 4.28d). Note that out-of-plane mode is not driven in this case. The brightness of the image is seems almost the same at each point; however, the left and right bottom corners are sharper than other parts of the pattern due to the optical misalignments. For the second case, the torsional modes of the mirror device are actuated with the same amount of power for 2D scan. 2D Lissajous pattern on the CMOS camera becomes blurred when the beam moves away from the focus of the objective lens (Figure 4.28e). Also note that the size of the Lissajous pattern gets larger in this case which is consistent with the difference observed between Figure 4.28a and Figure 4.28b. Figure 4.28c shows the corresponding observed planes as the micro-scanner makes 3D Lissajous scan. Keep in mind that the planes are drawn arbitrarily and only for demonstration purposes. The estimated axial scan of the micro-scanner is around 600 μm which is enough to look at the 3D image of a onion skin sample or acute rat brain tissue sample [10].

Table 4.7. Performance specifications comparison of our system with other 3D beam steering micro-scanners.

	[90]	**[91]**	**This work**
TOSA f_1,f_2	0.4°, 0.4°	20°, 14.5°	5°, 5°
Applied voltage f_1,f_2	1V, 1V	N/A	10V, 10V
Applied power out-of-plane	N/A, N/A	75mW	140mW
Applied power f_1,f_2	N/A, N/A	2.3mW	600mW
Vertical displacement	70 nm for 1V	200 μm	600 μm
Torsional frequencies	f_1,f_2 = 7.40, 31.9 kHz	f_1,f_2 = 238 ,244 Hz	f_1,f_2 = 998 ,2795 Hz
Out-of-plane frequency	f_3 = 18.3 kHz	DC Actuation	f_3 = 1723 Hz
Total device size (μm)	1500×1500×30	2000×2000×5 (only mirror)	9390x11400x400
Base material	Silicon	Silicon	Stainless-steel
Applied application	None	None	Confocal Microscope

In Table 4.7, our fabricated 3D scanner is compared with other 3D beam steering micro-scanners. Here f_1 and f_2 denote torsional resonant frequencies. The specifications of our device are obtained from characterization results provided in Section 4.3.1 and Section 4.3.2.

The micro-scanner produced by Nagasawa et al. [90] has high resonant frequencies and total size of the device is suitable for endoscopic applications; however, TOSA of the device for a given voltage is a little bit less than our micro-scanner. Moreover, the vertical displacement of that device is around 0.7 μm for 10V which is quite less than our device and applied current for any mode of the device is not given in this study. Whereas, Afsharipour et al. [91] also fabricated a micro-scanner for 3D beam steering and this device has quite impressive TOSA for very low power and can be considered as highly efficient. But, the torsional resonant frequencies of the device are quite low and it will be problematic for a Lissajous scan in terms of fill rate or it will be a slow device if one wants to get high fill rates with this device. Furthermore, total size of the device is not provided and it seems it is a little bit large if one wants to use it in a hand-held endoscopic imaging system.

Overall, the presented device is not only comparable in size to the 3D scanning devices presented in literature, but it was also manufactured with laser-machining technology allowing very low cost and rapid fabrication.

5. CONCLUSION

As a result of this study, in order to realize micro-scanners, two different fabrication methods; 3D printing and laser-machining technology is applied on polymer (Veroclear) and stainless-steel (grade:430), respectively. These techniques are low cost and have pretty simple fabrication steps. Fabricated devices are used in confocal microscopy applications.

In the former study, for the first time, a 3D printed scanner was demonstrated on a laser scanning microscope. Thanks to non-planar fabrication capability of the 3D printing routine, the flexures of the device could be built having a circular cross-section that significantly reduces the accumulated stress during its dynamic operation. The mechanical design allowed for both out-of plane and torsional modes, combination of which resulted in a Lissajous scan. The measured total optical scan angles, together with the experiments conducted on a custom built confocal microscopy setup reveal that a FOV of 105 μm $\times$ 105 μm and lateral resolution of 2.82 μm can be addressed. The resonance frequencies of the device were modeled analytically, closely matching those acquired experimentally with an LDV unit.

In the latter part, three different micro-scanners are fabricated via laser-machining technology.

A laser machined stainless steel micro scanner is designed for 2D confocal microscopy. The 2D scanning pattern is developed using Lissajous scan. Fabricated device integrated in custom confocal setup and its optical performance tested on a USAF resolution target. A FOV of 200 μm $\times$ 200 μm is obtained.

Another laser-machined stainless steel micro scanner is designed to work in different out-of-plane modes for confocal microscopy. The proposed device accomplish a 3D Lissajous scan in a volume of 100 μm $\times$ 100 μm $\times$ 100 μm to detect the sample by using its lowest out of-plane mode along with the torsional modes then it scans a reduced volume of 50 μm $\times$ 50 μm $\times$ 50 μm with its highest frequency out-of-plane to get a sharper image.

Finally, a stainless steel micro-scanner is designed for magnetic actuation and fabricated via laser-machining technology. The device is successfully used in a confocal microscope setup. Resonant frequencies of the proposed device is observed in a FEM software and experimentally measured with an LDV unit. Use of stainless steel as the structural material allows moderately high $Q-$factors which is the key performance parameter to satisfy fundamental specifications such as scan angle. Combination of the orthogonal torsion modes of slow and fast scan used to get a 2D Lissajous pattern. Developed micro-scanner is used in a custom-built confocal microscope setup and accomplished a 240 μm $\times$ 240 μm FOV and 2.8 μm FWHM resolution. The image of Convallaria Rhizome is acquired by the custom confocal microscope. In simulations, the out-of-plane pumping mode of the micro-scanner is showed to have 218 μm depth scan in tissue. The presented scanner also enables 3D scan of a tissue block of 240 μm $\times$ 240 μm $\times$ 218 μm within fraction of a second (with 3 fps), while addressing the half of the volume and provides 87% fill rate for 1 second scan. The punchline of this work is to design and characterization of a low cost micro-scanner for rapid 3D compact scanning microscopy technologies.

Remaining future work is to utilize the current confocal microscope setup in imaging experiments with three dimensional slicing capability.

REFERENCES

1. “Museo Galileo, Compound microscope, Galilean”, https://catalogue.museogalileo.it/object/CompoundMicroscopeGalilean.html, accessed in February 2019.

2. Minsky, M., “Microscopy apparatus”, Google Patents, Dec. 19 1961, uS Patent 3,013,467.

3. Petran, M. and M. Hadravsky, “Method and arrangement for improving the resolving power and contrast”, Google Patents, Jun. 30 1970, uS Patent 3,517,980.

4. Davidovits, P. and M. D. Egger, “Scanning laser microscope”, *Nature*, Vol. 223, No. 5208, p. 831, 1969.

5. White, J., W. Amos and M. Fordham, “An evaluation of confocal versus conventional imaging of biological structures by fluorescence light microscopy.”, *The Journal of cell biology*, Vol. 105, No. 1, pp. 41–48, 1987.

6. “Thorlabs, Small Beam Diameter Scanning Galvo Mirror Systems”, https://www.thorlabs.com/newgrouppage9.cfm?objectgroup_id=3770, accessed in May 2019.

7. “Leica, Supercontinuum Confocal Microscope”, https://www.leica-microsystems.com/products/confocal-microscopes/p/leica-tcs-sp5-x/, accessed in May 2019.

8. Liu, L. and H. Xie, “3-D confocal laser scanning microscopy based on a full-MEMS scanning system”, *IEEE Photonics Technology Letters*, Vol. 25, No. 15, pp. 1478–1480, 2013.

9. Ahn, H., J. Park, J.-A. Kim and J. Jin, “Optical fiber-based confocal and inter-

ferometric system for measuring the depth and diameter of through silicon vias", *Journal of Lightwave Technology*, Vol. 34, No. 23, pp. 5462–5466, 2016.

10. Liu, L., E. Wang, X. Zhang, W. Liang, X. Li and H. Xie, "MEMS-based 3D confocal scanning microendoscope using MEMS scanners for both lateral and axial scan", *Sensors and Actuators A: Physical*, Vol. 215, pp. 89–95, 2014.

11. Bargiel, S., Ł. Nieradko, M. Józwik, C. Gorecki and J. A. Dziuban, "New generation of fully integrated optical microscopes on-chip: application to confocal microscope", *Proceedings of SPIE, the International Society for Optical Engineering*, pp. 618602–1, Society of Photo-Optical Instrumentation Engineers, 2006.

12. Li, H., X. Duan, Z. Qiu, Q. Zhou, K. Kurabayashi, K. R. Oldham and T. D. Wang, "Integrated monolithic 3D MEMS scanner for switchable real time vertical/horizontal cross-sectional imaging", *Optics express*, Vol. 24, No. 3, pp. 2145–2155, 2016.

13. Teich, M. C. and B. E. Saleh, *Fundamentals of photonics*, Vol. 22, Wiley New York, 1991.

14. Xu, Z., S. Kolev and E. Todorov, "Design, optimization, calibration, and a case study of a 3d-printed, low-cost fingertip sensor for robotic manipulation", *Robotics and Automation (ICRA), 2014 IEEE International Conference on*, pp. 2749–2756, IEEE, 2014.

15. Kesner, S. B. and R. D. Howe, "Design principles for rapid prototyping forces sensors using 3-D printing", *Mechatronics, IEEE/ASME Transactions On*, Vol. 16, No. 5, pp. 866–870, 2011.

16. Wu, S.-Y., C. Yang, W. Hsu and L. Lin, "3D-printed microelectronics for integrated circuitry and passive wireless sensors", *Microsystems & Nanoengineering*, Vol. 1, 2015.

17. Oyman, H., Y. Gokdel, O. Ferhanoglu and A. Yalcinkaya, "A 3D Polymer Based Printed Two-Dimensional Laser Scanner", *Journal of Physics: Conference Series*, Vol. 757, p. 012024, IOP Publishing, 2016.

18. Oyman, H. A., Y. D. Gokdel, O. Ferhanoglu and A. D. Yalcinkaya, "Performance of a three-dimensional-printed microscanner in a laser scanning microscopy application", *Optical Engineering*, Vol. 57, No. 4, p. 041405, 2018.

19. Oyman, H., M. Icel, B. Efe, Y. Gokdel, O. Ferhanoglu and A. Yalcinkaya, "A Laser-Machined Stainless-Steel Micro-Scanner for Confocal Microscopy", *Multidisciplinary Digital Publishing Institute Proceedings*, Vol. 1, p. 564, 2017.

20. Oyman, H. A., B. C. Efe, M. A. Icel, Y. D. Gokdel, O. Ferhanoglu and A. D. Yalcinkaya, "Towards 3D Confocal Imaging with Laser-Machined Micro-Scanner", *Multidisciplinary Digital Publishing Institute Proceedings*, Vol. 2, p. 1067, 2018.

21. "Thorlabs, Reflective Objectives, Infinity Corrected", `https://www.thorlabs.com/newgrouppage9.cfm?objectgroup_id=6933`, accessed in May 2019.

22. "Mauna Kea Technologies, Cell Visio unit", `http://www.maunakeatech.com/en/cellvizio`, accessed in November 2017.

23. "Stainless steel 430, Data Sheet", `www.aksteel.com/pdf/markets_products/stainless/ferritic/430_data_sheet.pdf`, accessed in Nov 2018.

24. Mu, X., W. Sun, H. Feng, A. Yu, K. W. S. Chen, C. Y. Fu and M. Olivo, "MEMS micromirror integrated endoscopic probe for optical coherence tomography bioimaging", *Sensors and Actuators A: Physical*, Vol. 168, No. 1, pp. 202–212, 2011.

25. Sun, J., S. Guo, L. Wu, L. Liu, S.-W. Choe, B. S. Sorg and H. Xie, "3D in vivo optical coherence tomography based on a low-voltage, large-scan-range 2D MEMS

mirror", *Optics express*, Vol. 18, No. 12, pp. 12065–12075, 2010.

26. Kim, K. H., J. A. Burns, J. J. Bernstein, G. N. Maguluri, B. H. Park and J. F. de Boer, "In vivo 3D human vocal fold imaging with polarization sensitive optical coherence tomography and a MEMS scanning catheter", *Optics express*, Vol. 18, No. 14, pp. 14644–14653, 2010.

27. Zhong, Q., D. Inniss, K. Kjoller and V. Elings, "Fractured polymer/silica fiber surface studied by tapping mode atomic force microscopy", *Surface Science Letters*, Vol. 290, No. 1-2, pp. L688–L692, 1993.

28. Helmchen, F., W. Denk and J. N. Kerr, "Miniaturization of two-photon microscopy for imaging in freely moving animals", *Cold Spring Harbor Protocols*, Vol. 2013, No. 10, pp. pdb–top078147, 2013.

29. Zhang, C. C., W. B. Foster, R. D. Downey, C. L. Arrasmith and D. L. Dickensheets, "Dynamic performance of MEMS deformable mirrors for use in an active/adaptive two-photon microscope", *SPIE BiOS*, pp. 97170G–97170G, International Society for Optics and Photonics, 2016.

30. Carlsson, K., P.-E. Danielsson, R. Lenz, A. Liljeborg, L. Majlöf and N. Åslund, "Three-dimensional microscopy using a confocal laser scanning microscope", *Optics letters*, Vol. 10, No. 2, pp. 53–55, 1985.

31. Xiao, G., T. R. Corle and G. Kino, "Real-time confocal scanning optical microscope", *Applied physics letters*, Vol. 53, No. 8, pp. 716–718, 1988.

32. Maitland, K. C., H. J. Shin, H. Ra, D. Lee, O. Solgaard and R. Richards-Kortum, "Single fiber confocal microscope with a two-axis gimbaled MEMS scanner for cellular imaging", *Optics express*, Vol. 14, No. 19, pp. 8604–8612, 2006.

33. Minsky, M., "Memoir on inventing the confocal scanning microscope", *Scanning*, Vol. 10, No. 4, pp. 128–138, 1988.

34. Egger, M. D. and M. Petran, “New reflected-light microscope for viewing unstained brain and ganglion cells”, *Science*, Vol. 157, No. 3786, pp. 305–307, 1967.

35. Amos, W. and J. White, “How the confocal laser scanning microscope entered biological research”, *Biology of the Cell*, Vol. 95, No. 6, pp. 335–342, 2003.

36. Ra, H., W. Piyawattanametha, E. Gonzalez-Gonzalez, M. J. Mandella, G. S. Kino, O. Solgaard, D. Leake, R. L. Kaspar, A. Oro and C. H. Contag, “In vivo imaging of human and mouse skin with a handheld dual-axis confocal fluorescence microscope”, *Journal of Investigative Dermatology*, Vol. 131, No. 5, pp. 1061–1066, 2011.

37. Ra, H., W. Piyawattanametha, Y. Taguchi, D. Lee, M. J. Mandella and O. Solgaard, “Two-dimensional MEMS scanner for dual-axes confocal microscopy”, *Journal of Microelectromechanical systems*, Vol. 16, No. 4, p. 969, 2007.

38. Shin, H.-J., M. C. Pierce, D. Lee, H. Ra, O. Solgaard and R. Richards-Kortum, “Fiber-optic confocal microscope using a MEMS scanner and miniature objective lens”, *Optics express*, Vol. 15, No. 15, pp. 9113–9122, 2007.

39. Polglase, A. L., W. J. McLaren, S. A. Skinner, R. Kiesslich, M. F. Neurath and P. M. Delaney, “A fluorescence confocal endomicroscope for in vivo microscopy of the upper-and the lower-GI tract”, *Gastrointestinal endoscopy*, Vol. 62, No. 5, pp. 686–695, 2005.

40. Knittel, J., L. Schnieder, G. Buess, B. Messerschmidt and T. Possner, “Endoscope-compatible confocal microscope using a gradient index-lens system”, *Optics Communications*, Vol. 188, No. 5, pp. 267–273, 2001.

41. Xie, Z., S. Jiao, H. F. Zhang and C. A. Puliafito, “Laser-scanning optical-resolution photoacoustic microscopy”, *Optics letters*, Vol. 34, No. 12, pp. 1771–1773, 2009.

42. Wang, J., M. Yang, L. Yang, Y. Zhang, J. Yuan, Q. Liu, X. Hou and L. Fu, “A confocal endoscope for cellular imaging”, *Engineering*, Vol. 1, No. 3, pp. 351–360,

2015.

43. Mu, X., G. Zhou, H. Yu, Y. Du, H. Feng, J. M. L. Tsai and F. S. Chau, "Compact MEMS-driven pyramidal polygon reflector for circumferential scanned endoscopic imaging probe", *Optics express*, Vol. 20, No. 6, pp. 6325–6339, 2012.

44. Aljasem, K., L. Froehly, A. Seifert and H. Zappe, "Scanning and tunable micro-optics for endoscopic optical coherence tomography", *Microelectromechanical Systems, Journal of*, Vol. 20, No. 6, pp. 1462–1472, 2011.

45. Pan, Y., H. Xie and G. K. Fedder, "Endoscopic optical coherence tomography based on a microelectromechanical mirror", *Optics letters*, Vol. 26, No. 24, pp. 1966–1968, 2001.

46. Jung, W., J. Zhang, L. Wang, P. Wilder-Smith, Z. Chen, D. T. McCormick and N. C. Tien, "Three-dimensional optical coherence tomography employing a 2-axis microelectromechanical scanning mirror", *Selected Topics in Quantum Electronics, IEEE Journal of*, Vol. 11, No. 4, pp. 806–810, 2005.

47. Zara, J. M. and P. E. Patterson, "Polyimide amplified piezoelectric scanning mirror for spectral domain optical coherence tomography", *Applied physics letters*, Vol. 89, No. 26, p. 263901, 2006.

48. Mitsui, T., Y. Takahashi and Y. Watanabe, "A 2-axis optical scanner driven non-resonantly by electromagnetic force for OCT imaging", *Journal of Micromechanics and Microengineering*, Vol. 16, No. 11, p. 2482, 2006.

49. Morrison, J., M. Imboden, T. D. Little and D. Bishop, "Electrothermally actuated tip-tilt-piston micromirror with integrated varifocal capability", *Optics express*, Vol. 23, No. 7, pp. 9555–9566, 2015.

50. Hokari, R. and K. Hane, "A varifocal convex micromirror driven by a bending moment", *IEEE Journal of Selected Topics in Quantum Electronics*, Vol. 15, No. 5,

pp. 1310–1316, 2009.

51. Zipfel, W. R., R. M. Williams and W. W. Webb, "Nonlinear magic: multiphoton microscopy in the biosciences", *Nature biotechnology*, Vol. 21, No. 11, pp. 1369–1377, 2003.

52. Hoy, C. L., O. Ferhanoğlu, M. Yildirim, W. Piyawattanametha, H. Ra, O. Solgaard and A. Ben-Yakar, "Optical design and imaging performance testing of a 9.6-mm diameter femtosecond laser microsurgery probe", *Optics express*, Vol. 19, No. 11, pp. 10536–10552, 2011.

53. Frostig, R., *In vivo optical imaging of brain function*, CRC press, 2002.

54. Urey, H., C. Kan and W. O. Davis, "Vibration mode frequency formulae for micromechanical scanners", *Journal of Micromechanics and Microengineering*, Vol. 15, No. 9, p. 1713, 2005.

55. Young, W. C. and R. G. Budynas, *Roark's formulas for stress and strain*, Vol. 7, McGraw-Hill New York, 2002.

56. Meirovitch, L., *Fundamentals of vibrations*, Waveland Press, 2010.

57. Serway, R. A. and J. W. Jewett, *Physics for scientists and engineers with modern physics*, Cengage learning, 2018.

58. Fine, A., W. Amos, R. Durbin and P. McNaughton, "Confocal microscopy: applications in neurobiology", *Trends in neurosciences*, Vol. 11, No. 8, pp. 346–351, 1988.

59. Yong, Y. K., A. Bazaei and S. R. Moheimani, "Video-rate Lissajous-scan atomic force microscopy", *IEEE Transactions on Nanotechnology*, Vol. 13, No. 1, pp. 85–93, 2013.

60. Mahmood, I. A., S. R. Moheimani and B. Bhikkaji, "A new scanning method for

fast atomic force microscopy", *IEEE Transactions on Nanotechnology*, Vol. 10, No. 2, pp. 203–216, 2009.

61. Yong, Y., S. Moheimani and I. Petersen, "High-speed cycloid-scan atomic force microscopy", *Nanotechnology*, Vol. 21, No. 36, p. 365503, 2010.

62. Leblanc, M., "Study on the electrical transmission of light impressions", Vol. 2, No. 23, pp. 477–481, 1880.

63. Urey, H., D. W. Wine and T. D. Osborn, "Optical performance requirements for MEMS-scanner-based microdisplays", *MOEMS and Miniaturized Systems*, Vol. 4178, pp. 176–186, International Society for Optics and Photonics, 2000.

64. Hoy, C. L., N. J. Durr and A. Ben-Yakar, "Fast-updating and nonrepeating Lissajous image reconstruction method for capturing increased dynamic information", *Applied optics*, Vol. 50, No. 16, pp. 2376–2382, 2011.

65. Flusberg, B. A., J. C. Jung, E. D. Cocker, E. P. Anderson and M. J. Schnitzer, "In vivo brain imaging using a portable 3.9 gram two-photon fluorescence microendoscope", *Optics letters*, Vol. 30, No. 17, pp. 2272–2274, 2005.

66. Bazaei, A., Y. K. Yong and S. R. Moheimani, "High-speed Lissajous-scan atomic force microscopy: Scan pattern planning and control design issues", *Review of Scientific Instruments*, Vol. 83, No. 6, p. 063701, 2012.

67. Ferhanoglu, O., M. Yildirim, K. Subramanian and A. Ben-Yakar, "A 5-mm piezo-scanning fiber device for high speed ultrafast laser microsurgery", *Biomedical optics express*, Vol. 5, No. 7, pp. 2023–2036, 2014.

68. Tuma, T., J. Lygeros, V. Kartik, A. Sebastian and A. Pantazi, "High-speed multiresolution scanning probe microscopy based on Lissajous scan trajectories", *Nanotechnology*, Vol. 23, No. 18, p. 185501, 2012.

69. Takamatsu, T. and S. Fujita, "Microscopic tomography by laser scanning microscopy and its three-dimensional reconstruction", *Journal of microscopy*, Vol. 149, No. 3, pp. 167–174, 1988.

70. Webb, R. H. and F. Rogomentich, "Confocal microscope with large field and working distance", *Applied optics*, Vol. 38, No. 22, pp. 4870–4875, 1999.

71. Bayguinov, P. O., D. M. Oakley, C.-C. Shih, D. J. Geanon, M. S. Joens and J. A. Fitzpatrick, "Modern Laser Scanning Confocal Microscopy", *Current protocols in cytometry*, p. e39, 2018.

72. Shemelya, C., F. Cedillos, E. Aguilera, E. Maestas, J. Ramos, D. Espalin, D. Muse, R. Wicker and E. MacDonald, "3D printed capacitive sensors", *SENSORS, 2013 IEEE*, pp. 1–4, IEEE, 2013.

73. Kong, Y. L., I. A. Tamargo, H. Kim, B. N. Johnson, M. K. Gupta, T.-W. Koh, H.-A. Chin, D. A. Steingart, B. P. Rand and M. C. McAlpine, "3D printed quantum dot light-emitting diodes", *Nano letters*, Vol. 14, No. 12, pp. 7017–7023, 2014.

74. Wang, T. D., C. H. Contag, M. J. Mandella, N. Chan and G. S. Kino, "Dual-axes confocal microscopy with post-objective scanning and low-coherence heterodyne detection", *Optics letters*, Vol. 28, No. 20, pp. 1915–1917, 2003.

75. Boresi, A. P., R. J. Schmidt, O. M. Sidebottom *et al.*, *Advanced mechanics of materials*, Vol. 6, Wiley New York et al., 1985.

76. Rajadhyaksha, M., R. R. Anderson and R. H. Webb, "Video-rate confocal scanning laser microscope for imaging human tissues in vivo", *Applied optics*, Vol. 38, No. 10, pp. 2105–2115, 1999.

77. Holmstrom, S. T., U. Baran and H. Urey, "MEMS laser scanners: a review", *Journal of Microelectromechanical Systems*, Vol. 23, No. 2, pp. 259–275, 2014.

78. Yamada, K. and T. Kuriyama, "A novel asymmetric silicon micro-mirror for optical beam scanning display", *Micro Electro Mechanical Systems, 1998. MEMS 98. Proceedings., The Eleventh Annual International Workshop on*, pp. 110–115, IEEE, 1998.

79. Kumar, K., R. Avritscher, Y. Wang, N. Lane, D. C. Madoff, T.-K. Yu, J. W. Uhr and X. Zhang, "Handheld histology-equivalent sectioning laser-scanning confocal optical microscope for interventional imaging", *Biomedical microdevices*, Vol. 12, No. 2, pp. 223–233, 2010.

80. Wang, Y., K. Kumar, L. Wang and X. Zhang, "Monolithic integration of binary-phase fresnel zone plate objectives on 2-axis scanning micromirrors for compact microscopes", *Optics express*, Vol. 20, No. 6, pp. 6657–6668, 2012.

81. Yalcinkaya, A. D., O. Ergeneman and H. Urey, "Polymer magnetic scanners for bar code applications", *Sensors and Actuators A: Physical*, Vol. 135, No. 1, pp. 236–243, 2007.

82. Gokdel, Y. D., A. O. Sevim, S. Mutlu and A. D. Yalcinkaya, "Polymer-MEMS-Based Optoelectronic Display", *Electron Devices, IEEE Transactions on*, Vol. 57, No. 1, pp. 145–152, 2010.

83. Wang, Y., Y. D. Gokdel, N. Triesault, L. Wang, Y.-Y. Huang and X. Zhang, "Magnetic-Actuated Stainless Steel Scanner for Two-Photon Hyperspectral Fluorescence Microscope", *Microelectromechanical Systems, Journal of*, Vol. 23, No. 5, pp. 1208–1218, 2014.

84. Gokdel, Y., B. Sarioglu, S. Mutlu and A. Yalcinkaya, "Design and fabrication of two-axis micromachined steel scanners", *Journal of Micromechanics and Microengineering*, Vol. 19, No. 7, p. 075001, 2009.

85. Piyawattanametha, W., H. Ra, M. J. Mandella, K. Loewke, T. D. Wang, G. S. Kino, O. Solgaard and C. H. Contag, "3-D near-infrared fluorescence imaging us-

ing an MEMS-based miniature dual-axis confocal microscope", *IEEE Journal of Selected Topics in Quantum Electronics*, Vol. 15, No. 5, pp. 1344–1350, 2009.

86. Liu, T., A. J. Svidunovich, B. C. Wollant and D. L. Dickensheets, "MEMS 3-D Scan Mirror With SU-8 Membrane and Flexures for High NA Microscopy", *Journal of Microelectromechanical Systems*, Vol. 27, No. 4, pp. 719–729, 2018.

87. Mowla, A., T. Taimre, K. Bertling, S. Wilson and A. Rakić, "Confocal laser feedback microscopy for in-depth imaging applications", *Electronics Letters*, Vol. 54, No. 4, pp. 196–198, 2018.

88. Oxley, P., J. Goodell and R. Molt, "Magnetic properties of stainless steels at room and cryogenic temperatures", *Journal of Magnetism and Magnetic Materials*, Vol. 321, No. 14, pp. 2107–2114, 2009.

89. Quimby, R. S., *Photonics and lasers: an introduction*, John Wiley & Sons, 2006.

90. Nagasawa, T., Y. Oguchi and E. Iwase, "Operation of three-dimensional MEMS mirror by single superposed driving signal", *Japanese Journal of Applied Physics*, Vol. 56, No. 6S1, p. 06GN12, 2017.

91. Afsharipour, E., B. Park, R. Soltanzadeh and C. Shafai, "An electromagnetically actuated 3-axis gimbal-less micro-mirror for beam steering", *2018 International Conference on Optical MEMS and Nanophotonics (OMN)*, pp. 1–2, IEEE, 2018.